CHAPTER 1

INTRODUCTION

1.1 Introduction and Motivation

A large-scale quantum computer has the potential to hold a calculating power greater than the current fastest classical computer. The ultimate computing capability of the quantum computer comes from quantum bits or qubits, which represent both 0 and 1 state at the same time whereas classical bits can represent only one of the states [1, 2]. In consequence, the developed quantum algorithms allow solving certain problems such as a large number factorization and many-body systems, much faster than classical algorithms [3-5]. It has been estimated that with only 50 interaction-controlled qubits, quantum computing would exceed the performance of classical computing [6]. The supreme calculating capability of the quantum computer will extend the frontier of all branches of knowledge and lead to technological revolution.

In developing quantum computer, the system of neutral atoms individually occupying in each site of optical lattice is a strong candidate for realizing qubits physically. In the lattice, each atom in each trap is still detectable and addressable independently [7-10]. As the computational data is encoded into the internal states of the atoms through the employment of the near resonance light, the atoms are allowed to performing as qubits. The atoms in the lattice are well isolated with weak stray

light. This allows us to control properly the atoms with long trapping lifetime. Besides all above reasons, long range entangling interactions between the trapped single neutral atoms can be varied for on-off switching [11-13]. The coherently controlled interactions would be advantageous in quantum gate operations. However the error free quantum register confronts with an obstacle to load the perfect array of the single atoms without lattice vacancy. To resolve this problem, the simplest scheme of "one atom in a single well" is considered. Thus all crucial parameters, which suppress a single atom loading efficiency, would be studied in details. When the deterministic single atom preparation is achieved, the scalability from a single atom in a well to atoms in an optical lattice will be straightforward. In summary, a production of the single-neutral-atom source is not only capable of controlling the atoms in the microscopic scale but it is also worthwhile for realization of a quantum computer.

For past decade, there are several challenging attempts in deterministically preparing a single atom. The cavity-base method that trap the single atom at the antinode of the standing wave inside the cavity, has a difficult technique for loading single atom and gives a low efficiency [14, 15]. Furthermore, the scalability of this system is hard due to the use of cavity. The transition from the Bose-Einstein condensate (BEC) to Mott insulator in an optical lattice could contribute a high efficiency of loading single atom in each site of the lattice [16, 17]. However, the loading time of this route is long because of the complicated BEC generation. The other way for the single atom preparation is performing light-assisted collisions, of which the experimental technique is much simpler than the others and requires shorter loading time. In addition, the light-assisted collision can be employed in arbitrary

trap geometries. As semi-molecular potentials are shifted from the atomic potential levels when two atoms are closed to each other, both red- and blue-detuned light can induce a transition of the atoms, which is the beginning of two-body collision. Originally the red-detuned light has been used first for the single atom preparation. However the loading efficiency was limited at 50% [9, 18-20] because of the inelastic collision processes where the energy shared after the two-body collision is sufficiently high enough to make the pair loss event. This difficulty is resolved by using the blued-detuned light. In the case of blue-detuned light, the energy released from the collision is precisely controlled through detuning the light frequency in such a way that only one of the collision partners is lost. This provides the high loading efficiency of 83% [21]. The blue-detuned light-assisted technique shows signs of being a better pathway for the single atom preparation, since the loading efficiency and the loading time corresponding with this method have a potential to be improved.

In this thesis, the light-assisted collisions were studied for the purpose of enhancing the single atom loading efficiency and gaining knowledge of the collisional processes in both cases of red- and blue-detuned light. In the past, the cold collisions were studied in a scale of huge number of atoms where some information was hidden in the ensemble average of the large samples [22-25]. To extract the invisible information, an observation of individual collisional events is needed [26, 27]. In this study, we consider in the system such only two atoms in trap. The dynamics of the atoms under the influence of applied collision-inducing light are in our interest therefor detecting the individual collision occurrences.

1.2 Outline of Thesis

In Chapter 2, the background and relevant theory was described briefly in two parts. The first part of the chapter begins with reviewing the physics of standard trapping and cooling techniques such as Doppler cooling and Magneto-optical trap (MOT). An optical dipole trap that confines a single atom is described in the dressed-state picture. The Sisyphus and Polarized gradient cooling (PGC) techniques, which were employed for loading atoms into the dipole trap and cooling the atoms during imaging respectively, are also mentioned at the end. For the second part of Chapter 2, the atomic loss due to the cold collision induced by light is considered. This part begins with explaining the cold collision in the picture of a quasimolecular energy level. There are some theoretical models to describe this collision processes and the models are mentioned in the chapter as well.

In Chapter 3, the methods and apparatus for preparation of cold ^{85}Rb atoms are explained. The usual path way MOT was chosen for preparing the cold atoms. The MOT apparatus was constructed for the first time in Thailand at the Quantum Atom Optics (QAO) Laboratory. This apparatus consists of the four main systems, which are; the vacuum system for isolating the cold atoms from the environment; the laser system for cooling, trapping and detecting the atoms; the magnetic system for forming the confining force; and the imaging system for getting experimental data. The fluorescence image of the cold atomic cloud at the center of the MOT is shown at the end of the chapter.

To study the cold collision inside the dipole trap, part of this work was conducted at the Otago Atomic Physics Laboratory at the University of Otago in New Zealand. The apparatus and method for loading the cold atoms into the dipole trap are detailed in Chapter 4. The detection of Rb atoms in the dipole trap is reported and some characterization of the single Rb atoms also is presented in the chapter. As the result, it shows the ability to prepare both two atoms and single atom in the trap.

The dynamics of two atoms were measured while the laser light was being applied to induce the collision between the atoms. From the two-atom evolution, the individual collision events were detected and the result is reported in Chapter 5. The result is separated into two cases that are for the red and blue detuned light. As the simplicity of only two atoms in the trap, the simulation of their evolution was done for more understanding in the light-induced collision processes. In addition, the affect of the collision light parameters (intensity and frequency) to the single atom loading efficiency was studied. The efficiency result is reported in the chapter as well.

In Chapter 6, all of the results in this study are discussed and concluded.

CHAPTER 2

THEORETICAL BACKGROUND

The understanding of standard trapping and cooling techniques is necessary in preparing the cold atoms. This chapter begins by reviewing a fundamental physics that underlines these techniques in Sec. 2.1. After the atoms are trapped, the loss due to the cold collisions induced by laser light is considered; the detail is discussed in Sec. 2.2.

2.1 Cooling and trapping for neutral atoms

For the reason that atoms normally at room temperature must be cooled down before they can be captured and trapped, the basic of cooling mechanism such as Doppler cooling is introduced first in Sec. 2.1.1. In Sec. 2.1.2 a widely used Magneto-optical trap (MOT) is presented. The MOT is a combination of the Doppler cooling and an inhomogeneous quadrupole magnetic field. This technique exploits the Zeeman splitting to further enhance the trapping mechanism greatly [28]. Another kind of trap used in this study is an optical dipole trap explained in Sec. 2.1.3. It is based on the interaction between the electric-dipole moment of the atoms and the electric field of light. In this thesis, a polarization gradient cooling and a Sisyphus cooling were also used for further decreasing the kinetic energy of the trapped atoms. These cooling techniques are detailed in Sec. 2.1.4 and Sec. 2.1.5 respectively.

2.1.1 Doppler cooling

In the laser cooling theory, the temperature of an atomic ensemble T is defined by using an average of the atomic kinetic energy $\langle E_k \rangle$ in one dimension [29]:

$$\frac{1}{2} k_B T = \langle E_k \rangle. \tag{2.1}$$

This temperature assignment is adequate for the atoms that are in thermal equilibrium. At the equilibrium, the atomic velocity distribution is assumed to be the Mazwell-Boltmann (MB) distribution, which only depends on the speed of the atoms given by

$$f(v) = \sqrt{\frac{m}{2\pi k_B T}} \exp\left(-\frac{mv^2}{2k_B T}\right), \tag{2.2}$$

where m is an atomic mass and v is an atomic speed in one dimension.

As mentioned above, when an atom is cold, it moves slowly. On the other hand, a worm atom moves very quickly. Since the velocity distribution of the atoms is directly related to their temperature. The idea of Doppler cooling is to slow down these atoms by applying the laser light while the Doppler effect plays a crucial role as following details.

The capability of laser light to slow down atoms comes from the momentum transfer from the photons in the light beam to the atoms. To understand this, let us consider the system of an atom at rest interacting with a laser beam, of which the frequency is ω_0 resonant with an atom transition as shown in Figure 2.1. The atom may absorb the photon and change its state from the ground state to the excited state.

Then it emits a photon spontaneously in a random direction and goes back to the ground state.

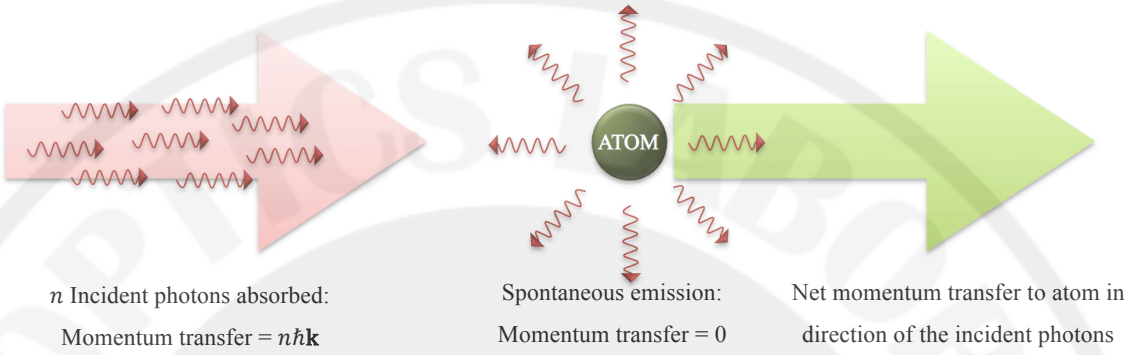

Figure 2.1. Momentum transfer in the laser cooling process. An atom at rest in laser beam absorbs a photon (represented by the small red arrow) in the incident laser beam, and then emits a photon spontaneously.

After n absorption/emission cycles a total momentum transfer to the atom due to the absorptions (n photons) is equal to $n\hbar\mathbf{k}$ in the same direction of the laser as represented by the pink arrow, where $\mathbf{k}$ is the wave vector of incident photons. The total momentum transfer due to the spontaneous emissions is zero due to the random direction of the emitted photons. As a result, the net momentum transfer to the atom is $n\hbar\mathbf{k}$ as represented by the green arrow. From these momentum exchanges, the atom experience a force called "the radiative force" with a corresponding time-averaged acceleration of [30]:

$$\langle \vec{a} \rangle = \frac{\hbar \mathbf{k} R(I, \omega)}{m}, \tag{2.3}$$

where $R(I,\omega)$ is the absorption rate which depend on the light intensity I and the light frequency ω. For a stationary atom in space, the absorption rate can be calculated to be:

$$R(I,\omega) = \frac{\Gamma}{2}\frac{I/I_s}{1 + I/I_s + (2(\omega - \omega_0)/\Gamma)^2}, \tag{2.4}$$

where Γ is the natural line width of an atomic transition and I_s is the saturation intensity. From this equation, the atom has the maximum absorption rate when the light frequency is ω_0.

Figure 2.2. The Doppler effect in the laser cooling process in one dimension. The details are described in text.

However, an atom has non-zero velocity. Thus the Doppler effect must be taken into accounted. As shown in Figure 2.2 when the atom counter propagates the light beam at a specific speed v, it experiences an increase in the light frequency amounted to $(v/c)\omega$, where ω is the light frequency in the rest frame and c is the speed of light. For this matter, if the laser beam is red detuned ($\omega < \omega_0$) from the resonance frequency of the atom, the atom can experience a light frequency shifted up to nearly ω_0. This leads to the atom having absorbed more photons with high $R(I,\omega)$ from the light beam. The opposite is also true when the atom moves along in the same direction of the beam.

The counter-propagating red-detuned laser beams are used for slowing down or cooling down the atom. The radiative force of the beam moving toward the atom is larger than that from the opposite direction as explained above. The velocity of the atom either the direction of the laser beams is decreased. To extend this cooling technique into three dimensions, we use three pairs along three mutually orthogonal axes in three dimensions. The atomic cloud is slowed down within the overlapping volume where the beams intersected. This essentially produces velocity-dependent damping force analogous to when a particle travels in sugar molasses and thus name the "optical molasses".

However, the heating due to the stochastic nature of photon absorption and emission leads to the limit of this cooling technique. At a low-intensity and the red detuning equal to $\Gamma/2$, the minimum limit of this Doppler temperature [30] is

$$T_D = \frac{\hbar\Gamma}{2k_B}. \tag{2.5}$$

This limit is typically several hundred μK. Associated with this temperature is the velocity in one dimension $v_D = \sqrt{k_B T/m}$.

2.1.2 Magneto-optical trap

In the optical molasses the atoms are not trapped and as a result a position dependent force is needed. We may introduce this force by applying a linearly inhomogeneous magnetic field to our atomic sample. This will create a broken symmetry that lifts

degeneracy of all magnetic sublevels in the atoms, recognized as the Zeeman splitting or the Zeeman effect [31].

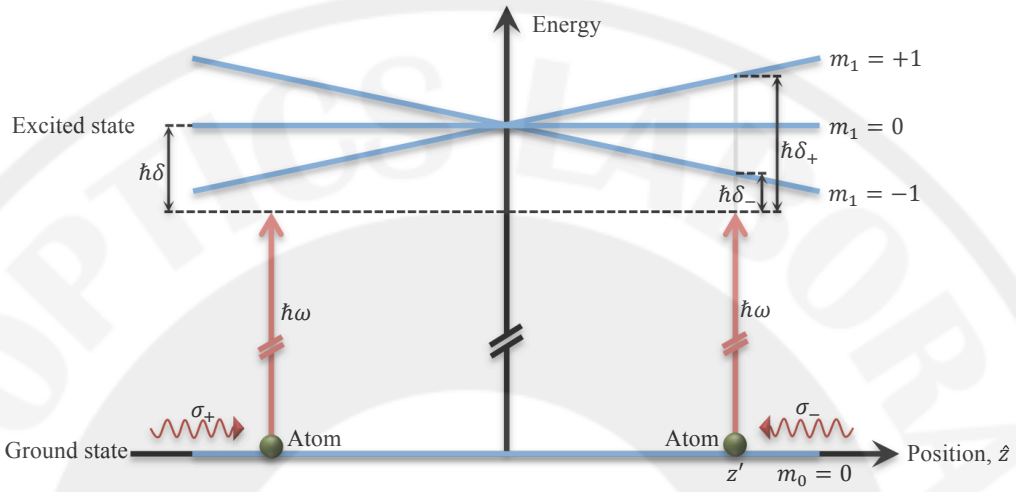

Figure 2.3. Cooling mechanism in one-dimensional MOT. The atomic ground state and first excited state are indicated by the total angular momentum of $J = 0$ and $J' = 1$ respectively. The excited state is split because of the Zeeman effect. The red arrows indicate the red-detuned incident photons with right-handed (σ_+) or left-handed (σ_-) polarizations, which are red detuned by δ.

Let us consider an atom with a ground state $J = 0$ and an excited state $J' = 1$ in the magnetic field $\mathbf{B} = B_z\hat{z}$ where B_z is directly proportional to z as shown in Figure 2.3. The counter-propagated light beams with right-handed (σ_+) and left-handed (σ_-) polarizations red detuned by δ from the zero field atomic resonance are applied. The energy of the atomic states shifts proportional to $m_j B_z$ as a result of Zeeman effect. In the right hand side, the excited state with quantum number $m_1 = +1$ is shifted up due to $B_z > 0$ where the state $m_1 = -1$ is shifted down. Suppose that the atom is at position z'. The detuning of the light from the $\Delta m = -1$ atomic transition (from the ground state with $m_0 = 0$ to the excited state with

$m_1 = -1$) is small as indicated by δ_- in the figure but the detuning from the $\Delta m = +1$ transition indicated by δ_+ is much larger than the other one. Due to the selection rules for circularly polarized light, the $\Delta m = -1$ and $\Delta m = +1$ transitions can occur only by absorbing the σ_- light and the σ_+ light respectively [30]. Thus the atom interacts more with the radiative force by the σ_- light than by the σ_+ one. As a result, it is pushed toward the origin where the magnetic field vanishes. On the other side ($B_z < 0$), the atom interacts more with the σ_+ light and again the atom is pushed toward the center.

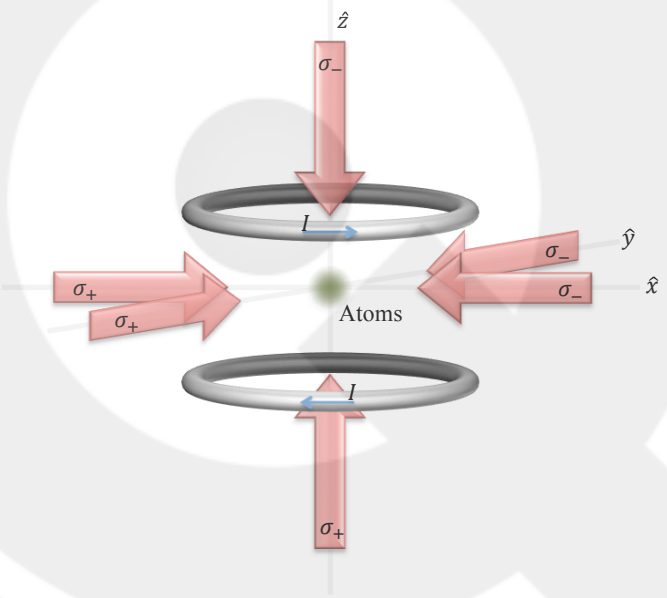

Figure 2.4. Schematic of the MOT. Six lasers beams are shined as represented by the red arrows. The directions of the current ***I*** applying to the anti Helmholtz coils are indicated by blue arrows.

This effect operates in position space to confine and push atoms back to the center of the trap, whereas the optical molasses mentioned before operate in velocity

space to slow down the atoms. This technique operating in both position and velocity space is called Magneto-optical trap (MOT).

The configuration of the MOT is shown in Figure 2.4. Three pairs of counter-propagating light beam have the circular polarization as described above. The overlapping region of the beams is aligned at the center of a quadrupole magnetic field. The field is created by using two coils in anti-Helmholtz configuration for which current in each coil runs in opposite direction. A MOT cloud of atoms is accumulated in this region.

2.1.3 Dipole traps

In this study, the cold MOT atoms were loaded into an optical dipole trap to study their properties and their collision process. (By loading into the dipole trap, a compressed MOT (cMOT) [30], following with the optical molasses as described in Sec. 2.1.4, were performed.) The advantages for using the dipole traps are: the atoms in dipole traps have much lower interaction with the trapping light compared with the MOT configuration; the trap depth can be adjusted conveniently by changing the power of the trapping laser; and the dipole traps can be scalable conveniently.

The crucial key of the dipole traps is that the energy level of the atoms is shifted when an atom interacts with a light field. The gradient of the energy can create a confining dipole force for the atoms. The concepts of atom interacting with the field can be explained by using a dressed state pictures that treat a quantized atom interacting with a quantized light field. First, the optical trap is described by

considering two-level atoms before the behavior of real multilevel atoms is exposed at the end.

Atoms in a quantized light field

In a quantum mechanical picture, an interaction of a quantized atom with a quantized monochromatic single mode laser field is treated and the eigenstates of this system are "dressed states". The corresponding eigenenergies are shifted as a function of the detuning and the number of photons in the field. This system treatment starts from the two level atom and then extends to all possible transition states.

Let us start with the uncoupled Hamiltonian, which is the sum of two parts: $H_0 = H_A + H_L$, where H_A is the atomic Hamiltonian and H_L is the Hamiltonian of the laser field. H_A can be taken from the sum of a kinetic energy of an atom and an atomic internal energy. However in this treatment, the kinetic energy term is omitted [32] and H_A is then

$$H_A = \hbar\omega_0 b^+ b. \tag{2.6}$$

Here $b^+ = |e\rangle\langle g|$ and $b = |g\rangle\langle e|$ are the raising and lowering operators respectively, where $|g\rangle$ is an atomic ground state with zero energy and $|e\rangle$ is an excited one with energy $\hbar\omega_0$. For the laser mode containing photon of energy $\hbar\omega$, the Hamiltonian of this single mode quantized field is

$$H_L = \hbar\omega(a^+ a + \frac{1}{2}), \tag{2.7}$$

where a^+ and a are the creation and annihilation operator respectively.

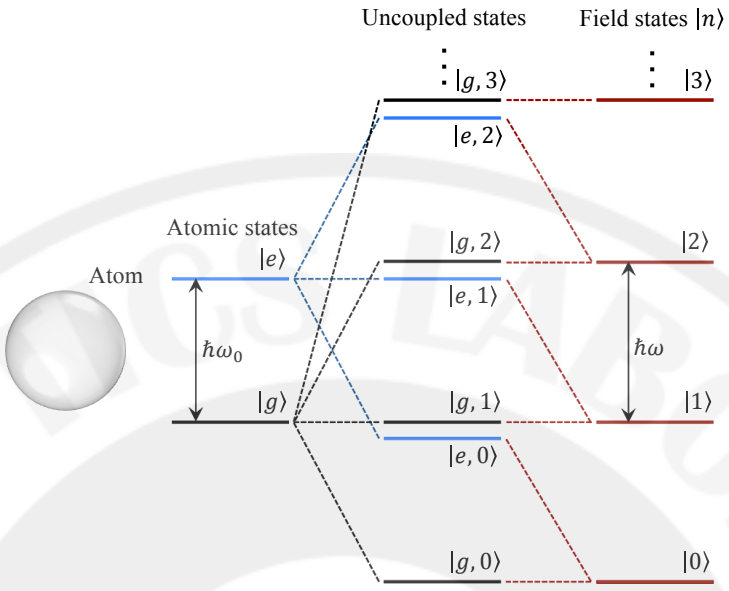

Figure 2.5. Energy level scheme for the atom with the $|g\rangle$ and $|e\rangle$ states (left) and the atom plus field Hamiltonian of uncoupled system.

An energy diagram of uncoupled system H_0 is shown in Figure 2.5. The ordinary atomic state levels ($|g\rangle$ and $|e\rangle$) are repeated for each photon number n and are shifted up by $\hbar\omega$ (the energy of the photon in the field). Then the attention is focused into the two closed adjacent levels of $|g, n+1\rangle$ and $|e, n\rangle$ called manifolds. In each manifold, the levels are spaced by $\hbar\omega_0 - \hbar\omega = \hbar\delta$ where δ is the detuning of the laser.

For atom-laser photon coupling, the interaction between the atomic dipole and the laser field is represented by

$$H_{AL} = -\mathbf{d} \cdot \mathbf{E}(\mathbf{r}) = k(b^{+}a + ba^{+}), \tag{2.8}$$

where $\mathbf{d} = \mathbf{d}_{ge}(b^+ + b)$ is atomic electric-dipole moment operator ($\mathbf{d}_{ge} = \langle g|\mathbf{d}|e\rangle = \langle e|\mathbf{d}|g\rangle$), $\mathbf{E}(\mathbf{r}) = \mathbf{e}\sqrt{\frac{\hbar\omega}{2\epsilon_0 V}}(a + a^+)$ is the laser field operator with a classical atomic position $\mathbf{r}$ (where $\mathbf{e}$ is the unit polarization vector and V is the volume of the field cavity), and k is a coupling constant equal to $-\mathbf{e}\cdot\mathbf{d}_{ge}\sqrt{\frac{\hbar\omega}{2\epsilon_0 V}}$ [33]. This coupling H_{AL} represents the excitation (first term) and stimulated emission (second term) of the atom induced by the light field. When the atom-laser coupling is taken into account, the dressed-atom Hamiltonian is

$$H_{DA} = H_0 + H_{AL} \tag{2.9}$$

and the new eigenstates called "dressed states" are

$$|1, n\rangle = \sin\theta|g, n+1\rangle + \cos\theta|e, n\rangle$$

$$|2, n\rangle = \cos\theta|g, n+1\rangle - \sin\theta|e, n\rangle, \tag{2.10}$$

where the angle θ is define by $\tan 2\theta = -\Omega/\delta$ and $0 \le \theta \le \pi$. Here Ω is Rabi frequency, which is equal to $\frac{2}{\hbar}k\sqrt{\langle n\rangle}$ [33].

From the coupling, the energy levels of the dressed states are shifted from the uncoupled ones by ΔE as shown in Figure 2.6. The separation of each pair of dressed states is calculated by an interval

$$\hbar\Omega' = \hbar\sqrt{\delta^2 + \Omega^2} \tag{2.11}$$

and are symmetry located with respect to the uncoupling ones.

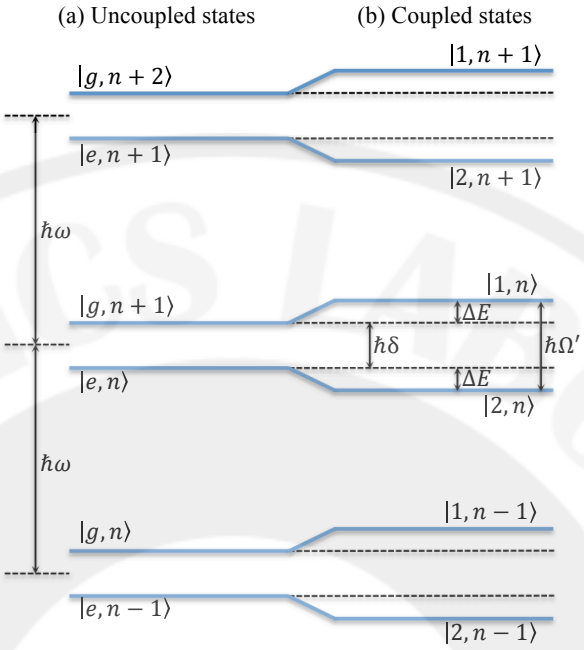

Figure 2.6. Dressed-atom energy diagram that shows uncoupled states in (a) and coupled states in (b) of the states combined atom-laser mode system.

The value of ΔE represented in Figure 2.6 (b) is equal to $\Delta E = \frac{\hbar}{2}(\Omega' - \delta)$. Let us consider in the case of far detuning ($\delta \gg \Omega$). Then ΔE can be approximated by :

$$\Delta E = \pm \frac{\hbar \Omega^2}{4\delta}. \tag{2.12}$$

The upper and lower sign are applied for the ground and excited states respectively.

Consider an atomic transition from a ground state with angular momentum J to an excited state with angular momentum J'. For this real multilevel atom, its energy shifts depend on the hyperfine states and can be expressed using a real transition coefficient or "Clebsch-Gordan coefficient, C_{ij}" and a reduced matrix element $\langle J' | \mathbf{d} | J \rangle$. If $|g_i\rangle$ and $|e_j\rangle$ are the considered states and $\langle g_i | \mathbf{d} | e_j \rangle = C_{ij} \langle J' | \mathbf{d} | J \rangle$,

the energy shift of specific state $|g_i\rangle$ can be calculated by summing up the contributions of all coupled excited states $|e_j\rangle$:

$$\Delta E_i = \frac{\hbar\Omega^2}{4}\sum_j \frac{C_{ij}^2}{\delta_{ij}}, \tag{2.13}$$

where δ_{ij} is the detuning of the laser field of the transition from $|g_i\rangle$ to $|e_j\rangle$.

The optically induced shift of the atomic energy level is known as the "light shift" or "ac Stark shift". The light shift of the ground state ΔE_i exactly corresponds to the dipole potential $U_{dip,i}$ that can be used for trapping atoms.

Dipole trap realization

To create the optical trap, a specific frequency light is used. From the state-dependent ground-state dipole potential, two specific types of real experiments are described in detail in the subsection below. As seen in the equation (2.13) the shifted energy of atom is directly proportional to the number of photon but inversely proportional to the laser detuning. If the light is red detuned ($\delta < 0$), the shifted energy has a negative value. In consequence the atom is attracted to the highest light intensity (or highest number of photons) region where the energy level of the atom is lowest. In the opposite if the light is blue detuned ($\delta > 0$), the atoms can be accumulated at the lowest light intensity region.

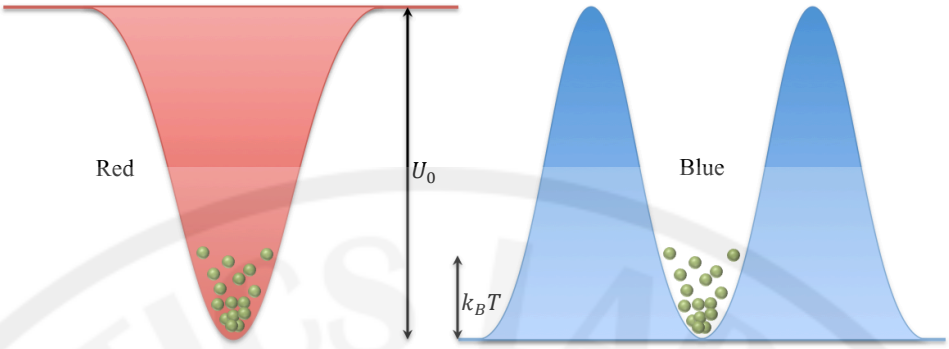

Figure 2.7. The cold atoms with temperature T trapped in the U_0 deep optical traps using red (left figure) or blue (right figure) detuned light.

To create the trap, the repulsive blue-detuned light has to be applied surrounding the atoms as illustrated in Figure 2.7 (right). The atoms are trapped in the dark place leading to the great advantage of this kind of trap. The trapped atoms are little affected by photon scattering, collisional losses induced by the light, and the light shifts of the atomic energy level. However, the blue-detuned trap is not simple to be realized. To create the optical walls, the three mains methods have been purposed that are the light sheets [34], the hollow laser beams [35], and Evanescent waves [36].

For a red detuned dipole trap, atoms are trapped where a light intensity is greatest as illustrated in Figure 2.7 (left). Experimentally the optical potential is easily generated using the focus of a far-red-detuned Gaussian beam (illustrated in Figure 2.8 (a)) that is called far-off resonance trap or FORT [37].

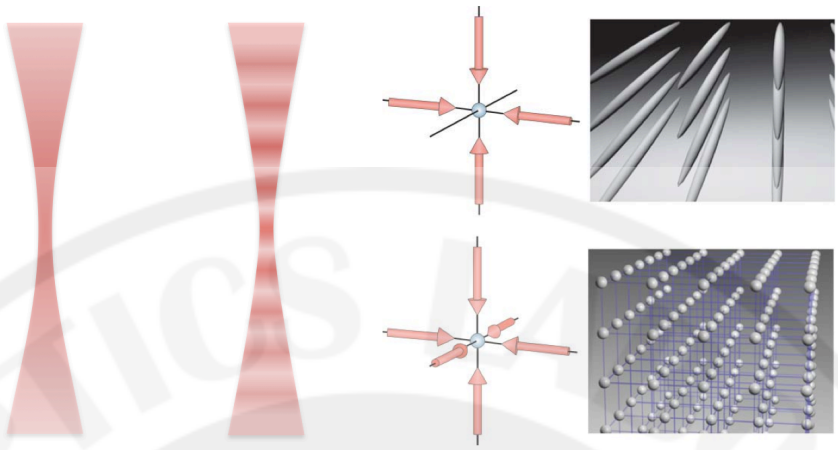

(a) (b) (c)

Figure 2.8. Red detuned light beam configurations for far-off resonance trap (FORT). (a) Focused-beam trap: the Gaussian beam is focused to create gradient of intensity in the axial axis of the beam. (b) Standing-wave trap: the counter propagating focused-beams create the one-dimensional optical trapping array. (c) Crossed-beam trap: two (top figure) or three pairs (bottom figure) of the counter propagating focused-beams are crossed each to create a two-dimensional or a three-dimensional trapping array, respectively [38].

An optical dipole trap is scalable conveniently. In Figure 2.8 (b), a one-dimensional optical trapping array can be straightforwardly generated from a pair of the counter propagating red detuned focused-beams. The atoms can be axially confined at the antinodes of the standing wave. An addition of more laser beams to the 1D configuration leads to a two-dimensional or three-dimensional optical array as shown in Figure 2.8 (c); the two (top) or three (bottom) pairs of orthogonal standing wave are intersected at their foci where the 2D or 3D trapping array are created.

In our study, the cold atoms were loaded into FORT, of which more details are explained in Chapter 4. As the FORT has no cooling mechanism, it is necessary to apply others cooling light beams for reducing the excess kinetic energy of the trapped atoms that make the atoms stay in the trap longer. For example, the polarization gradient cooling was used (Sec. 2.1.4) during the collision duration and the Sisyphus cooling was formed (Sec. 2.1.5) during the imaging duration. The theories of both cooling techniques are explained below.

2.1.4 σ_--σ_+ polarization gradient cooling

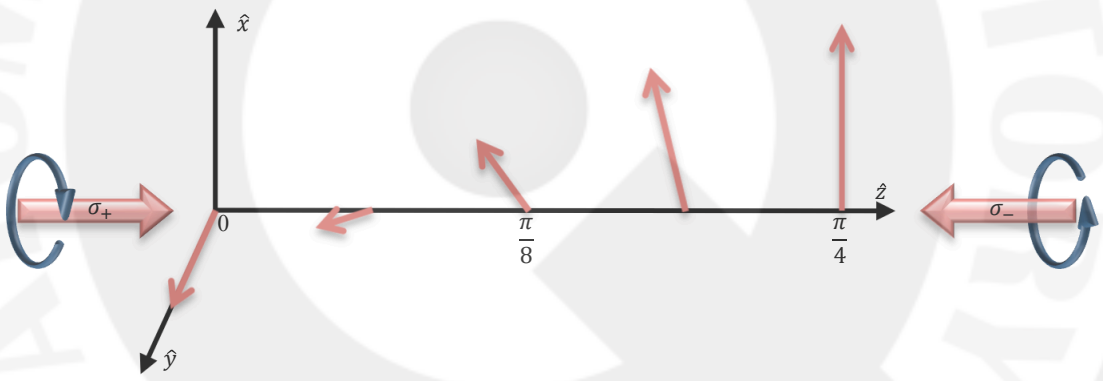

Figure 2.9. Polarization gradient field for the σ_--σ_+ configuration.

The Doppler cooling theory described before neglects the degeneracies of atomic energy levels. Atoms that are moving in the optical molasses experience the polarization gradients and are optically pumped by the molasses light to redistribute a population in their Zeeman sublevels of ground states. This effect gives another cooling mechanism that can cool atoms down below the Doppler limit, called "polarization gradient cooling, PGC".

There are two configurations to form the polarization gradient. The first one uses the counterpropagating laser beams of orthogonal linear polarizations to produce a local polarization that varies from linear to circular to orthogonal linear and to orthogonal circular with a spatial period of $\pi/2$. The second one uses the counterpropagating light beams of σ_- and σ_+ polarizations to form a linear polarization that rotates around the beam direction as shown in Figure 2.9. Corresponding to these two types of gradient, there are two different PGCs that can be realized [39].

In this study, PGC with σ_- - σ_+ configuration was used because the polarizations of the cooling beams are the same as that use in the MOT. Let us consider a moving atom in this polarization gradient with speed v. The atom responds to the local polarization of light with an optical pumping time τ_p, characterizing the mean time that it is transferred by fluorescence cycle to the other sublevel. If the atom is moving slowly enough ($\tau_p \ll \frac{\lambda}{2v}$, where λ is a wave length of the light), the light will have enough time to optically pump the atom into a state that has an orientation corresponding to the local polarization. On the other hand, for the fast atom ($\tau_p \gg \frac{\lambda}{2v}$), the optical pumping rate is too slow to make the orientation. In this case, the atom will be cooled by the Doppler cooling only.

To understand this PGC mechanism, the simplest model explains the ground-state orientation by using the atoms having $J = 1$. If the atoms is at rest at $z = 0$ and we take the quantization axis along the local linear polarization axis which is $\hat{y}$ as seen in Figure 2.9. The atoms will be optically pumped to redistribute their

populations of the magnetic substates. Due to the linear polarization, the most of them tend to be accumulated in the $m = 0$ sublevel and a smaller portion of them populate in the $m = +1$ and $m = -1$ sublevels equally. For the atoms moving in the same direction of the beams, they experience the rotation of the linear polarization and are optically pumped in order to follow it. However, the ground substate population of the moving atoms always lags behind the steady state distribution following the local field [39]. From this effect, the atoms traveling toward the σ_+ beam will populate the $m = +1$ state more than the $m = -1$ state and vice versa the $m = -1$ state is more populated for the atoms traveling in opposite direction.

This small imbalance in the distribution of the ground substate creates the large force to damp the atomic velocity. That is because the atoms with $m = +1$ have a higher probability to absorb the σ_+ photon than the σ_- photon (see the transition strength in Appendix A) and the most of them travel toward the σ_+ beam. Thus their motion will be damped by the radiative force of the σ_+ beam. For the atoms traveling toward the σ_- beam, they are optically pumped into the $m = -1$ state and then is slowed down by the radiative force of σ_- beam.

This PGC mechanism relies on the unbalance of the two radiative forces when the atom is moving due not to the Doppler shifts of two laser beams as in the Doppler cooling, but to an unbalance of the ground substate distribution because of the time lag of the atom orientation to follow the local field.

2.1.5 Sisyphus cooling

Another efficient cooling method called Sisyphus cooling is based on the stimulated emission [40]. Consider an atom moving in a spatially periodic potential created by a standing light wave. This causes an exchange between kinetic and potential energy of the atom. If the standing wave is formed by two counterpropagating light beams with frequency ω that is blue detuned δ from the atomic resonance. For a weak light intensity (saturation parameter $s \lesssim 1$), the beams produce heating of the atom because of the Doppler effect. By contrast, when the light intensity is high enough (saturation parameter $s \gg 1$), the beams produce a cooling mechanism due to the emission processes that are predominant over the Doppler heating.

A simple way to explain the atomic motion in the strong standing wave is using a dressed state picture as represented in Figure 2.10. The dressed energy levels are varied spatially following the light intensity (or the number of photons) in the standing wave. At a node position with the vanished intensity, the Rabi frequency Ω is equal to zero. Thus the coupling dressed states $|1, n+1\rangle$ and $|2, n+1\rangle$ coincide with the uncoupled states $|g, n+2\rangle$ and $|e, n+1\rangle$, respectively, where g and e represent the ground state and the excited state, respectively, and n is the light field quantum number as mentioned before Equation (2.10) in Sec 2.1.3. Because the light is blue detuned by δ, the energy level of $|g, n+2\rangle$ is higher than the level of $|e, n+1\rangle$ by $\hbar\delta$. At a position with the non-zero intensity, the dress state $|1, n+1\rangle$ start to have a nonzero coefficient of $|e, n+1\rangle$ and the state $|2, n+1\rangle$ also has a nonzero coefficient of $|g, n+2\rangle$ as well. In consequent the energy splitting is

increased as $\hbar\Omega' = \hbar[\delta^2 + \Omega^2]^{1/2}$ written in Equation (2.11). This splitting is largest at the antinodes of the standing wave where the light intensity is highest.

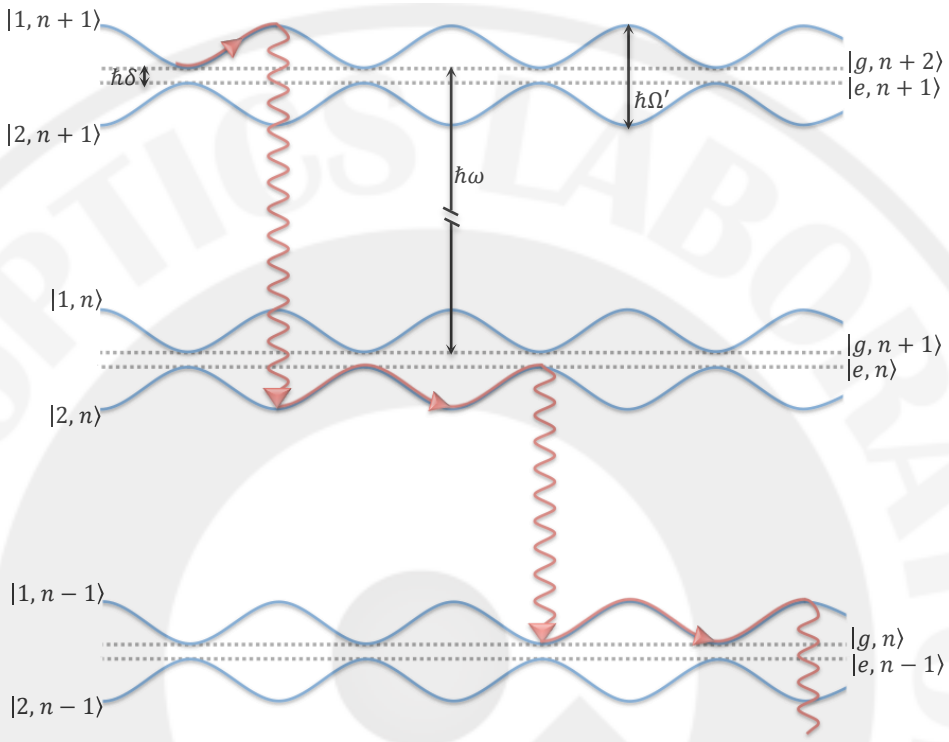

Figure 2.10. Sisyphus cooling processes in a strong standing wave. The blue lines represent the dressed atom energy levels, which are varied spatially due to the light intensity in the standing wave. The dotted lines represent the energy levels of the bare states. The red lines represent the atomic potential energy and where the spontaneous emissions occur.

Let us consider the atom having trajectory as shown in Figure 2.10. The atom in $|1, n+1\rangle$ travels in the periodic of energy level starting from the valley. It climbs up to the top of the potential hill where contains the largest coefficient of $|e, n+1\rangle$. Thus at this position, the atom has the maximum probability to spontaneously emit photon and decay into the lower dressed states $|1, n\rangle$ or $|2, n\rangle$ containing $|g, n+1\rangle$. If the atom decays into $|1, n\rangle$ where it is on the top of the hill, this will not change any

thing from a mechanical point of view. By contrast, if the atom decays into the $|2, n\rangle$ level where it is in the valley again. In this case, the velocity of the atom will be decreased because its kinetic energy is converted to potential energy while climbing up to the top of the hill and then jumps to the bottom of another one by the spontaneous emission. Now the atom in $|2, n\rangle$ starts to climb up again to the top of the hill where the probability to decay is highest because of the equivalent of $|2, n\rangle$ and $|e, n\rangle$ at the nodes of the standing wave. Then the atom may decay to the valley of the lower level again as shown in the figure. Thus the atom seems to be always climbing the hills and losing its potential energy by spontaneously emitting photon. This process will repeat until the atom has too small kinetic energy to climb the next hill. This cooling process exhibits a picture similar to when Sisyphus in Greek mythology tried to interminably push a huge rock up the hill; the reason why this cooling method is called the Sisyphus cooling.

2.2 Trap loss

For atoms in trap, the atom loss experiments have shown that the main loss mechanism is caused by the atomic collisions. To understand the trap loss, let us start with the rate of trap loss due to the collisions, which can be measured by observing the number of atoms in a trap N that changes by the rate

$$\frac{\mathrm{d}N}{\mathrm{d}t} = L - \gamma N - \beta \int_R \mathrm{d}^3R'[n(R',t)]^2 \,, \tag{2.14}$$

where L is an atomic loading rate of the trap, γ is the decay rate constant, β is the loss rate constant, and $n(R,t)$ is the atomic cloud distribution [30].

The first term of this expression represents an atomic capture rate of the trap that depends on the trap parameters. The second term represents the decay mechanism due to the collision between trapped atoms and a thermal background gas. The last term represents the trap loss mechanism due to the collisions between two trapped atoms. To study the collisional loss, this section starts with discussion about the principle of the collision (Sec. 2.2.1), which can be induced by either red detuned light (Sec. 2.2.2) or blue detuned one (Sec. 2.2.3).

2.2.1 Light induced cold collisions

In the presence of light field, the inelastic collisions between cold atoms are induced. The theory of the collisions can be explained by using the quasimolecular picture, $|S+S\rangle$ and $|S+P\rangle$ states as represented in Figure 2.11. The $|S+S\rangle$ asymptote

represents two ground state atoms that interact each other at an internuclear separation R. When the separation is of the order of optical wavelength, an attractive ground state potential is formed as

$$U_g(R) = \frac{C_6}{R^6} + \frac{C_8}{R^8} \dots$$

$$\simeq \frac{C_6}{R^6}, R \gg 0\,, \tag{2.15}$$

where C_i is the coefficient resulting from the interaction, i is an integer number [41]. Here C_6 and C_8 are negative.

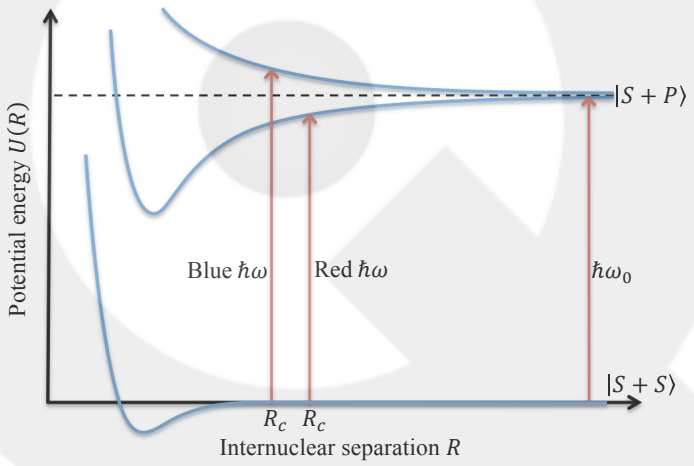

Figure 2.11. Schematic of the quasimolecular energy levels of $|S+S\rangle$ and $|S+P\rangle$ as a function of the internuclear separation R.

The $|S+P\rangle$ asymptote represents one ground and one excited state atoms. The energy level of this state is above the ground state $|S+S\rangle$ by the atomic excitation energy $\hbar\omega_0$ and is shifted due to the interaction between two atoms. The excited potential correlating to the $|S+P\rangle$ can be calculated as

$$U_e(R) = \hbar\omega_0 + \frac{C_3}{R^3} + \frac{C_5}{R^5} \ldots$$

$$\simeq \hbar\omega_0 + \frac{C_3}{R^3}, R \gg 0. \quad (2.16)$$

From this equation if C_3 is negative, the energy level of $|S + P\rangle$ is shifted below the $\hbar\omega_0$ level. In contrast to the positive C_3, the energy level is shifted up as shown in Figure 2.11.

Let consider a collision between two ground state atoms in the light field $\hbar\omega$. Their probability of transition to $|S + P\rangle$ is highest at the Condon point R_C, where the separation between the two states is resonant with the field. For the detuning δ, R_C is given by

$$\hbar\delta = \frac{C_3}{{R_C}^3} \quad \text{or} \quad R_C = \left(\frac{C_3}{\hbar\delta}\right)^{1/3}. \quad (2.17)$$

In an inelastic collision process, if the atoms are in the red detuned light field, they will absorb a photon, transition to the lower $|S + P\rangle$, and approach to each other following the attractive potential curve. On the other hand, for the atoms in the blue detuned light field, they will be excited to the upper $|S + P\rangle$. In this repulsive potential the atoms will approach one another until they reach the turning point of the nuclear motion and start to separate from each other along the repulsive curve. In either case, the atoms will decay back to $|S + S\rangle$ with the spontaneous decay and gain a certain amount of energy.

For collisions induced by the red detuned light, there are many studies about the collisions in MOTs leading to the traps loss. These studies are very important to

getting more precise measurements of the MOT's properties. For the blue detuned light assisted collisions, this mechanism is used in preparing individual atom due to the controllability of the energy gained in the collision process. These two kinds of collisions will be explained in detail in the next sections.

2.2.2 Collisions in MOT

During loading MOT, the red detuned light is applied to cool and confine atoms. At the same time, the two cold atoms may absorb the light photon at the initial stage of a collsion. In this collision, the atoms gain more kinetic energy from an internal electronic energy leading to increase in the nuclear motion. If the velocity of the atoms is higher than the recapture ability of the MOT, the atoms will escape the trap. To explain this cold collision induced by the red-detunded light, a semiclassical Gallagher-Pritchard model (GP model) was proposed. The GP model has been improved by Juienned and Vigue called JV model.

Gallagher-Pritchard model

The GP model is the first theoretical approahes for cold collisions [42]. The model was propose to describe the trap loss mechanisms due to a fine-structure-changing collision (FCC) and a radiative escape (RE). Figure 2.12 (a) and (b) show the two basic light-induced collisional trap loss processes which are FCC and RE respectively.

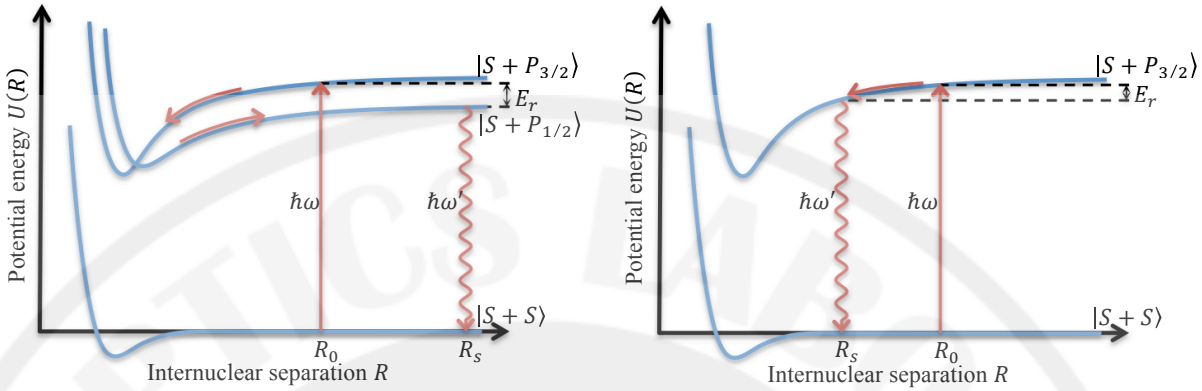

Figure 2.12. Schematic of the quasimolecular energy levels of $|S + S\rangle$, $|S + P_{1/2}\rangle$ and $|S + P_{3/2}\rangle$ as a function of the internuclear separation R. The two colliding atoms are in the light field with the frequency of ω, which is red detuned from the atomic D2-line transition. Due to the light, the atom may undergo either the FCC (a) or RE (b) passage.

In the FCC mechanism (see Figure 2.12 (a)), two colliding atoms in the red detuned light field approach each other in the ground state $|S + S\rangle$. They may absorb the photon with energy $\hbar\omega$ and excite into $|S + P_{3/2}\rangle$ at the separation of R_0. In the excited state, they are accelerated along the separation R towards each other by the attractive potential. At a very small R, the potential becomes repulsive and then the atoms start to move apart again. However the $|S + P_{3/2}\rangle$ can be coupled to another fine structure state $|S + P_{1/2}\rangle$. Thus the atoms may change to $|S + P_{1/2}\rangle$ state and move far away from each other. Finally, the atoms spontaneously decay back to the ground state and emit photon with energy $\hbar\omega'$. The FCC process can be described by

$$|S + S\rangle + \hbar\omega \longrightarrow |S + P_{3/2}\rangle \longrightarrow |S + P_{1/2}\rangle + \Delta E_{FS}$$

where ΔE_{FS} is the energy between fine structures, $|S + P_{3/2}\rangle$ and $|S + P_{1/2}\rangle$. In this FCC collision, the atoms gain kinetic energy equal to $E_r = \hbar(\omega - \omega') \approx \Delta E_{FS}$ where $h\delta \ll \Delta E_{FS}$.

In the RE mechanism (see Figure 2.12 (b)), after the absorbtion the atoms in $|S + P_{3/2}\rangle$ are accelerated towards each other. Then the atoms spontaneously emit photon with the energy of $\hbar\omega'$ and decay back to the ground state at the separation of R_s. In this case, the atoms gain released energy E_r, which is also equal to $\hbar(\omega - \omega')$. The RE process can be represented by

$$|S + S\rangle + \hbar\omega \longrightarrow |S + P_{3/2}\rangle \longrightarrow |S + S\rangle + \hbar\omega'.$$

The GP model begins with a stationary ground-state atom pair at internuclear separation R_0 in the light field and assumes that the excitation probability for the pair can be determined by an expression:

$$P_e(R_0) = \frac{\Omega^2}{[\delta(R_0)]^2 + (\Gamma_M/2)^2}, \tag{2.18}$$

where $\delta(R_0)$ is the local detuning which is $\omega - \left[U_e(R_0) - U_g(R_0)\right]/\hbar$. For this model, the ground-state energy level $U_g(R)$ is estimated to be zero at any R. This quasistatic approximation is reasonable if the collision processes is slow enough. From this expression, the model allows the colliding pair to be excited at an off-resonant position ($R_0 \neq R_C$) and the bounds are limited by the molecular linewidth Γ_M.

After excitation, the two atoms on quasimolecular excited state $|S + P_{3/2}\rangle$ are accelerated by the attractive potential $U_e(R)$. Their relative radial velocity as a function of the separation then is

$$v(R) = \sqrt{\frac{2}{\mu}\{E_{k0} - [U_e(R) - U_e(R_0)]\}}\,, \tag{2.19}$$

where μ is the reduce mass, E is an initial relative kinetic energy of the atoms. A classical time that is required to travel form R_0 to R_s, is given by $t = \int_{R_0}^{R_s} \frac{\mathrm{d}R}{v(R)}$. Thus the probability that the quasimolecule survives in the excited state to the internuclear separation R_s is

$$\begin{aligned} S &= exp(-\Gamma_M t) \\ &= exp\left(-\Gamma_M \int_{R_0}^{R_s} \mathrm{d}R \left[\frac{2}{\mu}\{E_{k0} - [U_e(R) - U_e(R_0)]\}\right]^{-1/2}\right). \end{aligned} \tag{2.20}$$

For calculation of S in this GP model, Gallagher and Pritchard ignored the initial kinetic energy E_{k0}, assumed Γ_M to be a constant $2\Gamma_A$ where Γ_A is an atomic linewidth and set $R_s = 0$. This survival probability of the GP model then is

$$S_{GP} = exp\left(-(\delta_\tau/\delta)^{5/6}\right), \tag{2.21}$$

where δ_τ is the detuning corresponding to $R_0 = R_\tau$ where $\tau = {\Gamma_M}^{-1} = \int_{R_\tau} \frac{\mathrm{d}R}{v(R)}$. If the excited quasimolecule can reach the coupled region between $|S + P_{3/2}\rangle$ and $|S + P_{1/2}\rangle$ where the FCC occurs, it rapidly passes this region twice. A net total angular momentum J -changing probability (the quasimolecule undergoes the

$|S + P_{1/2}\rangle$ channel), η_J, is equal to $2P_{LZ}(1 - P_{LZ})$ where P_{LZ} is the Landau-Zener single-transit curve-crossing probability (will be explained in the next subsection, Landau-Zener transition). If the quasimolecule oscillates through the crossing, the FCC probability is the sum of the probability of each repeated crossing [43],

$$P_{FCC} = \frac{\eta_J S_{GP}}{\left(1 - {S_{GP}}^2 + \eta_J {S_{GP}}^2\right)}. \tag{2.22}$$

The probability of radiative escape, P_{RE}, is obtained from integration similar to the FCC one. This GP model considers only the quasimolecule that transits in an inner R region where its released energy E_r is greater than an energy needed to achieve radiative escape in MOT. If the quasimolecule spends time $2t_E$ in this region before spontaneous decay, then the RE probability can be written as

$$P_{RE} = \frac{2t_E \Gamma_M S_{GP}}{\left(1 - {S_{GP}}^2 + \eta_J {S_{GP}}^2\right)}. \tag{2.23}$$

Julienne-Vigue model

Another model that improves the GP model was proposed that is called JV model [44]. The model was added a thermal averaging procedure, used the retarded molecular spontaneous emission decay rates $\Gamma_M(R)$ instead of constant value ($2\Gamma_A$), and employed realistic hyperfine molecular states by taking into account angular momentum quantum number dependence in the survival probability in an excited state S. The JV model agrees well with the GP model when the JV model makes the same approximation as GP model.

In both GP and JP models, the atoms are determined to share the released energy from collision equally. In consequent, a high released energy leads to the trap loss of the both collisional partners.

Landau-Zener transition

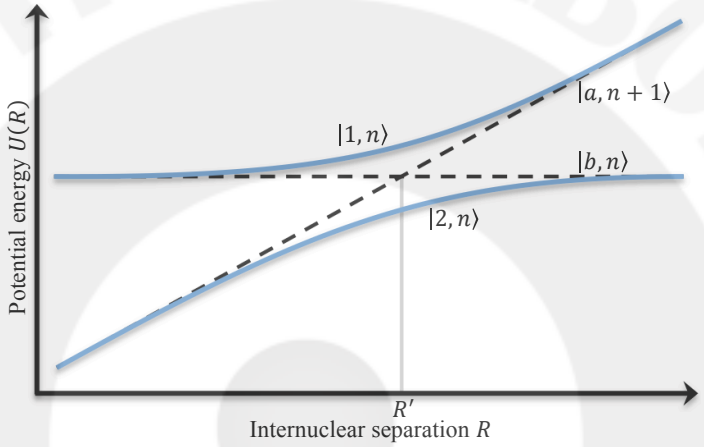

Figure 2.13. Schematic shows the energy levels of the dressed states $|1, n\rangle$ and $|2, n\rangle$ (solid lines) compared with the uncouple levels of the bare states $|a, n+1\rangle$ and $|b, n\rangle$ (dashed lines) as a function of the internuclear separation.

In the coupling region, the atoms may move approach to each other through the region adiabatically following the dressed state level (solid lines). The atoms also have a potential to transition to another dressed state. This mechanism is called Landau-Zener (LZ) transition. The probability of LZ transition can be determine by [43],

$$P_{LZ} = \exp\left(-\frac{2\pi\hbar\Omega^2}{Dv}\right), \tag{2.24}$$

where $D = \left|\frac{\mathrm{d}[U_e(R)-U_g(R)]}{\mathrm{d}R}\right|_{R'}$ is the slope of the difference potential energy at crossing point, R'. Then the probability that the atoms undergo the adiabatic passage [43], is

$$P_A = 1 - P_{LZ} = 1 - \exp\left(-\frac{2\pi\hbar\Omega^2}{Dv}\right). \tag{2.25}$$

Suppose that the atoms approach toward each other in the $|1,n\rangle$ dressed state. There are two pathways that the atoms will end up in $|2,n\rangle$ when they move apart each other. As the atoms pass this coupling region twice (when they are approaching and leaving each other), the atoms may undergo the adiabatic passage through the $|1,n\rangle$ level with the probability of P_A before they LZ transition into the $|2,n\rangle$ level with the probability of P_{LZ}. In the other way, the atoms may transition into the $|2,n\rangle$ level with the probability of P_{LZ} before undergo the adiabatic passage in the $|2,n\rangle$ level with the probability of P_A. In summary, the atoms that start in $|1,n\rangle$ have a probability to end up in $|2,n\rangle$ equal to $2P_{LZ}P_A$ or $2P_{LZ}(1-P_{LZ})$.

2.2.3 Blue detuned light assisted collisions

In a presence of blue detuned light field, the light can prevent atoms from closely approaching each other. This process is known as "optical shielding" and can be described via a semiclassical picture as seen in Figure 2.14. The two approaching atoms in $|S+S\rangle$ (as represented by grey arrow) are excited into $|S+P\rangle$ by absorbing the photon around the Condon point R_c.

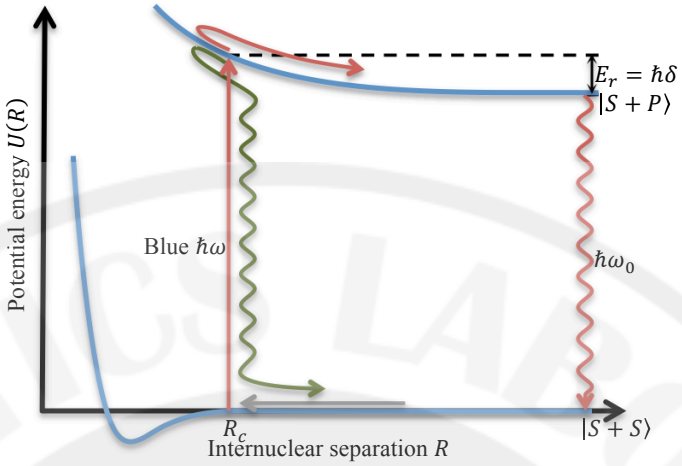

Figure 2.14. Schematic shows a model of collisional process induced by a blue detuned light with the frequency of ω. The quasimolecular energy levels of $|S+S\rangle$ and $|S+P\rangle$ as a function of the internuclear separation R are indicated by the solid blue lines. Grey arrow represents two atoms that approach each other in their ground state. Red and green arrows represent the inelastic and elastic collision between the atoms induced by blue detuned light respectively.

In the excited state, the closer distance between atoms is suppressed due to the repulsive potential. As a result, they move apart and exit either in $|S+P\rangle$ (as represented by red arrow) or in $|S+S\rangle$ (as represented by green arrow). In the case of an exit in $|S+S\rangle$, the released energy for the atoms is equal to zero and the collision then becomes elastic. An inelastic collision occurs when the atoms exit on $|S+P\rangle$. They travel following the repulsive potential; decay to $|S+S\rangle$; and gain the released energy that equals to $\hbar\delta$. That means the energy released from this inelastic collisions could be controlled through the detuning of the light.

CHAPTER 3

PREPARATION OF COLD ATOMS

The usual pathway of the atomic physics experiments starts with preparing a sample of cold atoms. For doing that, the apparatus for cooling and trapping Rubidium-85 atoms was constructed at the Quantum-Atom Optics (QAO) Laboratory. The main parts of the apparatus and their construction are described in Sec. 3.1 of this chapter. The standard technique, magneto-optical trap (MOT), was used for preparing the cold ^{85}Rb atoms. A use of imaging system provided the capability to detect the cold MOT atoms as detailed in Sec. 3.2.

3.1 Apparatus setup for preparing cold ^{85}Rb atoms

For getting the cold ^{85}Rb atoms with a long lifetime, we need to minimize an external disturbance by keeping them in a high vacuum chamber (Sec. 3.1.1). Inside the chamber, the pre-cool Rb atoms released from Rb dispensers were slowed down and confined by using the MOT configuration (Sec. 3.1.2), which consists of a laser system and a pair of magnetic coils.

3.1.1 Vacuum system

The MOT scheme was designed to operate inside a science chamber where was high vacuum by using a set of vacuum pumps as shown in Figure 3.1. The chamber made from the Synchrotron Light Research Institute (Part No.: SLRI-SW-CMU-540089) has two large ports of an 8-inch ConFlat (CF) flange and eight small ports of a 2¾-inch CF flange. One of the small ports was fitted with the Rb dispensers for ejecting Rb atoms into the chamber; another small port was connected with the series of the vacuum pumps; and all of the left ports were fitted with the MDC zero profile viewports (Part No.: 450008 and 450002). The viewports have the flat optical windows that allow us to apply the cooling beam into the chamber through these ports. When the beams were shined, the cold ^{85}Rb atoms were accumulated inside the chamber where the two magnetic coils were mounted outside on the two big ports.

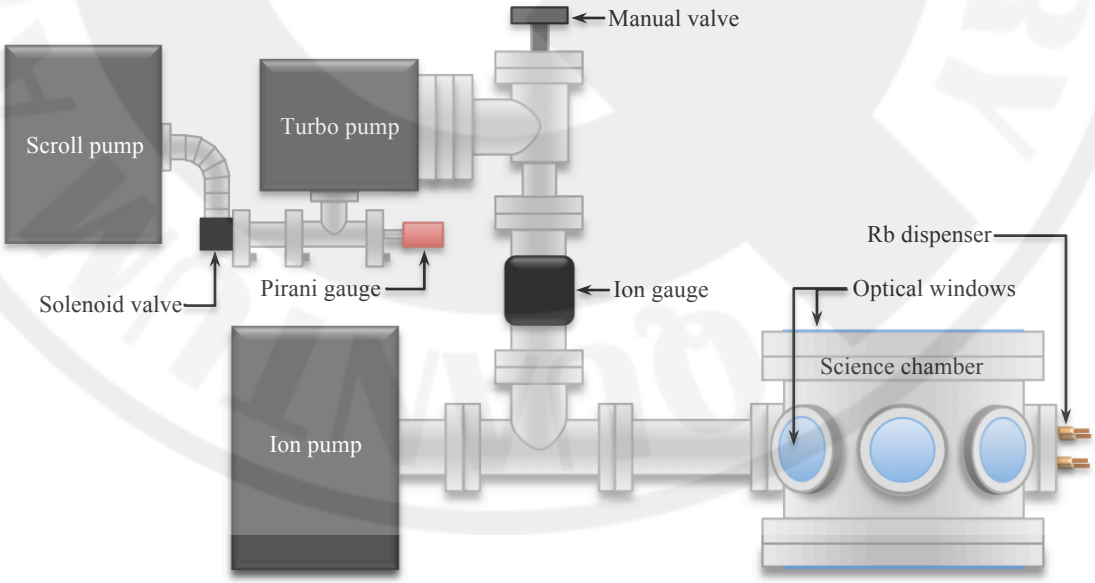

Figure 3.1. Top-view schematic of the vacuum system shows the science chamber connected with pumps, gauges, valves, and Rb dispenser.

For the atomic source, the dispensers made from SAES (Part No.: RB/NF/3.4/12 FT10+10) were used to provide natural Rb atoms, which consisted of approximately 77.2% ^{85}Rb and 27.8% ^{87}Rb. The three dispensers were mounted with a MDC electrical feedthrough (Part No.: 9452014) where the 6 Amps electric current was applied. Due to heating of the current applying, the dispensers released Rb atoms into the science chamber.

As mentioned before, the science chamber was connected to a high vacuum system. The system based on a Varian Valcon Plus 40 Diode Ion Pump (Part No.: MC-INV-10-11-0118) including a Provac Ion Gauge (Part No.: MC-INV-10-11-0118). The ion pump was operated continuously for keeping the pressure of the system at high vacuum, which was around 5.9×10^{-9} Torr. However, the ion pump could be employed only when the pressure was below the limit of 7.5×10^{-3} torr. Thus other two pumps were needed for operating at the low vacuum pressure. A Kurt J. Lesker Manual Valve (Part No.: SA0150MV CF) was used for isolating these two pumps from the high vacuum part.

The two pumps, an Edwards Dry Scroll Pump (Part No.: A72401903) and an Edwards EXT Turbomolecular Pump (Part No.: B72242000), were used for pumping all of the volume starting from the atmospheric pressure. To connect this low vacuum part to the high vacuum one, the turbo pump was attached to the manual valve. An Edwards Pirani Gauge (Part No.: D02601000) was mounted at the other end of the turbo pump for measuring the low vacuum pressure. Edwards Solenoid Valve (Part No.: C41752000) was then connected to the gauge following with the scroll pump as shown in the figure.

When all parts of the vacuum chamber were assembled, the scroll pump of which an ultimate vacuum is 5.3×10^{-2} torr was firstly turned on. After the vacuum pressure reached the limit of the scroll pump, the turbomolecular pump was turned on for further pumping. The stainless parts of the chamber were baked to 170 ºC for 3 days while both pumps were operating for eliminating the contaminants from the entire chamber. When the pressure of the chamber was reached the limit of ion pump, the pump was turned on, the manual vale was closed, and the turbomolecular pump and the dry scroll pump were turned off. With the ion pump alone, the pressure was reduced to 5.9×10^{-9} Torr with out any vibration.

3.1.2 Magneto-optical trap

As introduced in Chapter 2, the MOT is used as a standard technique for cooling down atoms from the room temperature. This technique relies on the cooperation of the red-detuned laser light and the quadrupole magnetic field that provides the spatial confining force for trapping the atoms. In this section, a laser system and a magnetic system used for experimentally realizing MOT are detailed.

For doing MOT of Rb atoms, the frequency of lasers employed in MOT scheme has to be locked at the transitions of the atoms. Firstly, the energy levels of ^{85}Rb are considered. As the ground electron configuration of the atoms is: $1s^2$; $2s^2$, $2p^6$; $3s^2$, $3p^6$, $3d^{10}$; $4s^2$, $4p^6$; $5s^1$ and the nuclear spin quantum number is $I = 5/2$. Thus the hyperfine energy levels corresponding to the D2-line transitions are as illustrated in Figure 3.2. In MOT operation, there are two necessary lasers of which the frequencies with relevant atomic transitions are also shown in the figure. The first

one is a MOT cooling laser locked to the $F = 3 \rightarrow F' = 4$ transition. The second one is a hyperfine repump laser locked to the $F = 2 \rightarrow F' = 3$ transition.

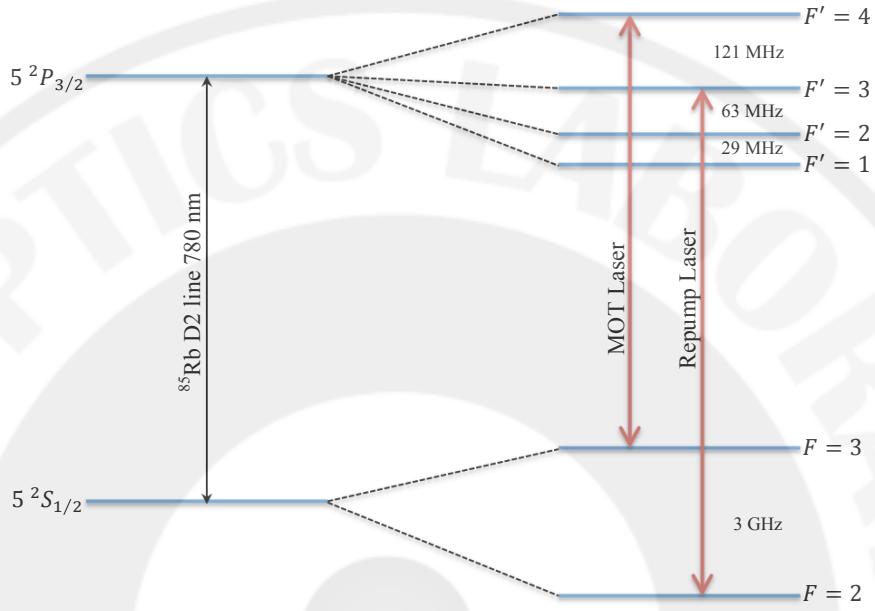

Figure 3.2. The relevant levels of ^{85}Rb for the D2 line transitions involved in the MOT operation.

The cooperation between the MOT laser and the repump laser provides the efficient cooling mechanism because the atoms are driven to be in the cooling cycle all the time of operating MOT. By absorbing photons in the MOT laser beams, the atoms in the $F = 3$ ground state are excited into the $F' = 4$ state. In this excited state, the atoms can decay back to the $F = 3$ state only where interact with the cooling beam again. This mechanism is repeated many times that make the photons can transfer the net of total momentum to the atoms in the direction of the laser beam as described in Chapter 2. However, there is still a chance for an off-resonant excitation of another transition to the $F' = 3$ state as well. In this case, the atoms have a potential to decay to either the $F = 2$ or $F = 3$ ground state. If the atoms decay to

$F = 2$, the atoms are then out of resonance with the cooling laser. To correct this problem, the repump laser was used to excite the atoms from the $F = 2$ state to the $F' = 3$ state. In this excited state, the atoms may decay back to the $F = 3$ ground state where they are in resonance with the MOT laser again.

In the experiment, two external cavity diode lasers (ECDLs), which are the commercial MOT/cooling laser made from MOGlabs and the home-made repump laser were used. The details of the lasers and their frequency control are explained below.

MOT laser

The MOGlabs ECDL (model: ECD-003) with a MOGlabs laser controller and stabilizer (model: DLC-202) provided the cooling beam with an output power of 150 mW (79.16 mW measured with an applied current of 118 mA) at the 780-nm wavelength. The ECDL was built in the Littrow configuration with a diffraction grating placed in front of a laser diode (Part No.: DL-780AP150). The angle of the grating was aligned in such a way that the first-order diffracted beam was fed back into the diode and the zero-order diffracted beam became the laser output beam. As consequence, adjusting an angle of the grating and an external cavity length could vary the wavelength of the laser. The sketch of the MOGLabs laser is shown in Figure 3.3. The coarse adjustment of the wavelength was done by manually tuning a knob of the grating mount that has an adjustment screw with a displacement of 12 nm per full turn. For an electrical control of the wavelength, a piezo actuator mounted at the back of the grating was used to translate the grating for changing the external

cavity length. Thorlabs optical isolator (Part No.: IO-3-780-HP) was placed just in front of the laser to protect its from optical back reflections into the laser cavity.

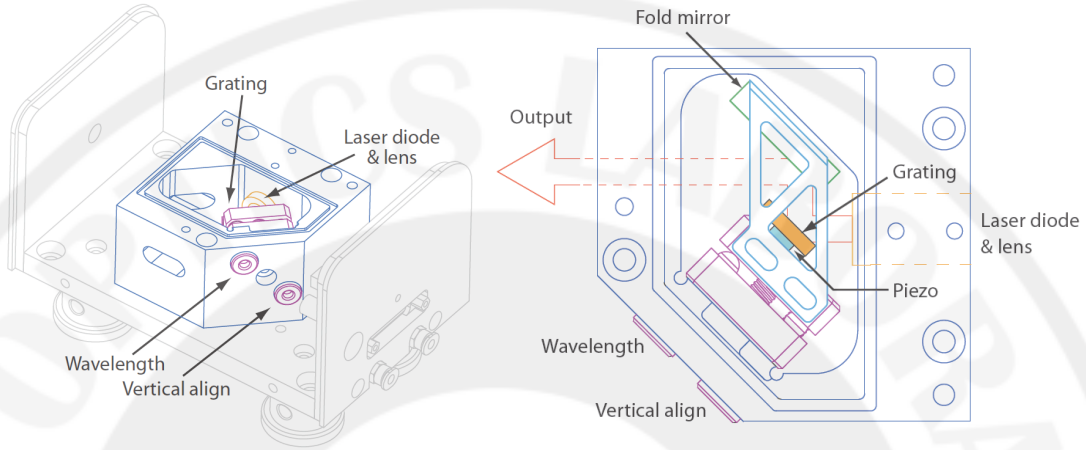

Figure 3.3. Sketch of the MOGLabs ECDL shows the essential components that are the laser diode and lens, the feedback grating mounted on a fine adjustable mount [45].

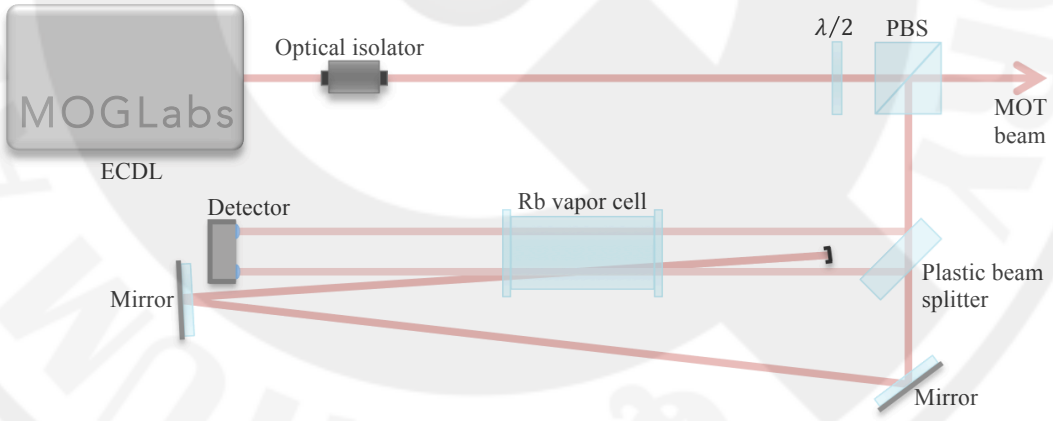

Figure 3.4. Optical alignment for locking the laser frequency to an atomic transition by using the saturated absorption spectroscopy technique.

To lock the MOT laser frequency to the $F = 3 \rightarrow F' = 4$ transition, Doppler-free saturated absorption spectroscopy (DSAS) of the ^{85}Rb atoms was produced. A few mW of the MOT beam was split into the spectroscopy part by using a cooperation

of a half wave plate and a polarizing cube beam splitter (PBS). The split beam was passed though an acrylic beam splitter and then divided into a bright beam and a pair of dimmer beams as shown in Figure 3.4. The dimmer beams were equal in intensity called probe beams. The one that was more intense called a pump beam. The probe beams were delivered through the Rb vapor cell and were received by a MOGLabs photo detector.

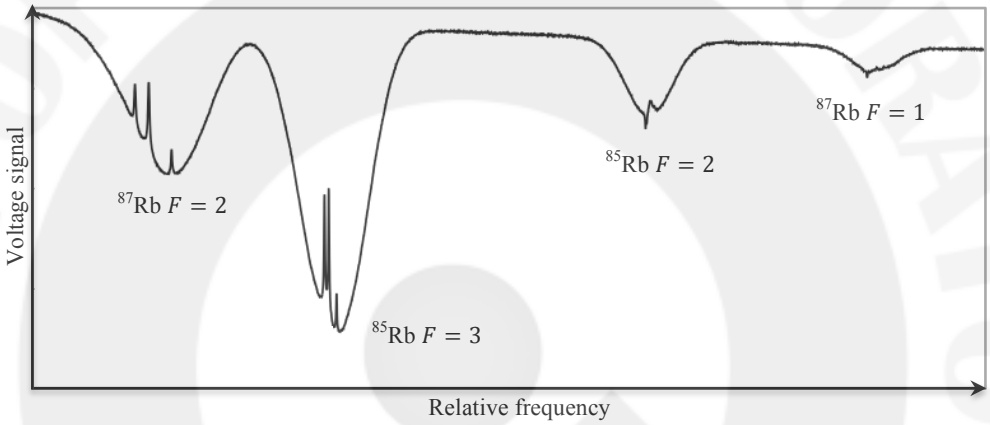

Figure 3.5. The saturated absorption spectrum line of Rb atoms detected from the probe beam with the overlapping pump beam. The voltage signal measured from the photodiode was plotted as a function of the relative frequency of the laser. The entire 780 nm Rb hyperfine structure was shown for both two natural isotopes when the laser frequency was scanned about 10 GHz. This figure is duplicated from [46].

The intensities of the probe beams were monitored as voltage signals, which were monitored by using an oscilloscope. The pump beam was aligned in direction that it overlapped one of the probe beams as much as possible inside the cell. If the laser frequency is scanned about 10 GHz, the spectrum signal of the overlapping probe beam will be as shown in Figure 3.5. The spectrum represents an entire 780 nm Rb hyperfine structure, which consists of the ^{87}Rb transitions from the ground states

with $F = 1$ and 2 to F', the ^{85}Rb $F = 2 \rightarrow F'$transitions (containing the transition for locking the repump laser), and the ^{85}Rb $F = 3 \rightarrow F'$ transitions (containing the transition for locking the MOT laser). For the other probe beam, the detector detects only a Doppler-broadened spectral line profile (linewidth ~1 GHz) due to a nonzero velocity of the Rb atoms in the cell.

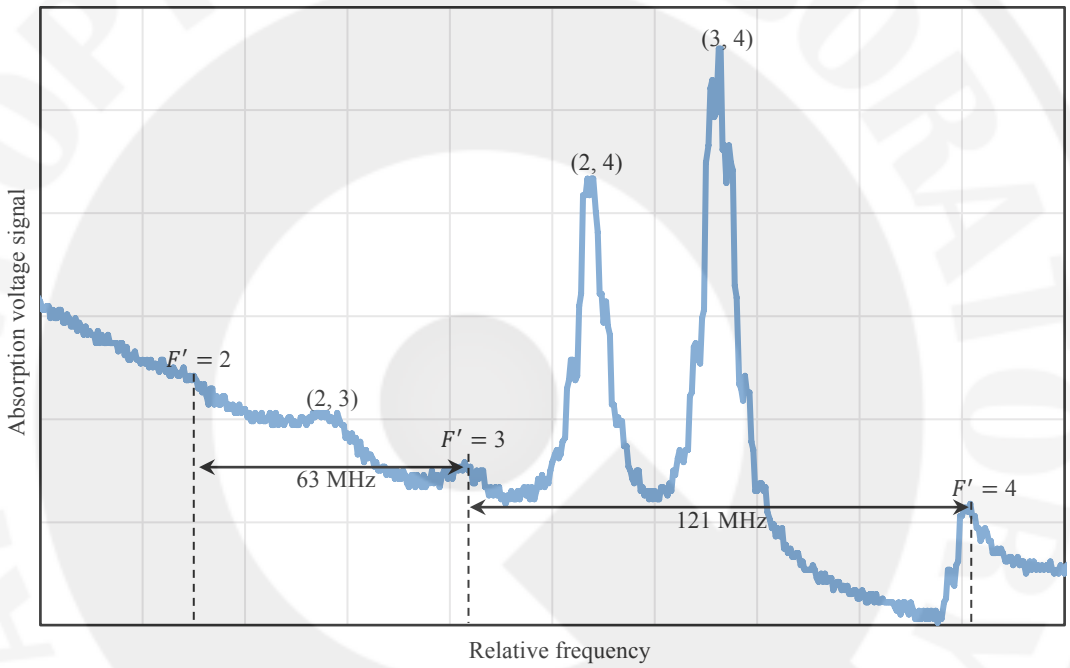

Figure 3.6. The absorption voltage signal is plotted versus the relative frequency of the laser. For narrow scanning, the spectrum of the ^{85}Rb $\boldsymbol{F = 3 \rightarrow F'}$ hyperfine structure is represented.

The appeared hyperfine structure can be explained as the following. The pump beam with high intensity saturates the atomic population in the excited state when the beam frequency is on resonance. As consequence, the probe breaches through the vapor cell easily with minimal absorption resulting in a voltage peak in the middle of the Doppler profile. The peak signal also corresponds to the group of

atoms, which has zero velocity along the probe beam. The observed hyperfine structure peaks/lines of the $F = 3 \rightarrow F'$ transitions are shown in Figure 3.6.

As mentioned before, the frequency of MOT laser need to be detuned a little below the $F = 3 \rightarrow F' = 4$ transition. The peak was used to give an error signal for locking and stabilizing the laser frequency. From the error signal, the controller generated a feed back signal to the laser through either the piezo actuator voltage or the laser diode current. To make the laser consistent enough for locking its frequency, a temperature of the laser was stabilized at 21 ºC along the operating time.

Repump laser

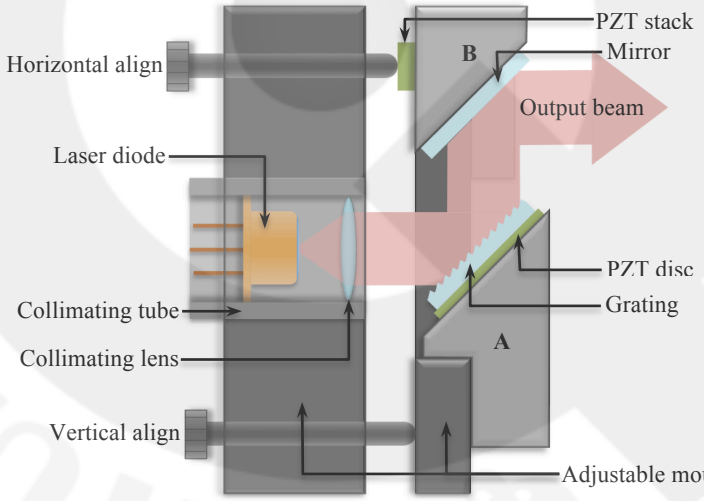

Figure 3.7. Sketch of the home-built ECDL shows the essential components that are the laser diode and lens, the feedback grating mounted on the adjustable mount.

The Repump laser was built by using the Littrow configuration [47] as illustrated in Figure 3.7. A Thorlabs laser diode (Part No.: L785P100) was used for providing a 780 nm beam with an output power of 90 mW. An electric current was applied to the

diode by using a home-built driver and stabilizer [48]. For getting the collimated output beam, the laser diode and a lens were mounted inside a collimating tube (Thorlabs, Part No.: LT110P-B).

For frequency control, the other parts of the laser were assembled as following. A Newport grating (Part No.: 33001FL02-330H) attached on the stack of three piezoelectric transducer (PZT) discs was mounted on an aluminum piece A. The collimating tube and the piece A were installed on a Newport adjustable mount (Part No.: U100-P) with two knobs (Part No.: AJS100-0.5K) as shown in the figure. A PZT stack was installed at the end of the horizontal knob for finely tuning the wavelength. Finally, a mirror attached on aluminum piece B was installed in front of the grating for fixing the direction of the output beam during changing the grating angle.

For stabilizing the laser frequency, the frequency was calibrated against the ^{85}Rb hyperfine structure lines obtained from the Doppler-free saturated absorption spectroscopy. A photograph of the optical alignments of the spectroscopy is shown in Figure 3.8. As the result, the hyperfine structure lines of the ^{85}Rb $F = 2 \rightarrow F'$ transitions obtained from an oscilloscope are shown in Figure 3.9. This provided the error signal, which was sent to the home-built driver and stabilizer for locking the laser frequency.

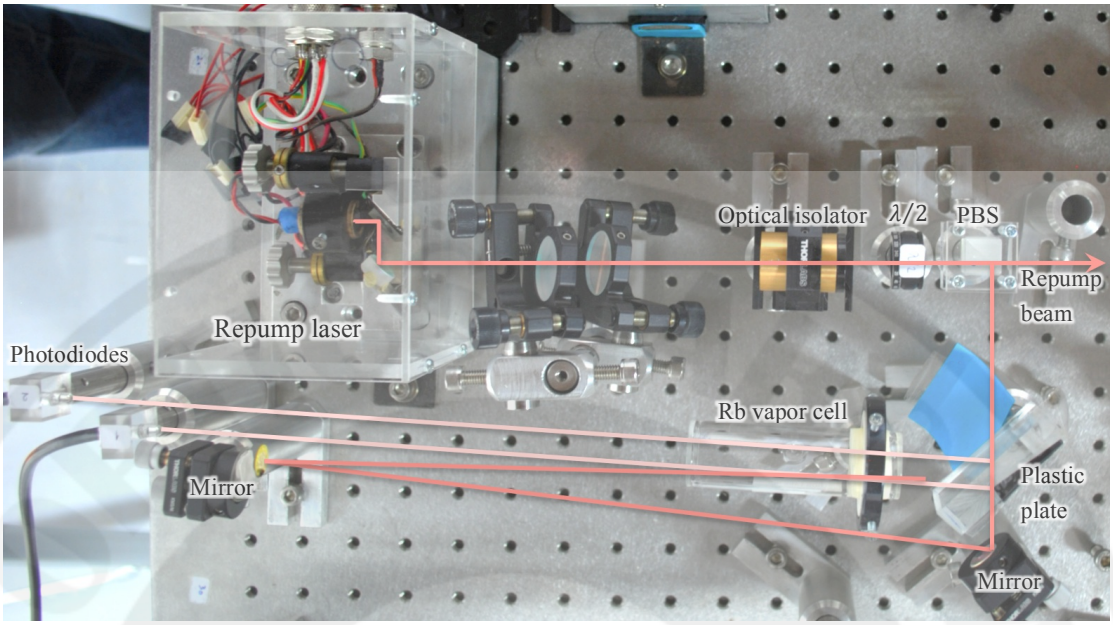

Figure 3.8. Repump laser and its optical alignment for Doppler-free saturated absorption spectroscopy.

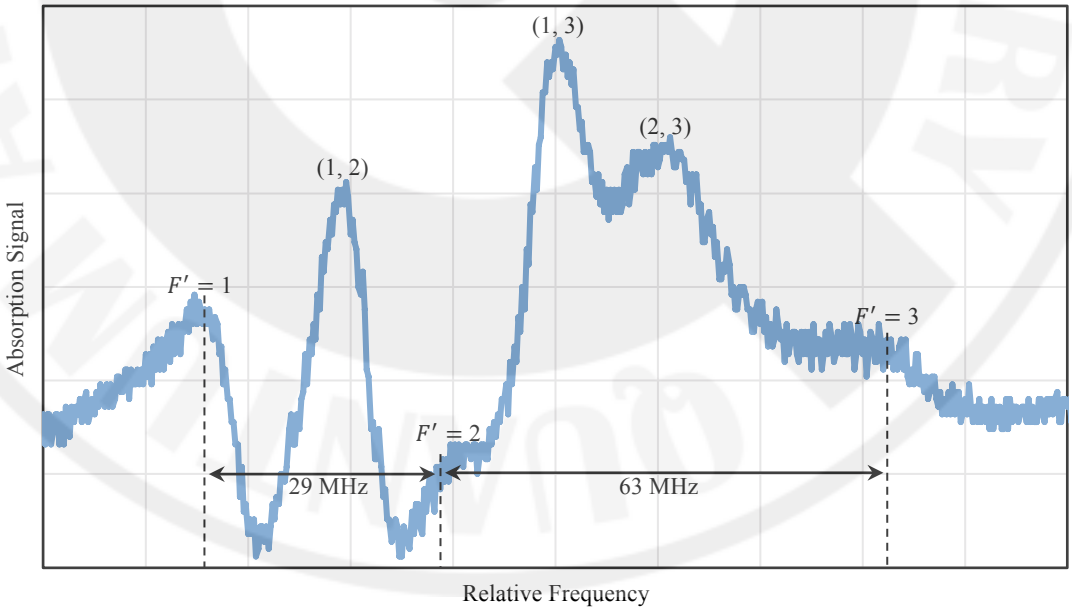

Figure 3.9. The absorption voltage signal is plotted versus the relative frequency of the laser. For narrow scanning, the spectrum of the ^{85}Rb $\boldsymbol{F = 2 \rightarrow F'}$ hyperfine structure is displayed.

Magnetic coils

Two coils of copper wire were performed to produce the quadrupole magnetic field necessary for the atomic confinement in the MOT configuration. Each coil consisted of 102 turns of a SWG#14 wire with an inner diameter of 210 mm. The coils were attached at the two big ports of the science chamber and separated by 70 mm from each other as seen in Figure 3.10. To load the MOT, a current of 9 A was applied to the coils that provided the magnetic field gradient of 8 Gcm^{-1} in the axial axis of the coils.

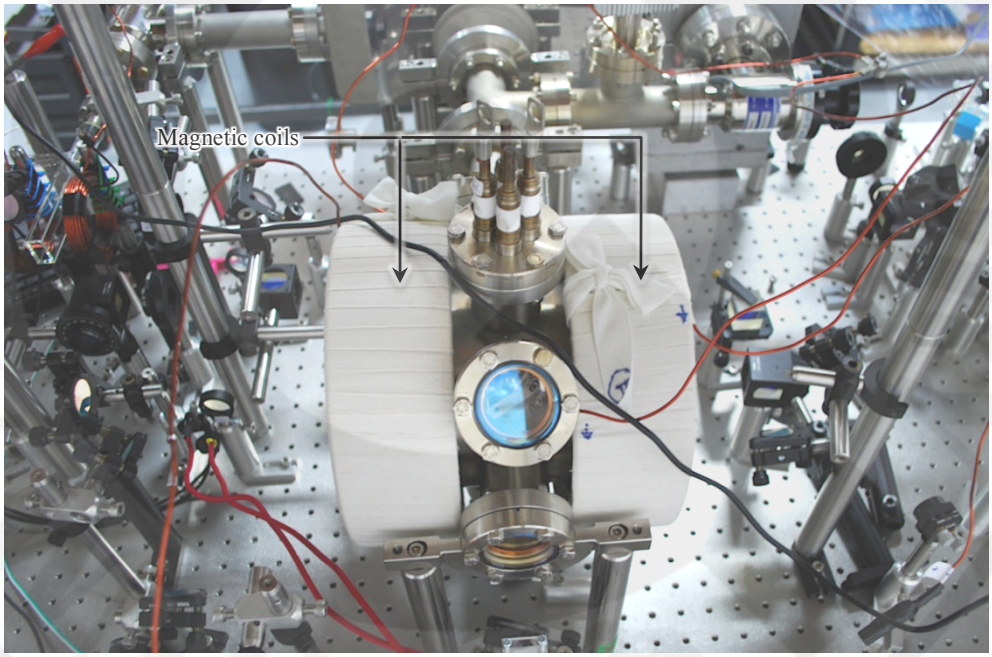

Figure 3.10. The magnetic coils attached on 8-inch ports of the science chamber.

MOT alignment

As mentioned before in Chapter 2, the MOT system consisted of the quadrupole magnetic field and the six MOT (and repump) beams for trapping and cooling Rb

atoms in three dimensions. The magnetic field was created from the quadrupole coils detailed above. The MOT laser and the repump laser were operated to generate the six cooling beams. The top view of the schematic of our MOT alignment and the necessary apparatus is illustrated in Figure 3.11 where the magnetic coils and some wave plates for the cooling beams are not shown.

The MOT alignment began with combining the MOT beam and the repump beam by sending the beams pass through two half-wave plates and a PBS as shown in the figure. The orientations of the linear polarizations of the beams were chosen by tuning the wave plates in such the way that both beams propagate in the same direction after they pass through the PBS. This combined MOT/repump beam was expanded into one-inch diameter beams by using a pair of lens with $f = 25$ and 250 mm. The MOT/repump beam was split into three beams equally by using two pair of half-wave plates and PBSs. Each beam originally linearly polarized was passed through a quarter-wave plate and turned into a right-handed circularly polarized beam for the MOT configuration. Many mirrors were used for steering all three beams to be mutually perpendicular as labeled with $\sigma_{+,x}$, $\sigma_{+,y}$ and $\sigma_{+,z}$ in the figure, where the subscripts of x, y and z represent the axis in three dimensions. Then each beam was passed through another quarter wave plate before was retro reflected by a mirror and passes through the wave plate again. Due to double passing the quarter wave plate, the reflected beam turned into a left-handed circularly polarized beam. These six crossing MOT/repump beams with proper circular polarization were intersected in the center of the science chamber where the magnetic trap potential was minimum.

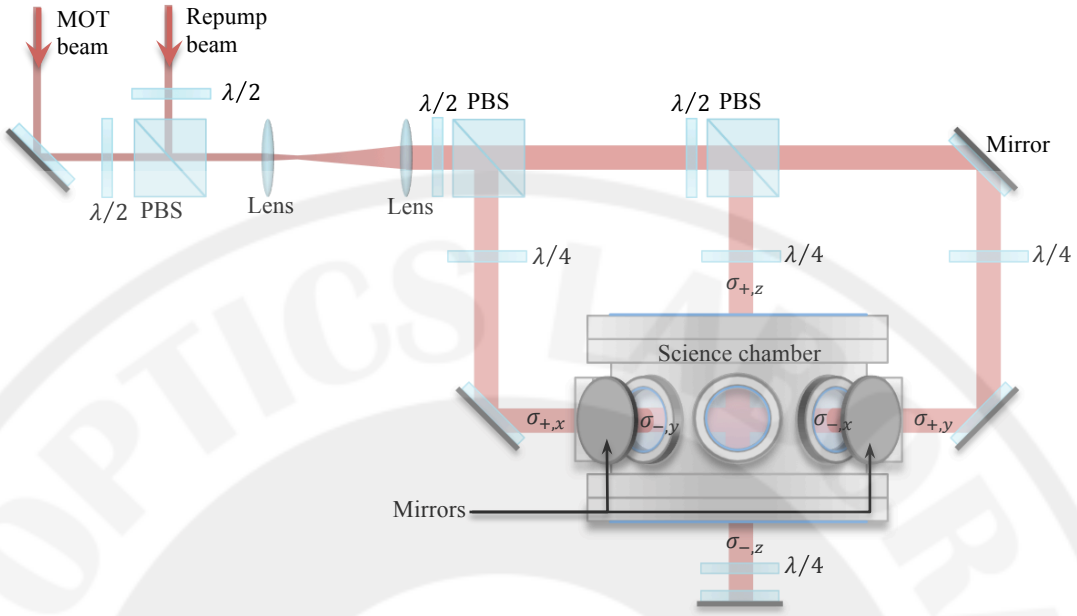

Figure 3.11. Schematic of our MOT apparatus (top view). The quadrupole magnetic coils and some wave plates of the cooling beams are not shown.

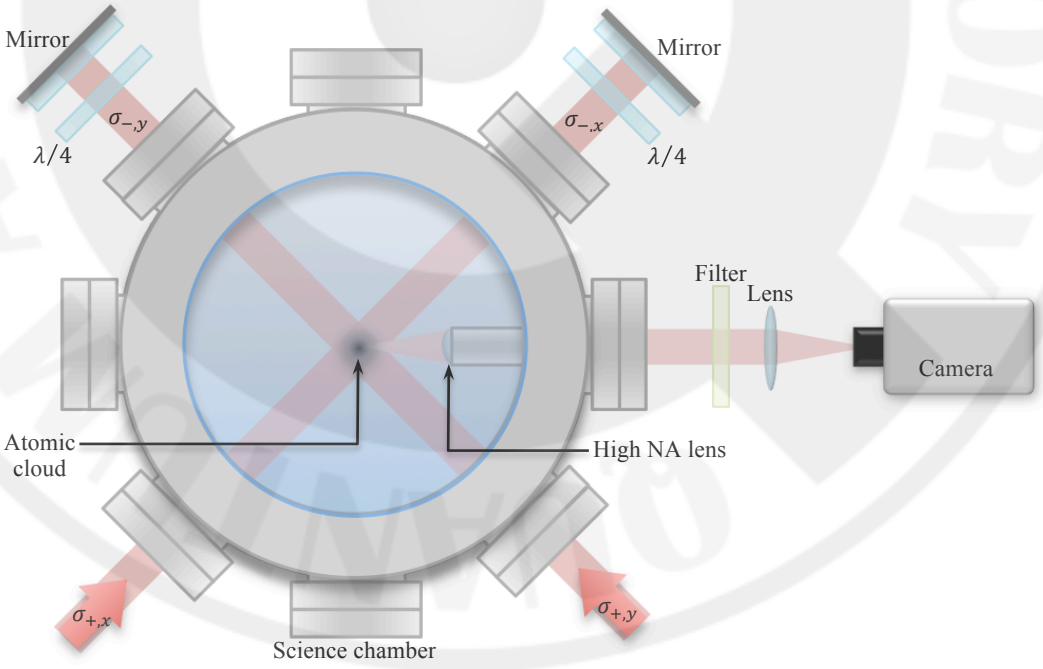

Figure 3.12. Side view of the optical layout shows an alignment of the fluorescence imaging system (the $\boldsymbol{\sigma}_{-,z}$ and $\boldsymbol{\sigma}_{+,z}$ beams are not shown). The system consists of a pair of lens, a filter and a high sensitivity CCD camera.

3.2 Magneto-optical trap detection

The cooperation between the laser system and the magnetic system supplied cold MOT atoms inside the science chamber. For detecting the atoms, the fluorescence imaging was chosen because this technique could be setup conveniently and gives us the sufficient information. An optical layout for the imaging system is shown in Figure 3.12. While the MOT was operating, the confined atoms absorbed photons from the six MOT beams and then emitted photons spontaneously in a random direction. A high numerical aperture (NA) lens from Thorlabs (Part No.: C240TME-B) was mounted on an aluminium tube inside the chamber to collect the photons. The collected photon beam passed through a 780 nm bandpass filter for reducing the unwanted light and focused to a pco. CCD camera (Type: sensicam qe, Part No.: 672 LS 4912) for recording the photons in real time.

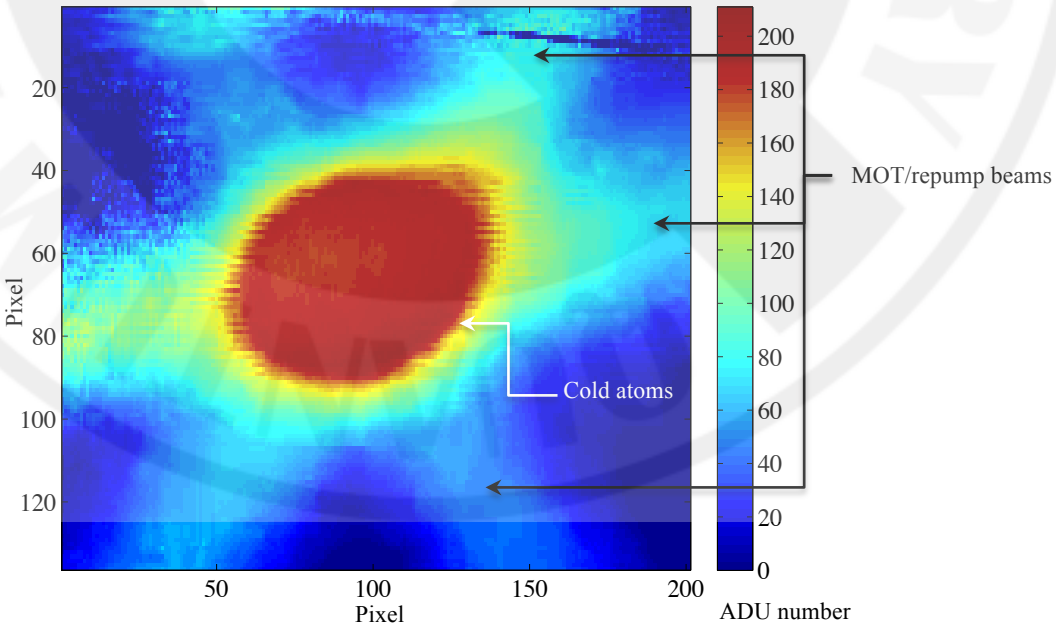

Figure 3.13. Image of the cold atomic cloud inside the vacuum chamber.

The video signal from the CCD camera was sent into the control computer to display and record the fluorescence of the atoms. As the result, the image of the cold atoms trapped in MOT is shown in the Figure 3.13. The image of background light is subtracted from the original image of the MOT cloud that left only the emitted photons to be displayed. The color of each pixel is indicated the collected light intensity of the atomic fluorescence of each pixel in an analog-to-digital unit (ADU), which is shown in the color bar. The red cloud at the center of figure represents the dense cold atoms trapped at the crossed section of the MOT/repump beams.

CHAPTER 4

LOADING ATOMS INTO DIPOLE TRAP

After the preparation of cold Rb atoms was achieved at the QAO Laboratory, I worked on the preparation of a single atom in an optical dipole trap and studied the two-body collisions of cold ^{85}Rb atoms by using an apparatus at the Otago Atomic Physics Laboratory at the University of Otago in New Zealand. In this chapter, the apparatus setup including the methodology for loading cold Rb atoms into an optical dipole trap are reported in Sec. 4.1 and the result of detection of the atoms in the trap is represented in Sec. 4.2.

4.1 Apparatus for loading the dipole trap

The main parts of the apparatus for cooling and confining ^{85}Rb atoms in the dipole trap or the far-off-resonance optical trap (FORT) are reported. This section begins with the details of the vacuum system in Sec. 4.1.1 and the cooling system in Sec. 4.1.2, which are similar to the system in QAO Laboratory. Using the vacuum and cooling systems loaded cold MOT atoms. Consequently, the atoms were transferred into the far-off-resonance dipole trap (FORT) via the compressed MOT (cMOT) and the following optical molasses. The atoms in FORT were observed by using an imaging stage. The details of the dipole trap and the imaging system are provided in Sec. 4.1.3 and Sec. 4.1.4 respectively.

4.1.1 Vacuum system

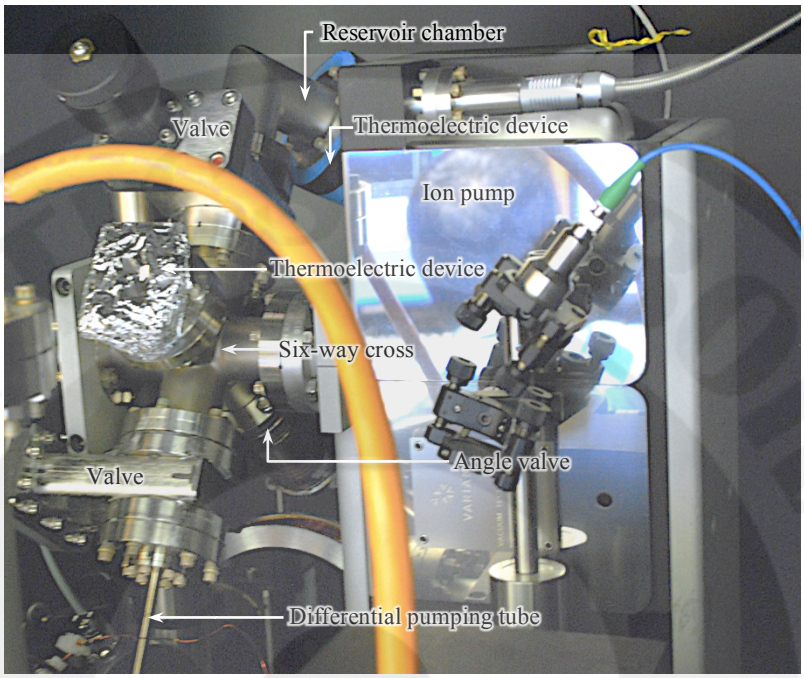

Figure 4.1. Photograph showing the schematic of the Rb source system. The Rb atoms in reservoir chamber are fed into the science chamber through a differential pumping tube.

As described before in Chapter 3, it is necessary to prepare the cold ^{85}Rb atoms in the vacuum system. This vacuum system is divided in two parts, an Rb-atom reservoir and an ultra-high vacuum (UHV) system. For the atom reservoir, a 1 g of natural Rb metal was put in a reservoir chamber, of which temperature were controlled by a thermoelectric device (see Figure 4.1). Adjusting the temperature could change the evaporation rate of the Rb atoms. To separate this chamber, a MDC gate valve (Part No.: GV-1500M) was mounted at the reservoir chamber as shown in the figure. The other end of the vale was connected to a six-way cross where the evaporated Rb atoms (from the reservoir chamber) were accumulated inside. One port of this cross

was connected to an Agilent VacIon Plus 20 Diode Ion Pump for keeping high vacuum. The other ports were connected to the second thermoelectric device for controlling temperature, an MDC angle valve (Part No.: MAV-150V) for installing a turbo-molecular pump and the second gate vale for isolating this Rb source system from a science chamber. This Rb source system fed the atoms into the UHV part through a home-built differential pumping tube.

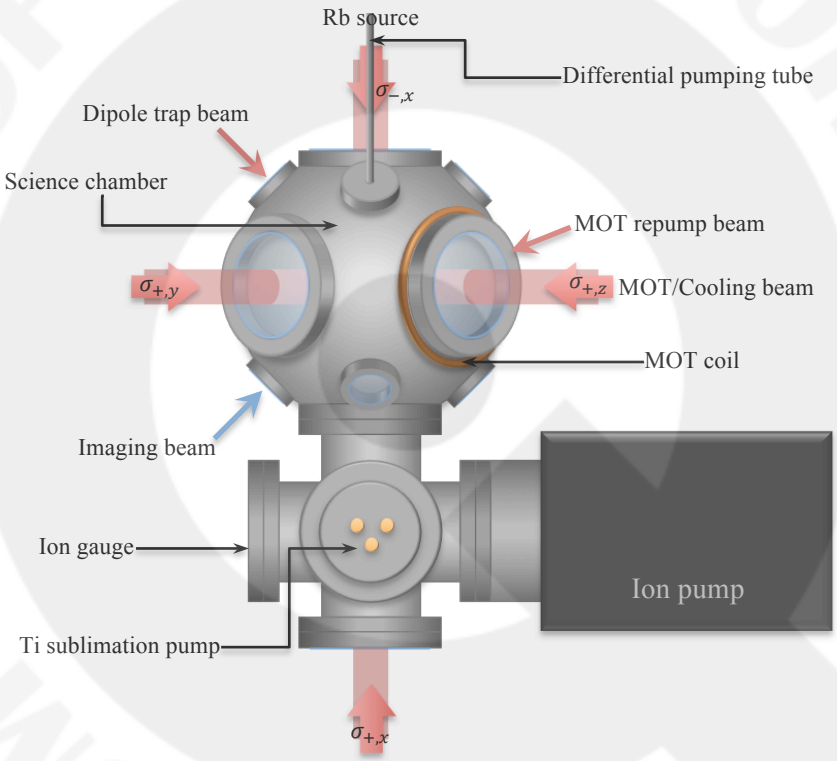

Figure 4.2. The schematic of vacuum system consists of the science chamber where the cold atoms are studied, Ti sublimation pump, Ion pump, and the differential pumping tube connected with the reservoir chamber.

Figure 4.2 shows a schematic of the UHV system. Below the Rb source system, there was a science chamber where the cold atoms were loaded. The chamber was a Kimball $2\,{}^{3}/_{4}$ multi-CF spherical cube (Part No.: MFC275-ESC608). It

consisted of six ports of a $2\,^{3}/_{4}$-inch CF flange and eight ports of an $1\,^{1}/_{3}$-inch CF flange. One of the $1\,^{1}/_{3}$-inch port was connected to the differential pumping tube as mentioned before, another one was fitted with a high numerical aperture (NA) lens used for the dipole trap formation, and the others were fitted with anti-reflection coated view ports. Five of the $2\,^{3}/_{4}$-inch ports were also fitted with the view ports. A six-way cross was mounted on the last $2\,^{3}/_{4}$-inch port for connecting the science chamber to a Vacuum Generators ST22 Titanium (Ti) Sublimation pump, an Agilent VacIon Plus 75 Starcell Ion pump, and a SenTorr Ion Gauge. One port of the six-way cross was fitted with the view port where a laser light was applied into the science chamber as shown in the figure. For keeping the pressure of the UHV system in the order of 1×10^{-11} Torr, the Ion pump was left on all the time and the Ti sublimation pump was weekly used by applying the current of 46 A for one minute.

4.1.2 Cooling system

For loading atoms into the dipole trap, it is necessary to start with loading the MOT, of which the process was the same as detailed in Chapter 3. Two lasers were needed for generating the MOT/cooling beams and the MOT repump beam. A Toptica TA-100 ECDL with a tapered amplifier was used to provide the MOT/cooling beam. As shown in Figure 4.3, the laser beam with a measured power of about 356 mW at 780 nm wavelength was split a few mW into a DSAS part for locking the laser frequency at the crossover peak between the $F = 3 \rightarrow F' = 4$ and $F = 3 \rightarrow F' = 3$ D2 lines. Before the split beam went into the spectroscopy alignment, its frequency was shifted down twice the modulating frequency by double passes the first acousto-optical

modulator (AOM1) with a center frequency (CF) of 110 MHz from ISOMET (Part No.: 1206C). A homebuilt driver was used for modulating this AOM1.

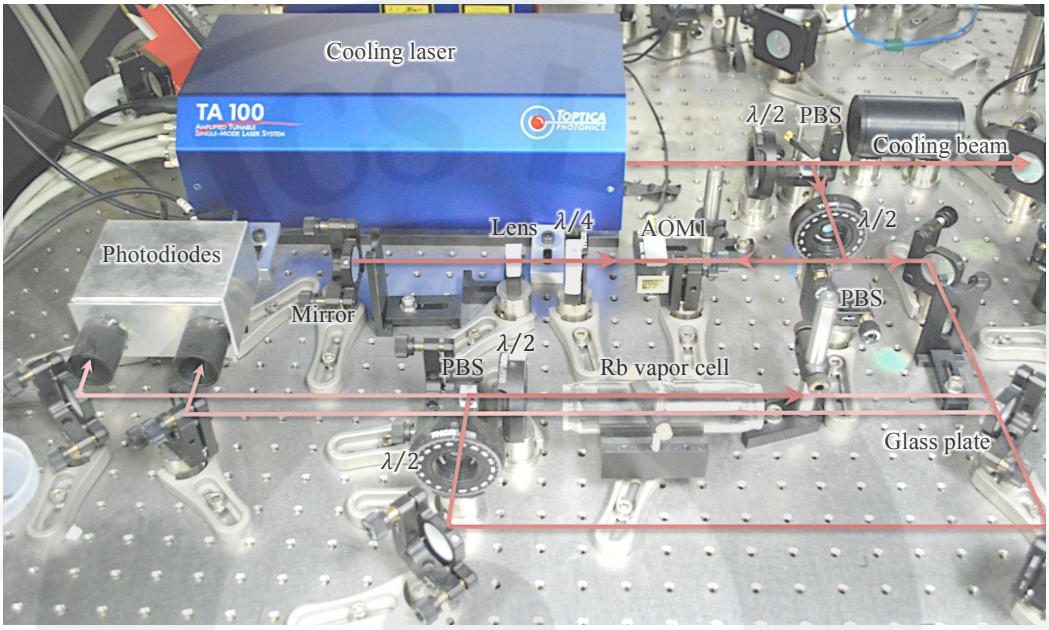

Figure 4.3. Photograph showing the spectroscopy for cooling laser stabilization.

During the experimental operation, it was necessary to shift the frequency of the cooling beam without changing the beam alignment. For doing that, the cooling beam was passed twice an AOM2 with a 75 MHz CF from Interaction (Part No.: ATM-751A2) as seen in Figure 4.4. An Interaction Model DE driver was employed for modulating the AOM2. After passing the AOM2, the beam was passed another Interaction AOM, or AOM3 used for fast switching the beam power. The first order of the cooling beam propagated through a mechanical shutter while the zero and other orders were blocked. All drivers received voltage signals from a computer control, for adjusting both the frequency and the intensity of the beams. Finally, the beam was sent through a half-wave plate and a PBS to align the direction of the linear polarization before it was coupled into a single mode fiber.

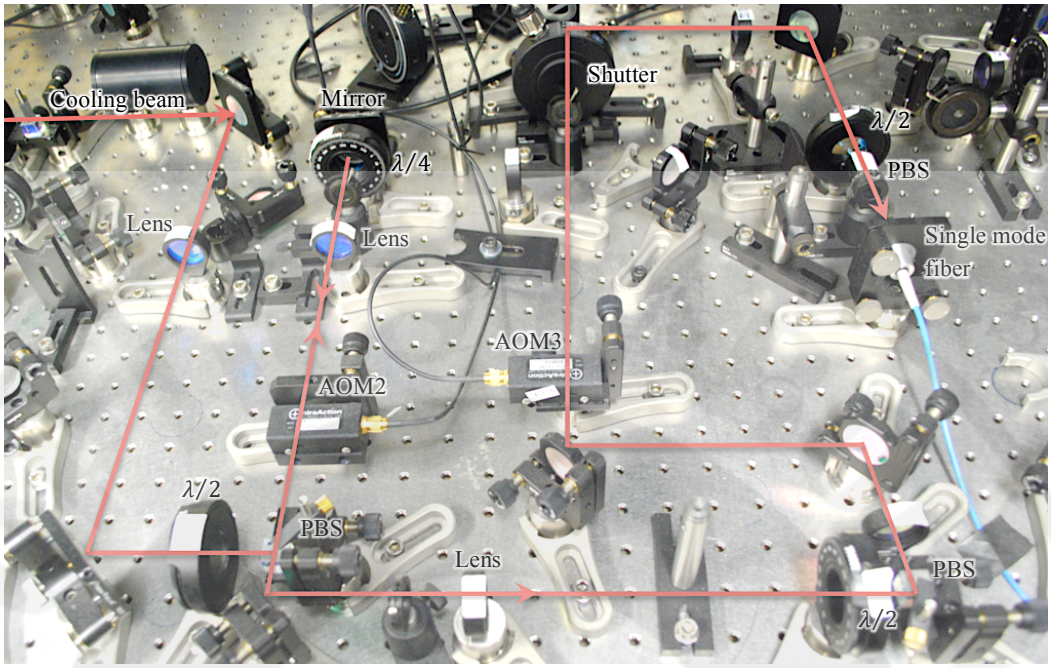

Figure 4.4. Photograph showing the optical alignment for shifting the beam frequency and switching the cooling beam by using AOMs.

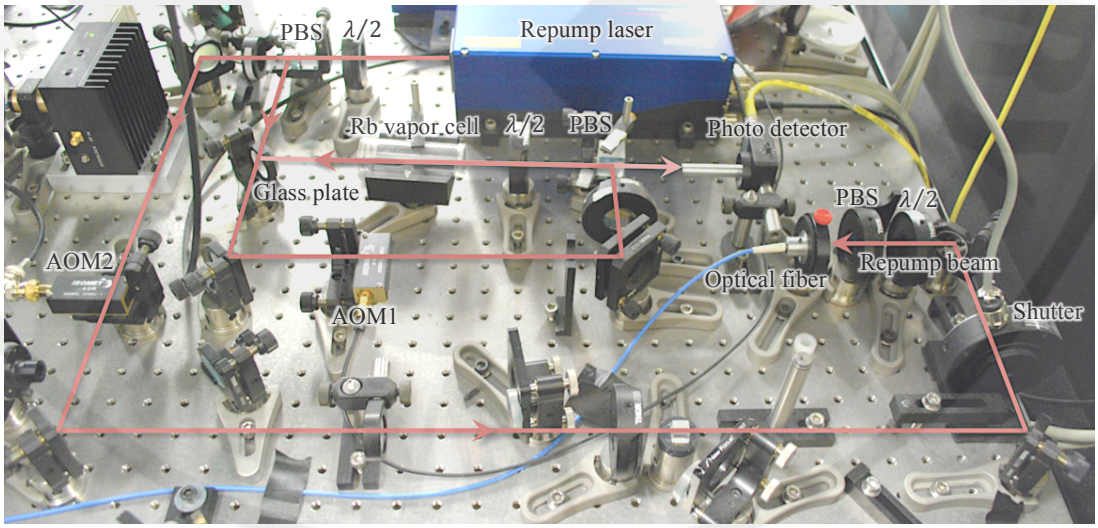

Figure 4.5. Photograph showing the optical alignment of locking and shifting the frequency for the repump laser.

For generating the MOT repump beam, a Toptica DL Pro ECDL was used as shown in Figure 4.5. The repump frequency was lock at a crossover peak between the $F = 2 \rightarrow F' = 2$ and $F = 2 \rightarrow F' = 3$ D2 lines by using PSAS. An AOM1 driven by a home-built modulator was put in the spectroscopy alignment. This gave us the shifted frequency of the repump beam that was equal to half of the modulating frequency of the AOM1. In this spectroscopy, only single photo detector was used that provided the absorption signal with the Doppler profile. The remaining repump beam was passed another AOM2 with 80 MHz CF from ISOMET (Part No.: 1205C-1) driven by another home-built modulator before propagated trough a mechanical shutter and was coupled in to a single mode fiber.

To calculate the cooling beam and the repump beam detunings from the $F = 3 \rightarrow F' = 4$ D2 line transition and the $F = 2 \rightarrow F' = 3$ D2 line transition respectively, the frequency shifting due to the locking point and the three AOMs was accounted that is:

δ_{MOT} = Lock frequency ($= -60.3$ MHz) – 2×AOM1 + 2×AOM2 + AOM3,

δ_{rep} = Lock frequency ($= -31.5$ MHz) – $\frac{1}{2}\times$ AOM1 + AOM2.

After the MOT/cooling beam propagated through the optical fiber, the fiber steered the beam to where the science chamber was. The output beam from the other end of the fiber was split equally into three beams. The MOT beams were aligned quite similarly as for loading the MOT of the QAO Laboratory detailed in Chapter 3. The alignment of the MOT beams for passing through the view ports of the science chamber is shown in Figure 4.2. The repump beam output from the fiber was directly

passed through one of the chamber windows. All beams were intersected at the center of the chamber where a magnetic trap potential was minimum. The magnetic field was created by using a pair of magnetic coils mounted on two $2\,^3/_4$-inch flanges. The coils consisted of 30 turns of copper wire with a radius of 6.5 cm. The current of 31 Amps was applied for providing the magnetic field gradient of 7.7 Gcm^{-1} in the axial axis of the coils. The MOT was loaded for 50 ms by using the parameters of the light beams and the magnetic field gradient as detailed in Table 4.1 (the MOT powers mentioned are the measured power from only one of the MOT beams). Loading more atoms into the MOT with longer time (more than 2 second) does not lead to a significant increase in the number of atoms transferred to the FORT due to the tiny size of the FORT.

Table 4.1. The cooling process with used parameters (the detuning and power of the beams and the magnetic field gradient) for loading Rb atoms into the FORT.

Process	Duration	MOT/cooling beam	Repump beam	Magnetic field gradient
MOT loading	50 ms	-14 MH, 4.5 mW	-5 MHz, 12 mW	7.7 Gcm^{-1}
Ramp to cMOT	1 ms	↓	↓	↓
cMOT1	149 ms	-22 MH, 2 mW	-5 MHz, 2 mW	10.2 Gcm^{-1}
cMOT2	1 ms	-22 MH, 2 mW	-5 MHz, 2 mW	↓
Ramp to Molasses	2 μs	↓	↓	Off
Molasses1	3 ms	-43 MH, 1 mW	-5 MHz, 2 mW	Off
Molasses2	2 ms	1 mW→Off	2 mW→Off	Off

After the MOT stage, all of the parameters were ramped into the values used in a cMOT loading within duration of 1 ms. In the cMOT, the atoms were cooled by using the further detuning of MOT beam and the lower repump power. At the same time, the atomic cloud was spatially compressed by the high magnetic field gradient. At the end of cMOT, the magnetic field gradient was ramped down until it was vanished. Finally, the MOT detuning was further adjusted and also reduced the power to load an optical molasses for 3 ms. All of the beams were then completely turned off in 2 ms at the end of the molasses loading. During this cooling and loading process, the dipole trap was left on all the time. As a result, the average of 10 to ~200 ^{85}Rb atoms were loaded into the trap depending on the MOT stage duration. The setup and calculation for the dipole trap is explained below.

4.1.3 Optical dipole trap

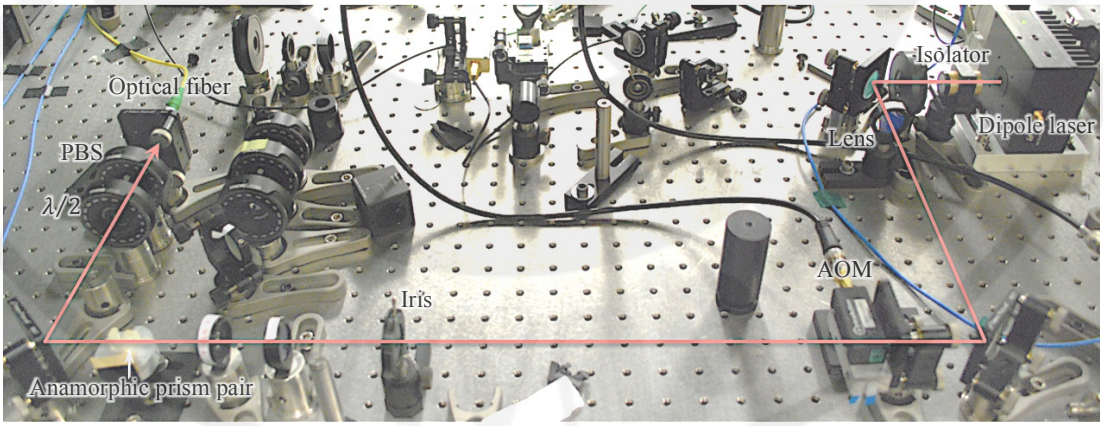

Figure 4.6. Photograph showing an optical alignment of switching AOM for a dipole laser.

To create the FORT, a far-red detuned light was focused by using the high NA lens mounted inside the science chamber. As mentioned before in Chapter 2, the atoms can be attracted into where the intensity of the red-detuned light is highest. In this experiment, a Sanyo laser diode (Part No.: DL8142-201) driven by a Thorlabs current and temperature controller (Part No.: ITC510) provided the dipole light beam at 828 nm wavelength. The beam propagated through an Interaction AOM (Part No.: ATM-1501A2) that acted as a fast switch for the beam. Amplitude of the AOM modulation was controlled by the voltage signal sending from the computer. The first order of the beam was passed through a pair of anamorphic prism for reducing an ellipticity of the beam before be coupled into an optical fiber.

After the dipole beam left the optical fiber, the beam emitted from the other end of the fiber was propagated through the high NA lens made from LightPath Technologies (Part No.: 352230). As consequence, the dipole beam with the power of 30 mW was focused at the center of science chamber where the MOT cloud was formed. The beam waist, w_0, was measured by directly imaging the focus of the beam. The Gaussian fit to the measured waist gives us the value of 1.8 μm.

The intensity distribution of the beam was calculated as a Gaussian beam, which is:

$$I(r,z) = \frac{2P}{\pi w^2(z)} \exp\left(\frac{2r^2}{w(z)}\right), \tag{4.1}$$

where r is the radial distance from the center axis of the beam, z is the axial distance from the beam waist, and P is the power of the beam. Hear the beam radius is given

by $w(z) = w_0\sqrt{1+\left(\frac{z}{z_R}\right)^2}$, where $z_R = \pi w_0^2/\lambda$ is called Rayleigh range. From the intensity distribution, the energy shift was calculated by using equation (2.13) in Chapter 2. Where the Rabi frequency can be determined from $\sqrt{\frac{3\lambda^3\Gamma I}{4\pi^2\hbar c}}$, the energy shift is

$$\Delta E_i = \frac{3\pi c^2\Gamma}{2\omega_0^3} I(r,z) \sum_j \frac{C_{ij}^2}{\delta_{ij}}. \tag{4.2}$$

The spatial dependent light shift of the energy level relative with the $F = 2$ and $F = 3$ ground states is represented in Figure 4.7. This shows a potential well with the depth of $U_0 = h \times 85$ MHz corresponding with the trap depth of 4.1 mK.

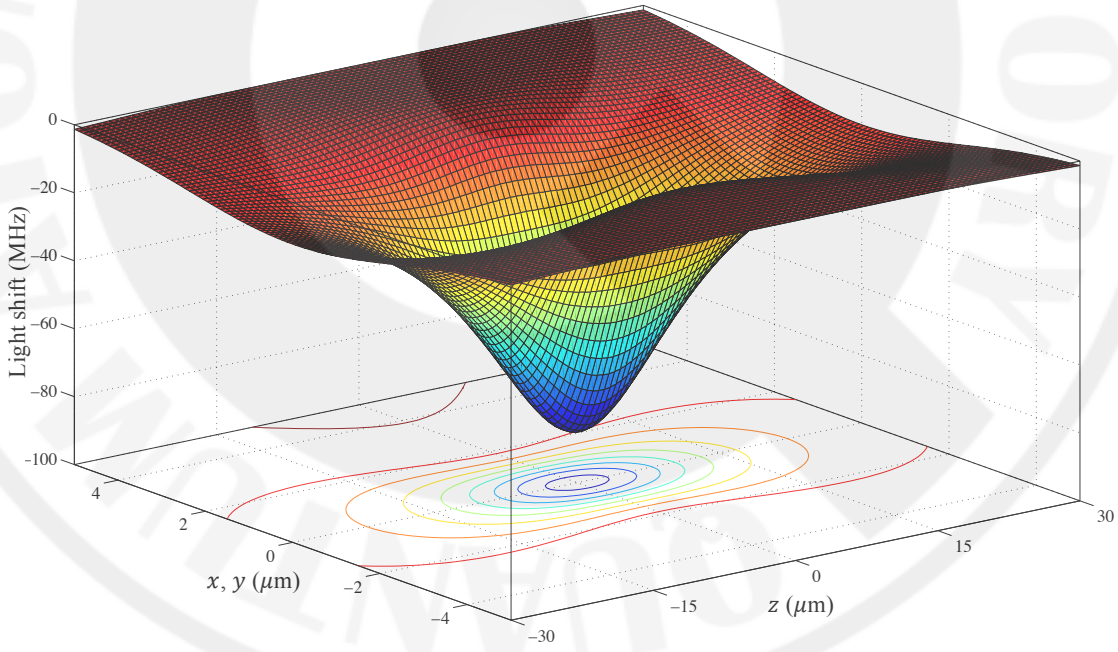

Figure 4.7. The energy shift of the atomic ground state plot as a function of the x, y and z positions where the origin is at the beam focal point.

In the FORT, the most trapped atoms took nearly all of the time around the bottom of the potential well or the center of the trap because the temperature of the atoms was very low (about 300 μK) compared with the trap depth. For this reason, the detuning of the lasers was included the maximum energy shift at the center of the dipole trap. The light-shifted-energy levels of the D1 and D2 lines are shown in Figure 4.8. The color arrows represent the relevant transitions used in the research.

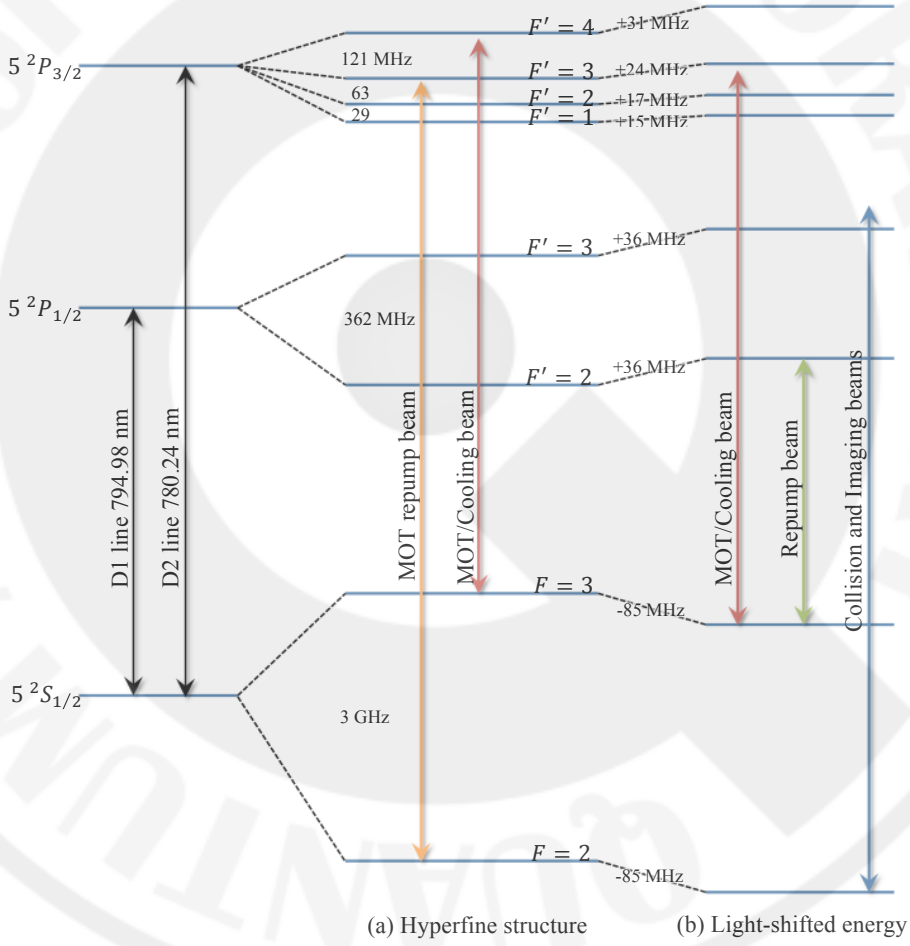

Figure 4.8. The energy level of ^{85}Rb D lines transitions without the light (a) and the energy level shifted due to the presence of the light (b). Laser beams employed in this work with the corresponding transitions are shown.

4.1.4 Imaging system and collision laser

For the fluorescence imaging, a standing wave of blue detuned light at 795 nm exposed the atoms trapped in the FORT. The light beam called imaging beam was linearly polarized and blue detuned by 15 MHz from the D1 $F = 2$ to $F' = 3$ transition as seen in Figure 4.8. By using the imaging beam, the fluorescence of the atoms in the $F = 2$ ground state was induced and was corrected with the high NA lens. For the atoms in the $F = 3$ ground state, they were optically pumped into the $F = 2$ ground state by using a D1 repump beam which was red detuned by 20 MHz from the D1 $F = 3$ to $F' = 2$ transition.

During imaging, the Doppler heating might be occurred because of the blue detuned imaging beam that lead to the loss of the atoms from the dipole trap. However, the standing wave of the imaging beam also produced the Sisyphus cooling mechanism (see section 2.1.5 in Chapter 2) to compensate with the heating. The Sisyphus cooling became dominant over the Doppler heating when the intensity of the imaging beam was high enough. Furthermore the six cooling beams used for loading MOT before were applied as well. These cooling beams provided the PGC mechanism (see section 2.1.4 in Chapter 2) operating on the D2 $F = 3$ to $F' = 4$ transition when the atoms were in the wings of the trap. At the bottom of the trap, the frequency of cooling beams closely corresponded with the D2 $F = 3$ to $F' = 3$ transition (about –4 MHz detuning). As a result, the cooling beams acted as the repump beam that optically pumped the atoms from the $F = 3$ ground state to the $F = 2$ ground state where they interacted with the imaging beam.

Toptica DL Pro ECDL was used to provide a light with wavelength of 795 nm operating on the D1 transitions. Figure 4.9 shows a photo of the D1 laser and the optical alignment for controlling and stabilizing its frequency. The output beam was split a few mW into a PSAS for locking the laser frequency to the $F = 2$ to $F' = 3$ D1 transition. An Isomet AOM (Part No.: 1206C) labeled AOM1, was use to shifted the laser frequency inside the PSAS by a half of the modulating frequency. The AOM1 was modulated by a home-built driver.

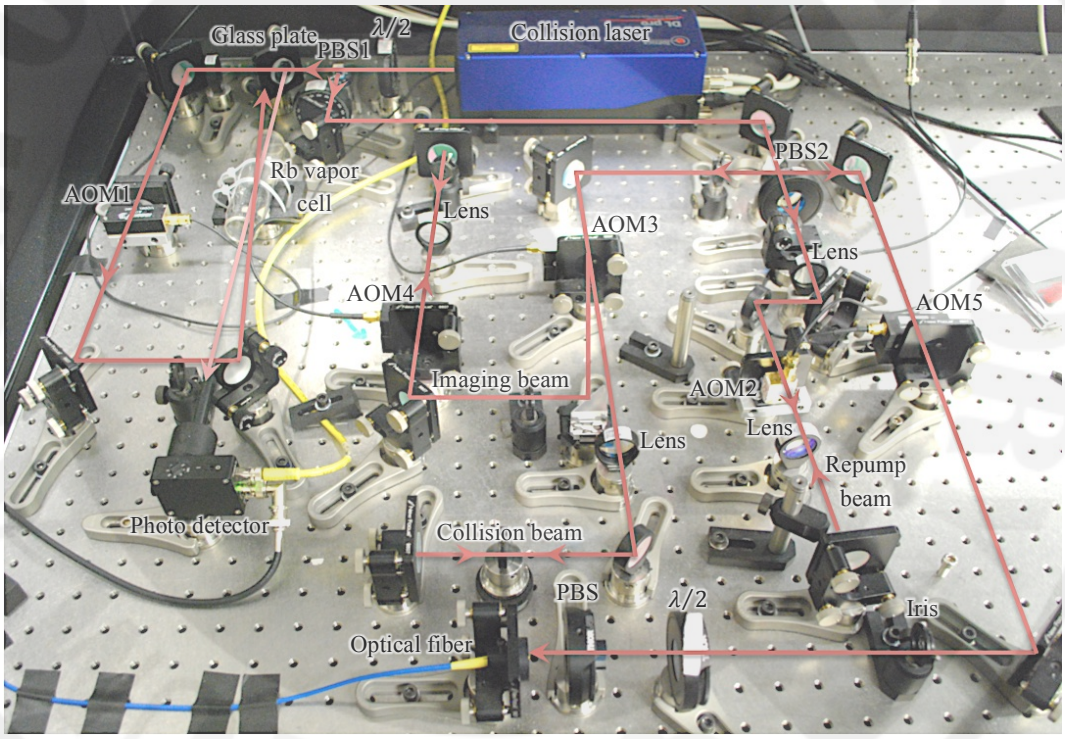

Figure 4.9. Photograph showing the optical alignment of locking and shifting the frequency for the D1 laser.

The remaining beam was split again by using a half-wave plate and a PBS2 into two beams. The first beam was the D1 repump beam was double passed through an AOM2 with a CF of 1.5 GHz from Brimrose (Part No.: GPF-1500-200-780) and

was allowed only the first minus order to be reflected back to the PBS2. Agilent Signal Generator (Part No.: N5183A). This AOM2 was modulated by using a Mini-Circuits Power Amplifier (Part No.: ZHL-5W-2G). From this configuration, the frequency of the repump beam was shifted down by 3.15 GHz that corresponded to the $F = 3$ to $F' = 2$ D1 transition. For the second beam, it was passed through an AOM3 made from Interaction (Part No.: ATM2251A2). An Interaction Model DE driver was operated to modulate the AOM3. After the beam passed through the AOM3, the first order beam diffracted by this AOM was reflected back to the PBS2. This beam called a collision beam was used for inducing collisions between trapping. The zero-order beam diffracted from the AOM3 was used as an imaging beam. The imaging beam was double passed an Interaction AOM4 (Part No.: ATM1501A) modulated by an Interaction Model DE driver. Then the imaging beam propagated back to the PBS2 as well. As all of the three beams were combined at the PBS2, they have the same direction and were passed through an AOM5, which acted as a fast shutter. The AOM5 was an Interaction AOM (Part No.: ATM1351A) and was modulated by an Interaction Model DE. The first diffracted order from the AOM5 was coupled into a single mode fiber. The detuning of the three beams were calculated as:

$$\delta_{ima} = \text{Lock frequency } (= 0 \text{ MHz}) + \tfrac{1}{2} \times \text{AOM1} + 2 \times \text{AOM4} - \text{AOM5},$$

$$\delta_{Rep} = \text{Lock frequency } (= +3.36 \text{ GHz}) + \tfrac{1}{2} \times \text{AOM1} + 2 \times \text{AOM2} - \text{AOM5},$$

$$\delta_{col} = \text{Lock frequency } (= 0 \text{ MHz}) + \tfrac{1}{2} \times \text{AOM1} + 2 \times \text{AOM3} - \text{AOM5}.$$

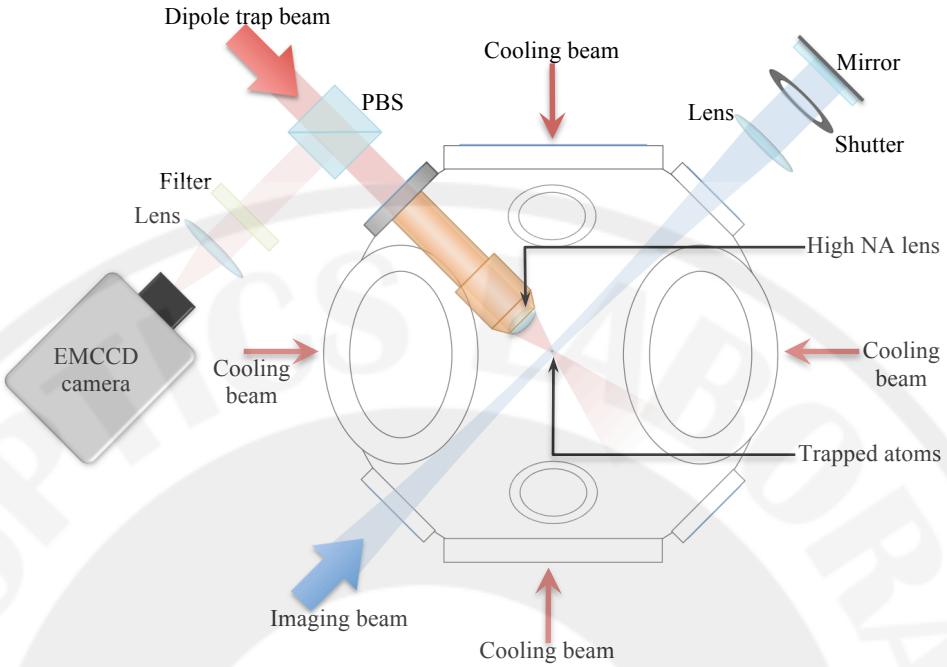

Figure 4.10. The schematic of the dipole trap and the imaging system.

After the three beams left from the fiber, they were steered into the science chamber by using many mirrors in such the way that their direction was overlapped the position of the dipole trap as illustrated in Figure 4.10. The beams were passed through a lens with the focal length of 500 mm before going into the chamber. After the beams left from the chamber, they were collimated by passing another lens and reflected off a mirror to go back into the science chamber for creating the standing wave. A mechanical shutter was installed in front of the mirror and turned the shutter on when the collision beam was employed. In the imaging stage, the imaging beam, the repump beam and the cooling beam with the power of 40 μW, 15 μW and 0.6 mW respectively were applied. After the trapped atoms absorbed the photons and spontaneously emitted them, the high NA lens collected only about 10% of the fluorescence. The collected fluorescent light was passed a PBS. Approximately half of the light was reflected into another direction for separating them from the dipole

beam as seen in the figure. The reflected light propagated through an 830 nm notch filter from Semrock (Part No.: NF0183OU) for removing the scattered light of the 828-nm dipole beam. Then the light propagated through a 795 nm bandpass filter (Part No.: FF01-800/12) for filtering other stray light. The output of the two filters, which was about 37% of the collected light, was focused onto an 8.2×8.2 mm image sensor of an electron-multiplying charge coupled device (EMCCD) camera from Princeton Instruments (ProEM: 512B) to record the 250×30 pixels images. A measured quantum efficiency of the EMCCD was 60%. The EMCCD was cooled to –70 °C by using a thermo-electric device for reducing a dark current. The avalanche e gain, which is an electron-multiplying gain of the EMCCD, was set at 100.

4.2 Trapped atoms detection

In this section, the techniques for preparing and counting a small number of atoms in FORT are explained (Sec. 4.2.1). These techniques were used to prepare and identify single and two atoms for the collisional study. The trapping lifetime and the temperature of the prepared single atoms were observed (Sec. 4.2.2). Finally, the method to determine an atom number for large samples in the trap was introduced (Sec. 4.2.3).

4.2.1 Preparation and counting small numbers of atoms

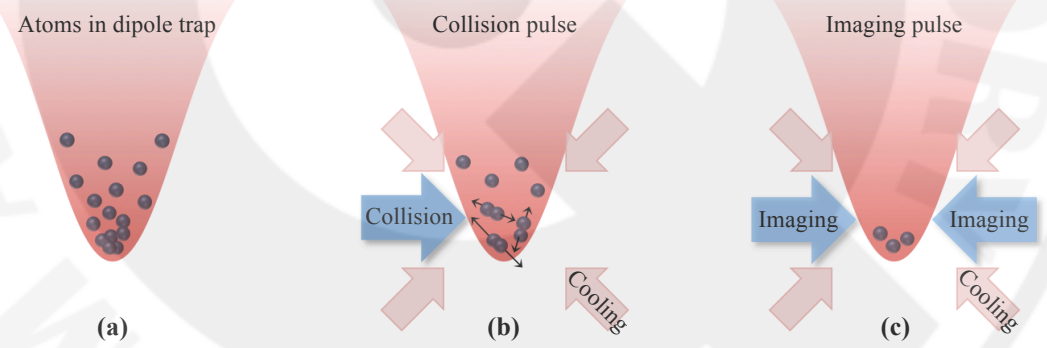

Figure 4.11. Preparation of small number of atoms by using the light-assisted collisions. The cold atoms are loaded into FORT (a); most of them are ejected out of the trap by the collision light pulse (b); and the remaining atoms are counted by using the imaging light pulse (c).

As the purpose of this thesis is to study the cold collisions between only two atoms, a method to prepare small numbers of atoms in FORT is needed. In this section, the

preparation method using the light-assisted collision is introduced. The method is separated into three steps as illustrated in Figure 4.11. In the first step (Figure 4.11 (a)), by using the series of cooling and trapping techniques mentioned before in Sec. 4.1.2, the average of 10 to 200 ^{85}Rb atoms were loaded into the dipole trap. The number of loaded atoms depended on both the loading times of MOT and cMOT. For the second step (Figure 4.11 (b)), the collision light pulse was applied for inducing the collisions between them where the light pulse consisted of the collision beam and the six cooling beams (the MOT cooling beams). As described before in Sec. 4.1.4, the cooling beams produce the PGC cooling mechanism to reduce the excess energy of the atoms generated from the collisional process. The cooling beams also act as the efficient repump beam that optically pump the atoms into the $F = 2$ ground state where they interact with the collision beam. As a result, the majority of the atoms were ejected until only few atoms were left in the trap.

For the last step (Figure 4.11 (c)), the imaging stage was employed. The imaging light pulse exposes the remaining atoms for 10 ms. The light pulse consisted of the standing wave of the imaging beam, the D1 line repump beam and the six cooling beams as detailed in Sec. 4.1.4. The imaging beam was blue detuned by 20 MHz from the $F = 2$ to $F' = 3$ D1 transition and had the beam power of 50 mW. Due to the standing wave of the imaging beam, the Sisyphus cooling was formed. The cooperating of the PGC and Sisyphus cooling provided the longer trapping lifetime of the atoms during the imaging stage. The fluorescence of the atoms induced by the imaging light was collected and focused into the EMCCD. The samples of the atomic fluorescence images are shown in Figure 4.12 (a). The images of the atoms were cropped into 11×11 pixels frame.

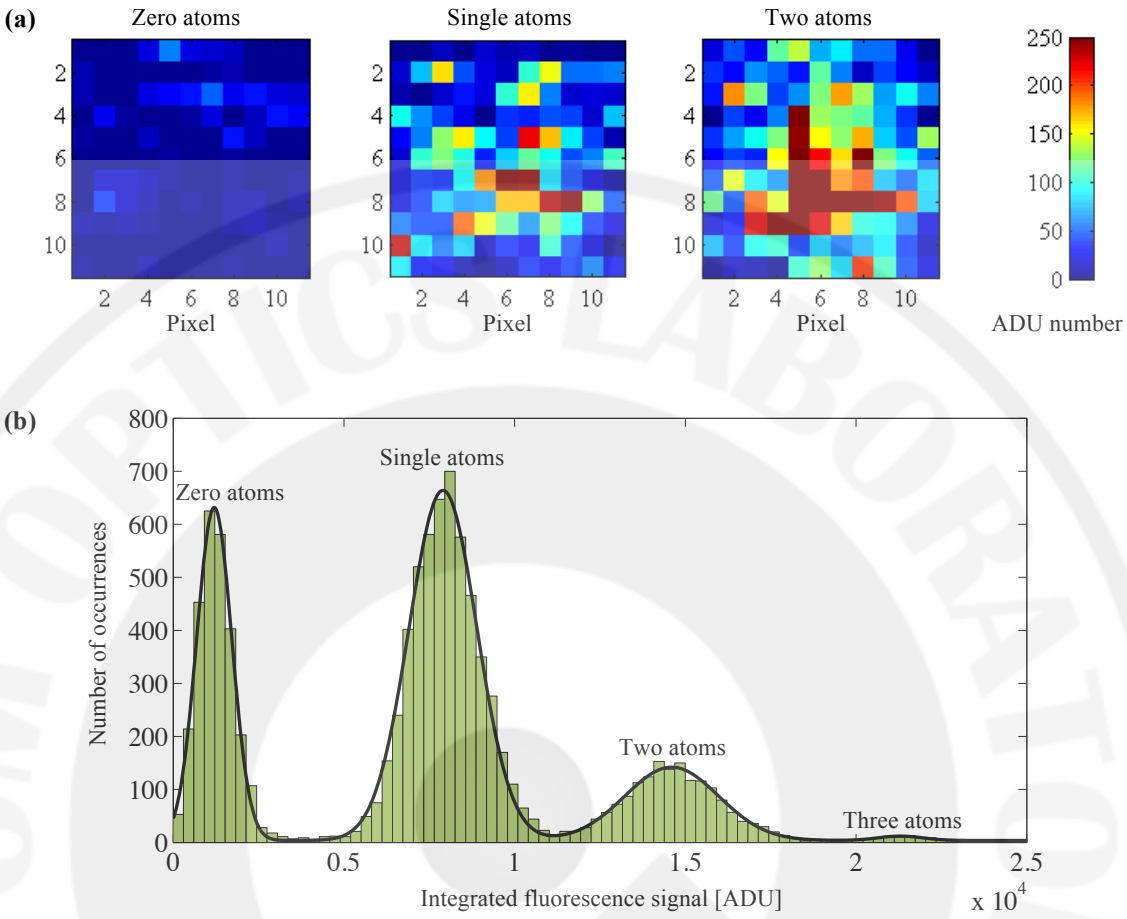

Figure 4.12. Experimental images of zero, one and two atoms are shown in (a). The color of each pixel is indicated an analog-to-digital unit (ADU) number of the atomic fluorescence as presented in the color bar. Histogram of the integrated fluorescence of each image for 10,000 experimental runs is plotted in (b). The peaks from the left hand represent zero, one, two and three atoms remaining in the FORT. The solid line indicates a fitting with the four Gaussians.

The atomic fluorescence signals gained from the images were used to determine the numbers of atoms. An ADU number of each pixel in the image represented the level of the collected light intensity. Then a sum of the ADU numbers for the entire frame was done for getting an integrated fluorescence signal. For this

method, only one experimental run cannot determine the atom number. Consequently, the all of these three steps was repeated several times (above 100 times in this research). The histogram of the integrated fluorescence signals was plotted as shown in Figure 4.12 (b). The result shows that the appeared peaks are separated equally from the adjacent ones. That is because the atomic fluorescence was discrete in correspondence with the number of atoms in the trap. The peaks from the left hand represent the fluorescent signal from zero, one, two and three atoms remaining in the FORT respectively. The fluorescent signal for zero atoms is not equal to zero ADU due to the noise created from the EMCCD readout and the stray light. The photons emitting from the atoms follow a Poissonian photon statistic that contributes to the peak widths. However, by using this imaging technique, it is hard to resolve the peak of the high atom number due to the atomic lost during the imaging stage. The technique to determine the high number of atom will be presented later in Sec. 4.2.3.

In order to prepare either single or two atoms, the duration of the collision pulse in the second step was optimized. The imaging technique in the third step provided the capability to distinguish the number of atoms in each run. After the experiment was done for several runs, each run that either single or two atoms were loaded, was chosen to be accounted. In this work, the efficiencies of the preparations were about 0.40-0.90 for single atom and about 0.2-0.3 for the two atoms that depended on the parameters of the collision light pulse.

4.2.2 Lifetime and temperature measurement

After the single atoms and the pairs of atoms were prepared in the FORT, the trapping lifetime and the temperature of the atoms were measured. In this study, the lifetimes of single atoms were measured under the influence of light. Figure 4.14 shows the measurement of the trapping lifetime of the single atoms while the collision pulse was being applied.

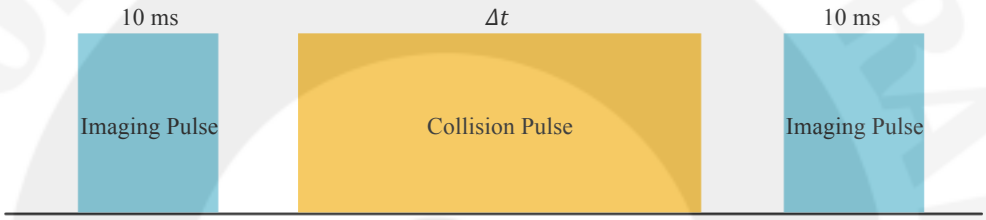

Figure 4.13. Schematic of the trapping-lifetime measurement.

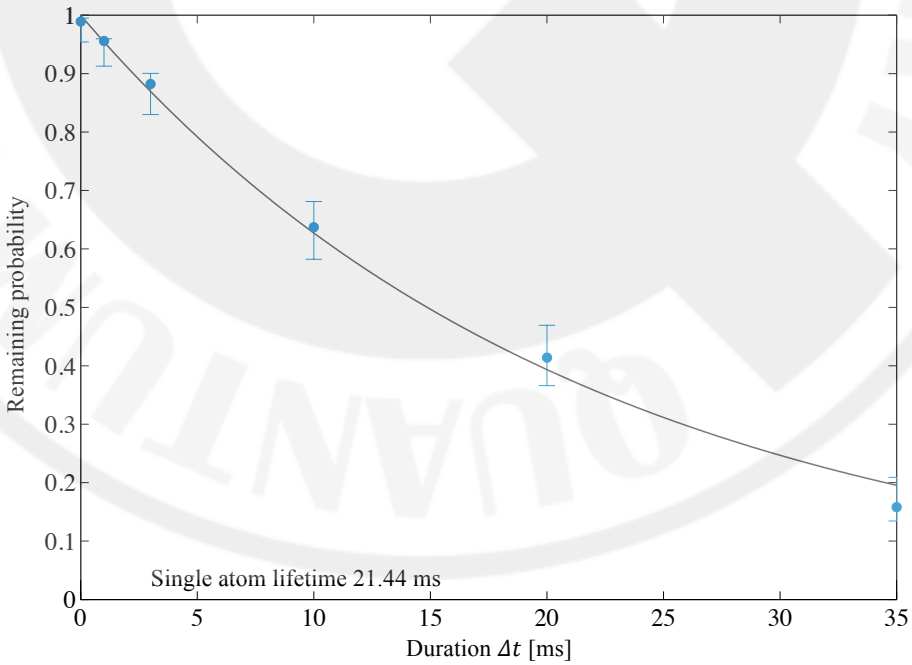

Figure 4.14. Remaining probability of single atom P_R plotted as a function of the duration Δt. The fitting provided the trapping lifetime of single atoms.

The lifetime measurement began with identifying the existence of single atoms by the imaging stage (which is the third step of preparing small number of atom in Figure 4.11 (c)). At this stage, the imaging pulse was applied for 10 ms as represented by the first blue pulse in Figure 4.13. Then the collision light pulse (the second pulse in the figure) was applied for the duration of Δt, where the pulse consisted of the collision beam with the power of 11 mW and the detuning of 85 MHz from $F = 2$ to $F' = 3$ D1 line transition and the six cooling beams. During this duration, the atoms may be lost due to the radiative force of the light. Finally, the atom number left in the trap that could be either zero or one atom was measure by the second imaging stage. The experiment run was repeated for 200 times. Only the runs, which observed single atom in the first imaging state, were accounted. Then the probability of single atom remaining in the trap after applying the collision pulse is defined by

$$P_{Rem} = \frac{N(1)_2}{N(1)_1}, \tag{4.3}$$

where $N(1)_i$ is the number of the experimental runs that found single atoms in the i^{th} imaging stage.

The remaining probability P_{Rem} getting from 200 experimental runs was plotted versus the pulse duration of Δt as shown in Figure 4.14. The blue circles indicate the observed P_{Rem} and the solid line is fitting curve calculated from the exponential decay function. The fitting function is:

$$P_{Rem} = \exp\left(-\frac{\Delta t}{\tau}\right), \tag{4.4}$$

where τ is the trapping lifetime of single atom. From the fitting, the trapping lifetime of single atoms under the influence of the blue detuned collision pulse is equal to 21.44 ms.

For the temperature measurement, a release and recapture method was used [49]. After the single atom was loaded into the FORT, the first imaging pulse was applied to identify the existence of single atom as represented by the first blue pulse in Figure 4.15. The FORT represented by the red pulse in the figure was turned off for the duration of Δt. With out the trapping beam, the atom was released to fly out off the trap with an initial velocity and also be force to drop down due to the gravity. At the end of the duration Δt, the trap was turned on again. The atom might be recaptured as the potential well was appeared. The number of atom in the FORT was measure at the end of process by the second imaging stage, which is represented by the second imaging pulse in the figure. As it was only one atom before tuning off the trap, the number measured by the second imaging could be either zero or one atom. The experimental run was repeated for 200 times. In the consequence, the probability that the single atoms were recaptured when the FORT was turned on is defined by

$$P_{Rec} = \frac{N(1)_2}{N(1)_1}, \tag{4.5}$$

To find out the temperature, the measured P_{Rec} was plotted versus the releasing duration of Δt as represented by the blue circle in Figure 4.16. The solid line represents the fitting data obtained from the Monte Carlo simulation. The fitting provided the estimated temperature of 204 ± 5 μK.

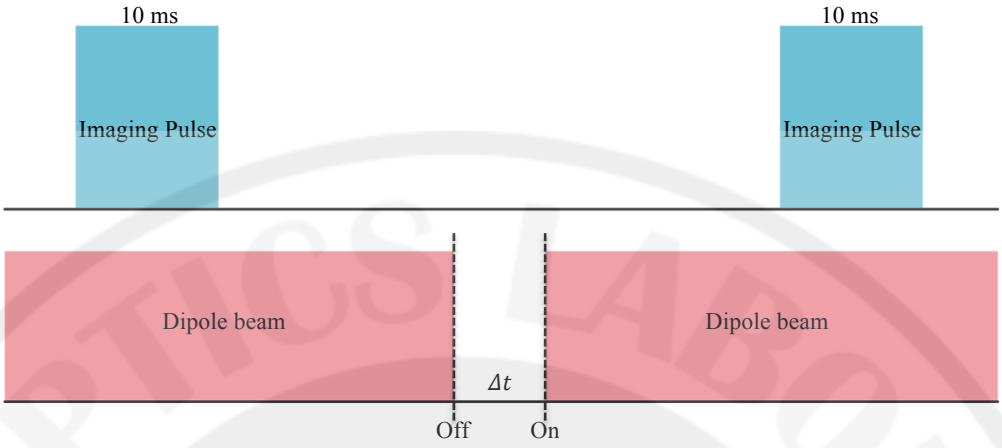

Figure 4.15. Schematic of temperature measurement by using the released and recaptured method.

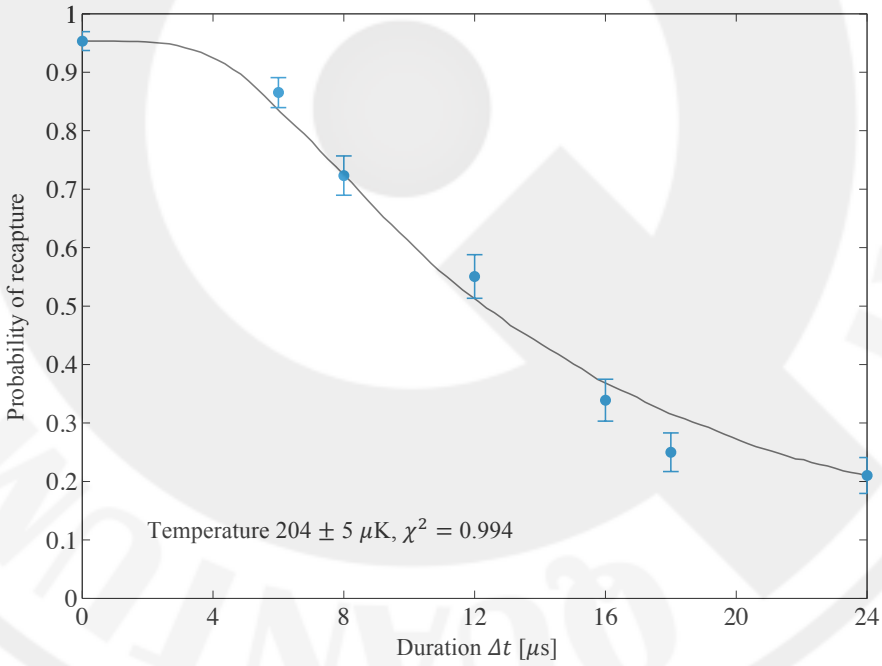

Figure 4.16. The Probability of recapture P_{Rec} is plotted against the releasing duration of Δt. The fitting line obtains from a Monte Carlo simulation explained in text to extract the temperature of 204±5 μK.

In the simulation, an ^{85}Rb atom at trial temperature T was generated. The Maxwell-Boltzmann statistics was used for determining the initial velocity of the atom. Each one-dimensional velocity was chosen randomly from the normal distribution,

$$f_v(v_i) = \frac{1}{\sigma\sqrt{2\pi}} \exp\left(-\frac{v_i^2}{2\sigma}\right), \tag{4.6}$$

where $\sigma = \sqrt{\frac{k_B T}{m}}$. The trapping potential was estimated as the harmonic one. That is

$$U(x, y, z) = -U_0 + \frac{1}{2} m[\omega_{rad}^2(x^2 + y^2) + \omega_{ax}^2 z^2], \tag{4.7}$$

where U_0 is a depth of the dipole trap, ω_{rad} and ω_{ax} are the natural oscillation of the atom in the harmonic trap in the radial and axial directions respectively. The initial position of the atom in the radial and axial directions were chosen randomly from the normal distribution where $\sigma_{rad} = \sqrt{\frac{k_B T}{m\omega_{rad}^2}}$ and $\sigma_{ax} = \sqrt{\frac{k_B T}{m\omega_{ax}^2}}$ respectively. The starting time of the simulation was set as the time when the trap was turned off. Then the position and velocity of the atom evolved dynamically in time under the influence of the gravity force. Each time steps of simulation, the possibility that the atom was recaptured when the trap was suddenly turned on, was observed. The atom was considered to be lost if its kinetic energy of was higher than the depth of the trapping potential at that position. The simulation was continued until the time was equal to the longest experimental duration. These processes were repeated for 5,000 single atoms to get the average value of P_{Rec} as a function of the duration. The temperature

T was varied until the simulating P_{Rec} curve fit well with the experimental data. The programming of the simulation is shown in Appendix B.

The temperature of the atomic pairs in the trap was also measured by using the same method. Figure 4.17 shows the experimental result and the fitting solid line that determine the temperature of 281 $\pm$ 14 μK. The temperatures of the single atoms and the pairs were used for determining in the study of the cold collision, which is detailed in the next chapter.

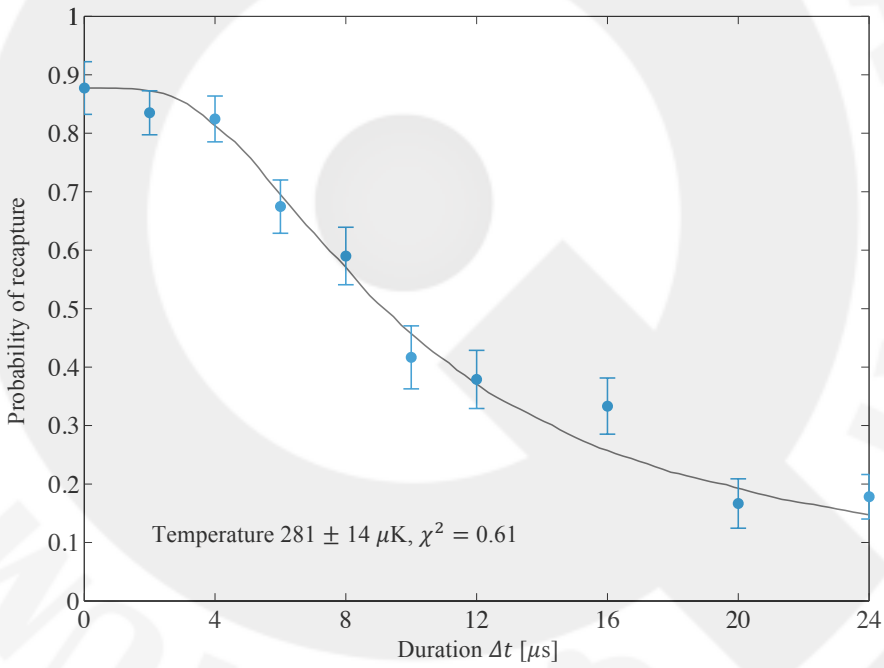

Figure 4.17. The result of temperature measurement for the atomic pair in the dipole trap. The Probability of recapture is plotted against the release duration. The fitting line obtained from a Monte Carlo simulation extract the temperature of 281$\pm$14 μK from the release and recapture data.

4.2.3 Determining the atom number in the trap

To determine the number of atoms in the trap, it was necessary to account the effect of atomic collisions induced while the imaging pulse exposed the atoms. The losing rate of the atoms due to the collisions increased relatively with the atomic number in the trap as represented in the equation (2.16) in Chapter 2. During imaging state, the changing rate of the atom number in the dipole trap can be calculated by

$$\frac{\mathrm{d}N}{\mathrm{d}t} = -\gamma N - \beta N(N-1). \tag{4.8}$$

Here the atomic loading rate of the dipole trap is zero and the rate of atomic loss due to the light induced two-body collisions is proportional to $N(N-1)$, where N is the number of atom [50]. The equation **(4.8)** is transformed into $\mathrm{d}N\left(\frac{1}{N}+\frac{1}{\alpha-N}\right) = A\mathrm{d}t$, where $A = \beta - \gamma$ and $\alpha = A/\beta$. Integrating both side of the equation gives us the result of

$$N = \frac{\alpha}{\frac{1}{B}e^{-At}+1}, \tag{4.9}$$

where B is a constant getting from the integration. In case of $t = 0$, the number of atom is equal to N_0. Substituting this in equation **(4.9)** gives us $B = \frac{N_0}{\alpha - N_0}$ and the equation is changed into:

$$N(t) = \left[\frac{\beta}{A} + \left(\frac{1}{N_0} - \frac{\beta}{A}\right)e^{-At}\right]^{-1}. \tag{4.10}$$

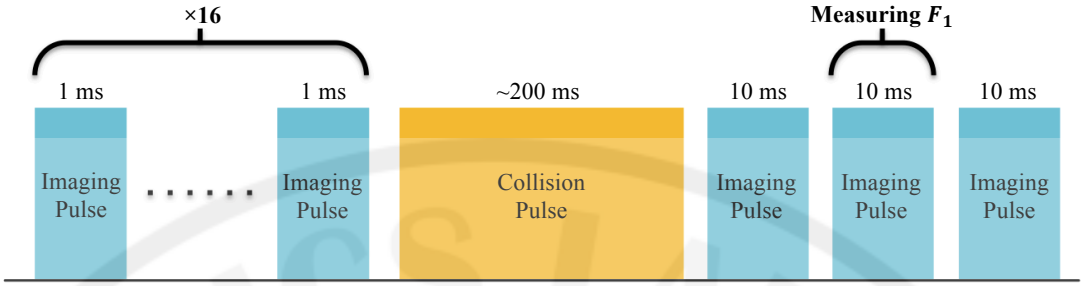

Figure 4.18. Schematic of the atom number measurement.

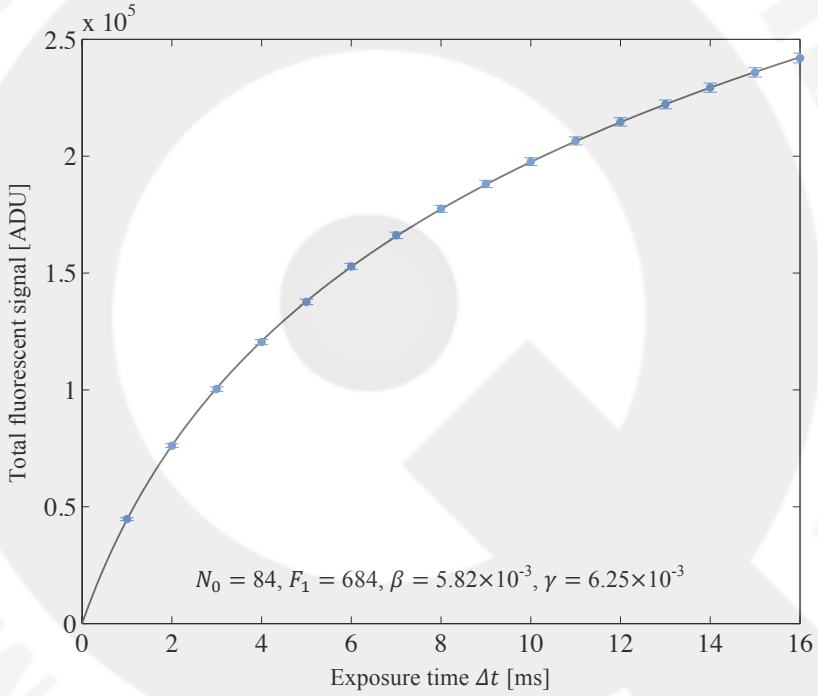

Figure 4.19. Total fluorescent signal of the remaining ^{85}Rb atoms in the dipole trap versus the exposure time of imaging pulse.

For determining the number of atoms in the trap, the total fluorescence signal of the trapped atoms was observed as a function of the exposure time of imaging pulse Δt. The total fluorescence can be calculated by $\int_o^{\Delta t} F_1 N(t) \mathrm{d}t$, where F_1 is the

average of measured fluorescent rate of single atoms. As a consequence, the total fluorescence is determined by

$$F_{tot}(\Delta t) = F_1\left[\frac{A\Delta t}{\beta} + \frac{1}{\beta} ln\left(\frac{\beta N_0}{A} + \left(1 - \frac{\beta N_0}{A}\right) e^{-A\Delta t}\right)\right]. \quad (4.11)$$

In the experiment, after cold atoms were loaded into the FORT, the series of fluorescence images were recorded as shown by the 16 imaging pulses in Figure 4.18. For each image, the detector collected the atomic fluorescence for a duration of 1 ms. Then the collision light pulse was used to eject the atoms out off the trap until only single atom left. To measure F_1, three imaging stages with the duration of 10 ms were applied as shown in the figure. The experiment was repeated for 200 runs to obtain the average value. Only the fluorescence signals obtained from the second imaging stages of the experimental runs that single atoms were found in both the first and last imaging states, were counted for determining F_1.

The fluorescence signals obtained from the 1-ms imaging pulse were accumulated for getting the total fluorescence signal as a function of the exposure time of the imaging pulse as plotted in Figure 4.19. The result was fitted with the equation **(4.11)** as represented by the solid line. This fitting provided the initial number of atoms N_0 before shining the imaging light pulse. As the result, the initial number of atoms was equal to 84 and during apply the light pulse they were lost from the trap with the rates $\gamma = 6.25\times10^{-3}$ s^{-1} and $\beta = 5.82\times10^{-3}$ s^{-1}.

CHAPTER 5

STUDY OF COLD COLLISION

This chapter reports the result of a study about an inelastic collision between two cold ^{85}Rb atoms under an influence of a light field. The experiment began with preparing the cold atom via MOT and loading them into the optical dipole trap through cMOT and optical molasses as detailed before in the previous chapter. A collision light pulse was applied to kick out the atoms until only two atoms were left in the trap. Preparation of only two atoms in FORT allowed us to observe the two-bodies collisions that were induced by the light. Both cases of the red- and blue-detuned light were studied as presented below in Sec. 5.1 and Sec. 5.2 respectively.

5.1 Cold collision induced by red-detuned light

This section introduces a method to measure the time evolution of two atoms confined in the optical dipole trap (Sec. 5.1.1). This allowed us to detect the effect of the red-detuned light on the decay rate of two atoms and the growth rates of the probability of detecting one and zero atoms in the trap. As a result, the probability of single atom loss event in two-body collision, $P(1|2)$ was determined. Further more, the light was used to prepare a single atom in the trap as the purpose to enhance the single atom loading efficiency (Sec. 5.1.2).

5.1.1 Time evolution of two atoms

Firstly, the system consisting of only two atoms in the red detuned light field is considered. When the atoms move toward each other in the ground state $|S+S\rangle$ and pass through the Condon point R_c where the transition is resonant with the light field, they have a probability to absorb the photon and be excited into the attractive excited state $|S+P\rangle$. This process is the first step of the FCC and RE processes that may lead to the trap loss as described before in Chapter 2. Here, the RE, which has more probability to occur, is in the focus.

In order to study the effect of the parameters of red detuned light on the cold collision, the experiment began with loading two atoms into FORT by using the method mentioned in Chapter 4. A use of the imaging stage for 10 ms identified the existence of the two atoms in trap as illustrated in the first flame of Figure 5.1. In the second flame of the figure, the collision light pulse was applied for the duration of Δt to induce the collisions between the atoms. As a result of collisions, the atoms may be lost. Finally, the number of atoms was measured by the imaging stage as shown in the last flame of the figure. The duration of Δt was varied for exploring the time evolution of the pair. For each Δt, the experiment was repeated for 600 runs that provided about 180 pairs of atoms measured in the first imaging stage. Only the runs that found a pair of atoms in the first imaging were counted. For each of the runs, the observed atom number in the last imaging stage could be two, one or zero as the result of none-atom, single-atom or pair lost respectively. The probabilities to found two, one and zero atoms remaining in the trap were plotted as a function of Δt to show the time evolution of two atoms as the result of the light-assisted collisions between them.

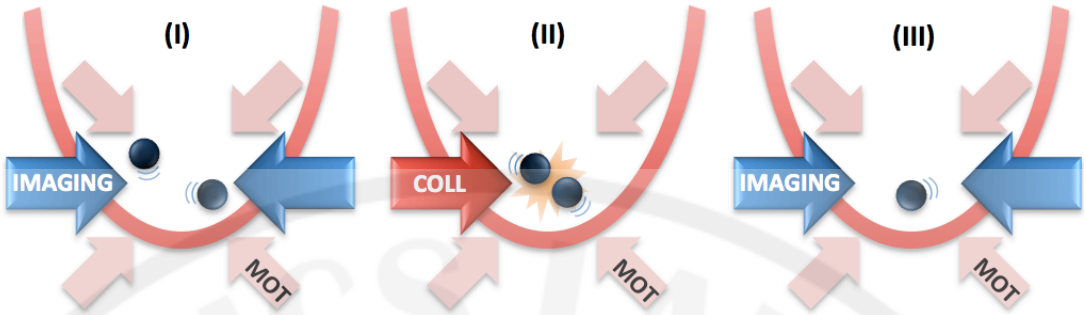

Figure 5.1 shows a sequence of the time evolution measurement of a pair of atoms in the FORT.

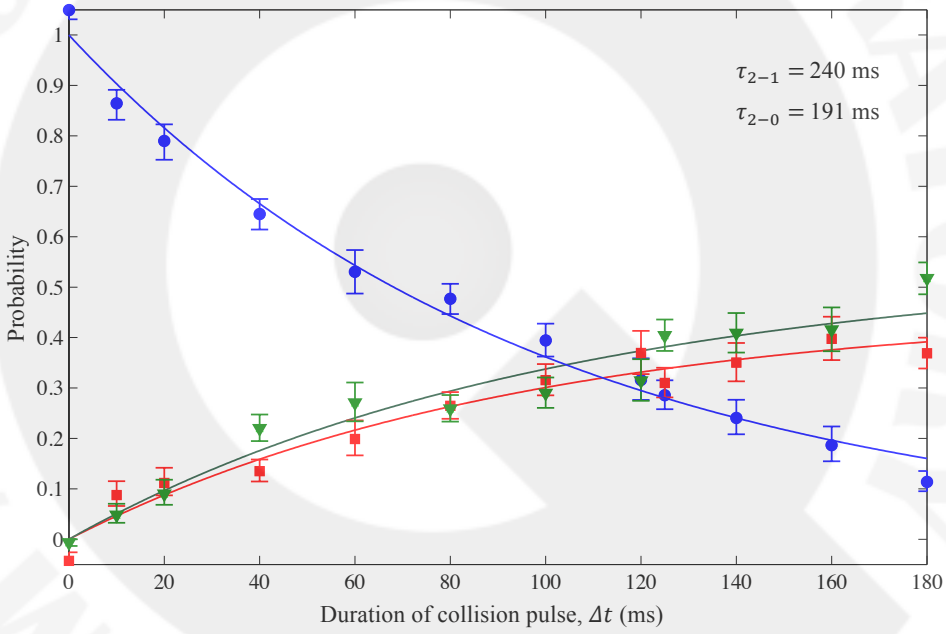

Figure 5.2. Probability to observe two, one and zero atoms in FORT under the influence of collision light pulse plotted as function of the pulse duration Δt. The blue circles indicate the survival probability of the pair. The red squares and the green triangles indicate the probability of obtaining one and zero atoms respectively. The solid lines indicate the fitted curves of the data by using a simple decay model that give us $P(1|2) = 0.44$ for the parameters of collision light pulse which are $P_{col} =$ 350 nW, $\delta_{col} = -45$ MHz, $P_{rep} = 200\ \mu$W and $\delta_{rep} = -4.3$ MHz.

The atomic-pair evolution is shown in Figure 5.2. The blue circles indicate a survival probability of the pair after applied the collision light pulse for Δt. As seen in the figure, the probability was decay due to the atomic loss. At the same time, the probabilities to find one and zero atoms remaining in the trap were accumulated as represented by the red squares and green triangles respectively. In this case, the collision light pulse consisted of the collision beam and the cooling/repump beams. The collision beam had a power, P_{col} of 350 nW and its frequency was red detuned by 45 MHz from the D1 $F = 2$ to $F' = 3$ transition at the center of the trap (δ_{col} = -45 MHz). The cooling/repump beams had a power, P_{rep} of 200 μW and there frequency were red detuned by 4.3 MHz from the D2 $F = 3$ to $F' = 3$ transition at the center of the trap ($\delta_{rep} = -4.3$ MHz).

To extract the probability of single atom loss event in these two-body collisions, the result data in the figure are fitted with a simple decay model of the pair probability. Let assume that the pair in the trap can decay to either one or zero atoms with a rate of $\frac{1}{\tau_{2-1}}$ or $\frac{1}{\tau_{2-0}}$ respectively due to the collisions. Here, τ_{2-1} and τ_{2-0} are the lifetime of the pair due to the single atom and pair collisional loss respectively. Moreover, the pair also decays because of the finite trapping lifetime of atoms, τ. Then the rate equations for the probability of the pair P_2 and the probability of single atom P_1 can be written as

$$\frac{\mathrm{d}P_2}{\mathrm{d}t} = -P_2\left(\frac{1}{\tau_2} + \frac{2}{\tau}\right), \tag{5.1}$$

$$\frac{\mathrm{d}P_1}{\mathrm{d}t} = P_2\left(\frac{1}{\tau_{2-1}} + \frac{2}{\tau}\right) - \frac{P_1}{\tau}. \tag{5.2}$$

where $\frac{1}{\tau_2} = \frac{1}{\tau_{2-1}} + \frac{1}{\tau_{2-0}}$. The solutions of the rate equations give us the probabilities of the pair, one and zero atoms as a function of time, which are

$$P_2(t) = P_2(0)\exp\left(-t\left(\frac{1}{\tau_2} + \frac{2}{\tau}\right)\right), \tag{5.3}$$

$$P_1(t) = P_2(0)\left(\frac{1}{\tau_{2-1}} + \frac{2}{\tau}\right)\left(\frac{\tau\tau_2}{\tau + \tau_2}\right)\left\{1 - \exp\left(-t\left(\frac{1}{\tau} + \frac{1}{\tau_2}\right)\right)\right\}\exp\left(-\frac{t}{\tau}\right), \tag{5.4}$$

$$P_0(t) = 1 - \left(P_2(t) + P_1(t)\right). \tag{5.5}$$

The solid lines in Figure 5.2 indicate the fitting curve of the observed data with the equations (**5.3**) - (**5.5**). The values of τ_{2-1} and τ_{2-0} are extracted as the fitting parameters. The probability of single atom loss event from the collisions, $P(1|2)$ is defined by

$$P(1|2) = \frac{\tau_2}{\tau_{2-1}}. \tag{5.6}$$

From the fitting, τ_{2-1} and τ_{2-0} are equal to 240 ms and 191 ms respectively where the measured τ in this case is equal to 6.5 s. In this case, the calculated $P(1|2)$ is 0.44. The non-zero value of $P(1|2)$ represents the probability that the red detuned light induced collisions can contribute single atom lost from the two-body collisions as well.

However, as the portion of the collision light pulse was the cooling beams, the effect of the beams needed to be investigated. Consequently, the pair evolution under the influence of the cooling beams was observed. The collision light pulse used in the second flame of Figure 5.1 consisted of only the cooling beams with $P_{rep} = 0.64$ mW and $\delta_{rep} = -4.3$ MHz. The result is shown in Figure 5.3. From fitting the observed

data, τ_{2-1} and τ_{2-0} are equal to 130 s and 5.2 s respectively. The obtained $P(1|2)$ was then only 0.04. This represents that most of the collisional losses induced by the cooling beams were the pair loss. The reason was that even though the beams were little red detuned from the D2 $F = 3$ to $F' = 3$ transition but they were red detuned by ~3 GHz from the D2 $F = 2$ to $F' = 1, 2, 3$ transitions as well. In consequence, the atoms in the ground state with $F = 3$ were optically pumped into the other ground state efficiently by the near resonance beams. It was reasonable to assume that all collisions occurred while the atoms were being in the $F = 2$ ground state and they experienced the beams with the detuning of –3 GHz. Thus the collisions contributed only the pair loss as the result of the large detuning.

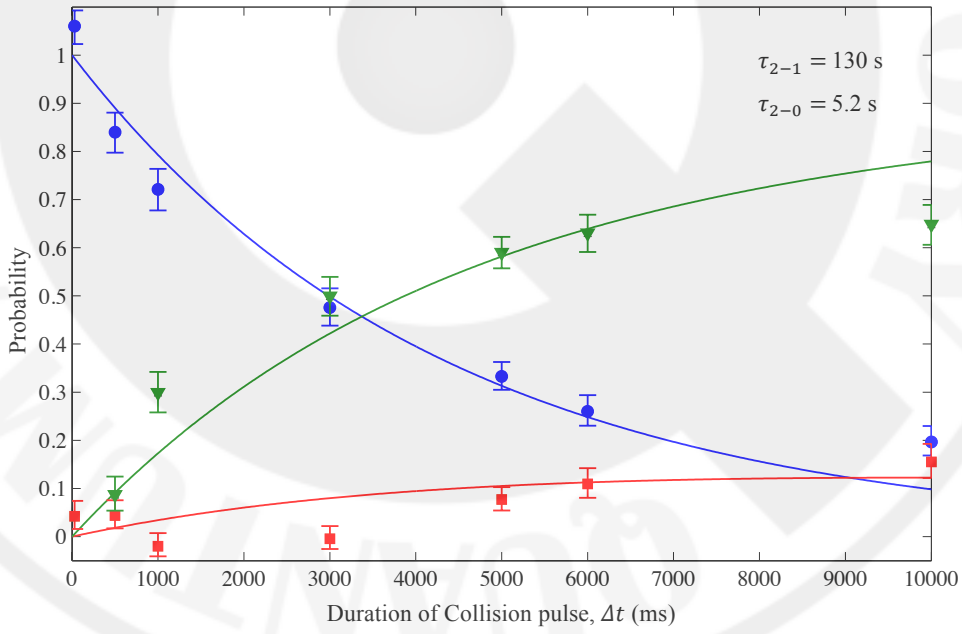

Figure 5.3. Probability to observe two, one and zero atoms in FORT under the influent of the cooling/repump light pulse plotted as function of the duration of the pulse. From fitting, $P(1|2)$ is determined to be 0.04.

In the case of that the collision light pulse consisted of both collision beam and cooling beams, the results were assumed that only the collision beam contributed the atomic loss. That is because the measured collisional pair decay time τ_2 induced by the cooling beams was very long (more than 5 s) compared with τ_2 induced by the collision beam (~100 ms). This assumption was used in considering the result in this entire study.

Simulation of the red detuned light induced collision

To understand the red detuned light assisted collision between two cold atoms, the dynamic of two atoms undergoing the collisions are simulated. The model of this simulation is relied on semiclassical GP and JV models detailed in Chapter 2. In the model, the three steps of the collision process are described by using the quasimolecular state picture. Step I, two atoms in the ground state $|S+S\rangle$ approach to each other. At the Condon point ($R = R_c$), the atoms may absorb a photon and transition into the excited state $|S+P\rangle$. Step II, in this $|S+P\rangle$, the atoms are accelerated toward each other as the result of the attractive excited-state energy, $U_e(R)$. Step III, the atoms decay to $|S+S\rangle$ by spontaneously emitting photon at the separation of R_s and gain a released energy E_r, which was equal to $U_e(R_c) - U_e(R_s)$. The atoms share the obtained E_r depending on their initial momentums before colliding. The atoms, of which the kinetic energy is higher than the trap deep potential, will escape from the trap.

To simulate the collision process, I begin with modeling of two atoms in the optical dipole potential. Their spatial and velocity distributions are followed the

Maxwell-Bozeman statistics. As a consequence, the initial positions of both atoms are randomly selected from the Maxwell-Bozeman distribution, of which a corresponding probability depends on the trapping potential $U(x, y, z)$ and an initial temperature T of the atoms. The initial velocities are chosen randomly from the Gaussian or normal distribution where the standard deviation $\sigma = \sqrt{k_B T/m}$ and m is mass of the atoms.

The simulated atoms move under the confining force of the trap and are cooled by the Doppler cooling model. To make the atoms experience the same cooling as in the experiment, the cooling rate of the experiment was measured through the atomic temperature as a function of cooling time. To do that, single atom was prepared in the trap where the temperature of the atom was 204 μK as reported before in Chapter 4. Then the atom was heated up to above 500 μK by turning off the dipole trap for 8 μs and shining the blue detuned MOT cooling and repump beams at the same time. After the trap was turned on, the atom recaptured was hotter than before. With this heating method, the temperature of atom was achieved the highest temperature of 967 μK as shown in Figure 5.4. After the heating process, the collision light pulse was shined to the heated atom for the duration of Δt. Then the temperature was measured. The parameters of the pulse were $P_{col} = 350$ nW, $\delta_{col} = -45$ MHz, $P_{rep} = 350\ \mu$W and $\delta_{rep} = -4.3$ MHz. As a result shown in Figure 5.5, the measured temperature (the blue circles in the figure) is plotted as a function of cooling time Δt. Finally, the Doppler cooling model in the simulation was created in such the way that the simulation result reproduced the observed time evolution as shown by the solid line in the figure.

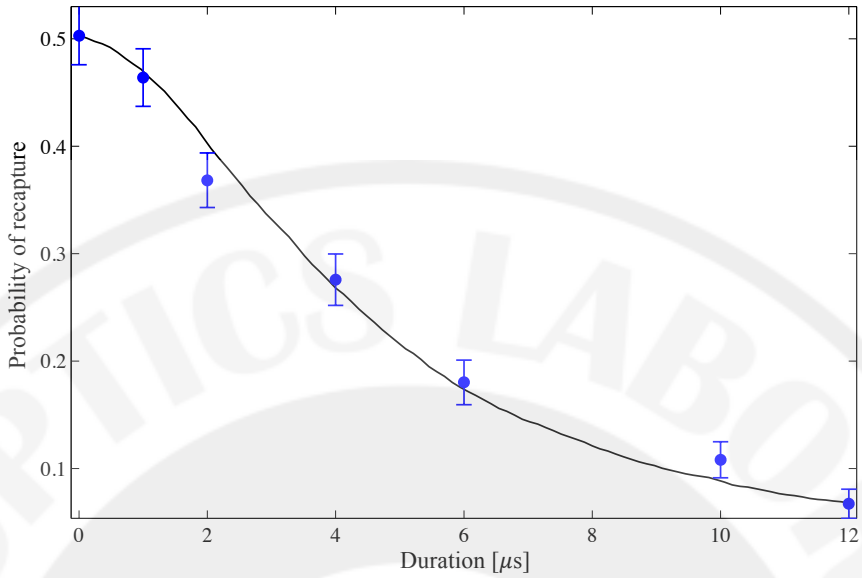

Figure 5.4 Probability to recapture single atom plotted as a function of the releasing duration for the temperature measurement. The solid line is a fit of the experimental data giving the temperature of 967±23 μK.

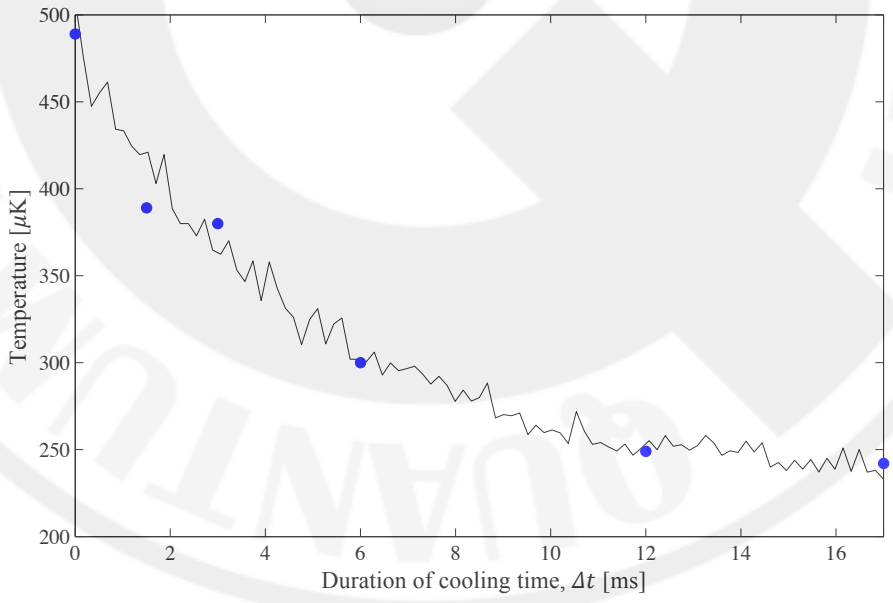

Figure 5.5. Temperature of single atom plotted as a function of cooling time of Δt. The blue circles show the measured temperature and the solid line is from the simulation.

While the two simulated atoms are travelling in the trapping potential and being cooled by the Doppler cooling model, they may move toward each other and get excited by absorbing photon in the collision beam at R_c. The excitation probability is determined by the Landau-Zener (LZ) formalism in dressed state picture shown in Figure 5.6 (a). As detailed before in Chapter 2, the attractive excited-state potential for the long-rang internuclear separation R is approximated to be $U_e(R) = \frac{C_3}{R^3} + \hbar\omega_0$, where $C_3 = -20.13$ a.u. [51]. The ground state is assumed to be independent of R. For the dressed-state picture, the energy level of the excited state is offset by the photon energy. It is then seem that it crosses with the energy level of the ground state at R_c as shown by the dotted line in the figure but it really does not (see Chapter 2) as represented by the solid line.

The two atoms, which are approaching each other, have a probability of P_{LZ} in equation (2.24) to undergo the LZ transition to the other dressed state when they are passing R_c (as the dotted line path). The atoms can move adiabatically through this region as well with the probability of P_A in equation (2.25) and end on the excited state potential as represented with the green arrow. If approaching atoms pass though the region by the LZ transition path, they will reach R_c again when they move away form each other (see the orange arrow). In this case, they may move adiabatically follow the upper dressed state. The atoms will be attracted to move approach each other and return back to R_c again. At this point, the atoms may undergo the LZ transition to the other dressed state and end on the excited state potential. If not, this scenario will repeat itself. From these processes, the probability that the atoms are in the excited state at the end, can be written as:

$$P_e = P_A + \frac{P_{LZ}^2 P_A}{1 - P_A^2}. \tag{5.7}$$

This P_e is used as the excitation probability of the approaching simulated atoms at R_c that is the step I of the collisional model.

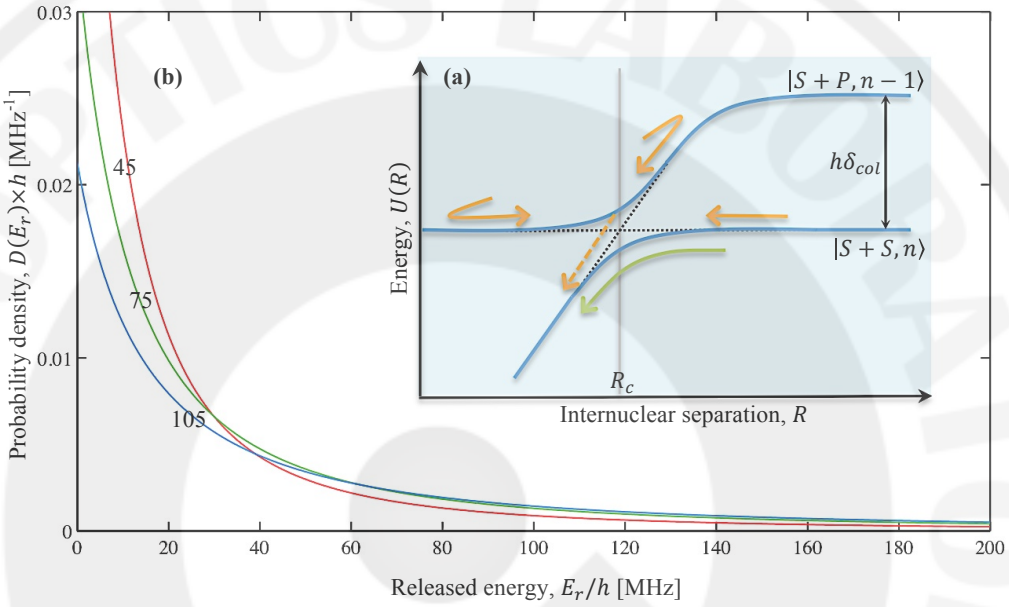

Figure 5.6. (a) Dressed state picture showing an avoided crossing between $|S+S, n\rangle$ and $|S+P, n-1\rangle$ at R_c. The color arrows show the different excitation paths. (b) Probability density of the released energy for $v(R_c) = 0.2$ ms^{-1} for three different values of δ_{col} (45, 75, and 105 MHz).

In the step II, the atoms are accelerated radially along the internuclear separation by $U_e(R)$. From equation (2.19), their radial velocity can be given by

$$v(R) = \sqrt{v(R_c)^2 - \frac{2}{\mu}[U_e'(R) - U_e'(R_c)]}, \tag{5.8}$$

where $U_e'(R)$ is $U_e(R)$ plus a centrifugal barrier. Due to the decay of the atoms in the excited state with the rate Γ_M, a survival probability of the atoms in the excited state traveling from R_c to R_s can be written as

$$S(R_s) = \exp\left(-\Gamma_M \int_{R_c}^{R_s} \sqrt{v(R_c)^2 - \frac{2}{\mu}[U_e'(R) - U_e'(R_c)]}\right). \tag{5.9}$$

As the separation where the atoms decayed is predicted from the above equation, the energy $E_r = U_e(R_c) - U(R_s)$ released in the step III of collision is determined. Figure 5.6 (b) shows examples of the probability densities of the released energy $D(E_r)$ for three values of δ_{col} which are -45, -75, and -105 MHz where $v(R_c) = 0.2$ m/s. As seen in the figure, the excited atoms had a high probability to release a small quantity of E_r during the collision. The predicted E_r is shared to both collision partners while the total momentum is conserved and the velocities of the atoms are changed along their internuclear separation $\boldsymbol{R}$. Then conditions for sharing E_r can be written as:

$$-\Delta\boldsymbol{v}_1 = \Delta\boldsymbol{v}_2 = -\alpha\boldsymbol{R}\,, \tag{5.10}$$

$$v_1^2 + v_2^2 + \frac{2E_r}{m} = v_1'^2 + v_2'^2. \tag{5.11}$$

Here $\boldsymbol{v}_1$ and $\boldsymbol{v}_2$ are the velocity of the first and the second atoms before collision respectively, $\boldsymbol{v}_1'$ and $\boldsymbol{v}_2'$ are the velocity of the first and second atoms after collision respectively, $\Delta\boldsymbol{v}_i = \boldsymbol{v}_i' - \boldsymbol{v}_i$ where i =1 or 2, the relative position vector $\boldsymbol{R} = \boldsymbol{R}_1 - \boldsymbol{R}_2$ where $\boldsymbol{R}_1$ and $\boldsymbol{R}_2$ are the position vectors of the first and second atoms respectively, and α is a positive constant. From the equations above, α could be determined by

$$\alpha = \frac{\boldsymbol{R}\cdot\boldsymbol{v} + \sqrt{\frac{4R^2E_r}{m} + (\boldsymbol{R}\cdot\boldsymbol{v})^2}}{2R^2}, \tag{5.12}$$

where the relative velocity $\boldsymbol{v} = \boldsymbol{v}_1 - \boldsymbol{v}_2$. After gaining the energy from the collision, the atom, of which kinetic energy is larger than the trap depth, is determined to be lost.

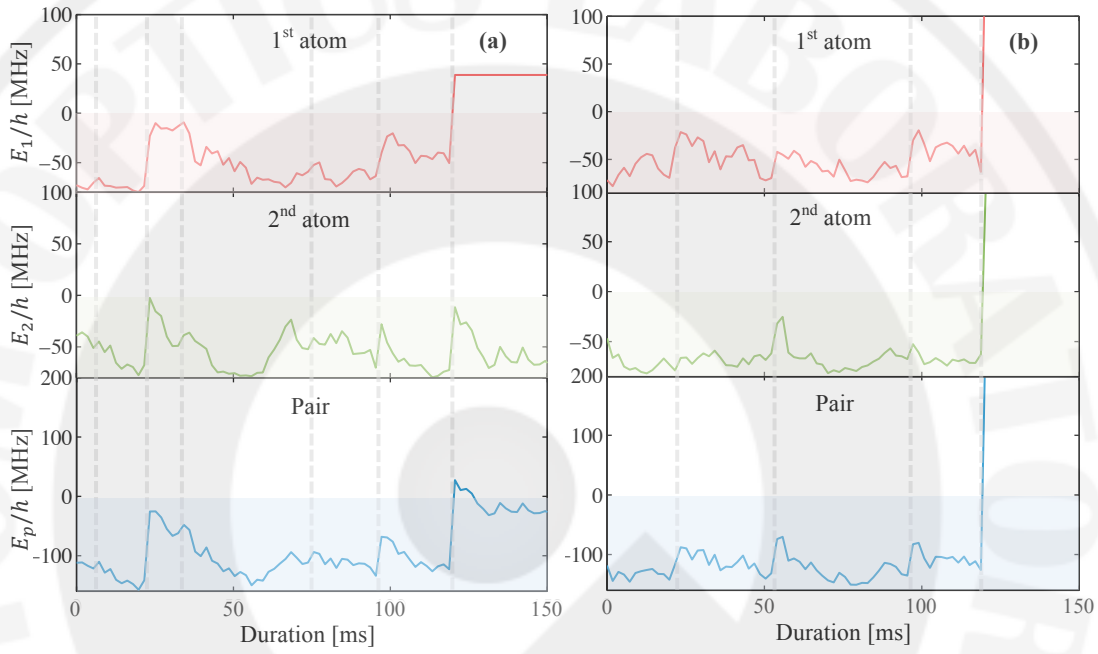

Figure 5.7 shows the total energies of the two simulated atoms and of the pair as a function of the collision duration. The simulation ends with single atoms loss (a) and other ends with the pair loss (b). The dashed lines show when the collisions happen.

As a result, both events of single- and two-atom loss can happen as represented in Figure 5.7 (a) and (b) respectively. The figure shows the total energies of individual simulated atoms, E_1 for the first atom and E_2 for the second atom, and their combining energy, $E_p = E_1 + E_2$, which evolve as a function of time. The gray dashed lines indicate when the inelastic collisions occur. In the simulation shown that most of the collisions release a low E_r, which is not high enough for making any

atoms lost. After collisions, an excess energy of the atoms tends to be decreased as the result of the Doppler cooling model. This scenario is repeated itself until the collision releases high energy, which is enough for making either one or two atoms lost. For a broad range of intermediate released energy, it is possible to lose only one of them due to the nonzero speed of the center of mass. For a large released energy, it has a high probability to lose both them. The programming of this simulation is in Appendix B.

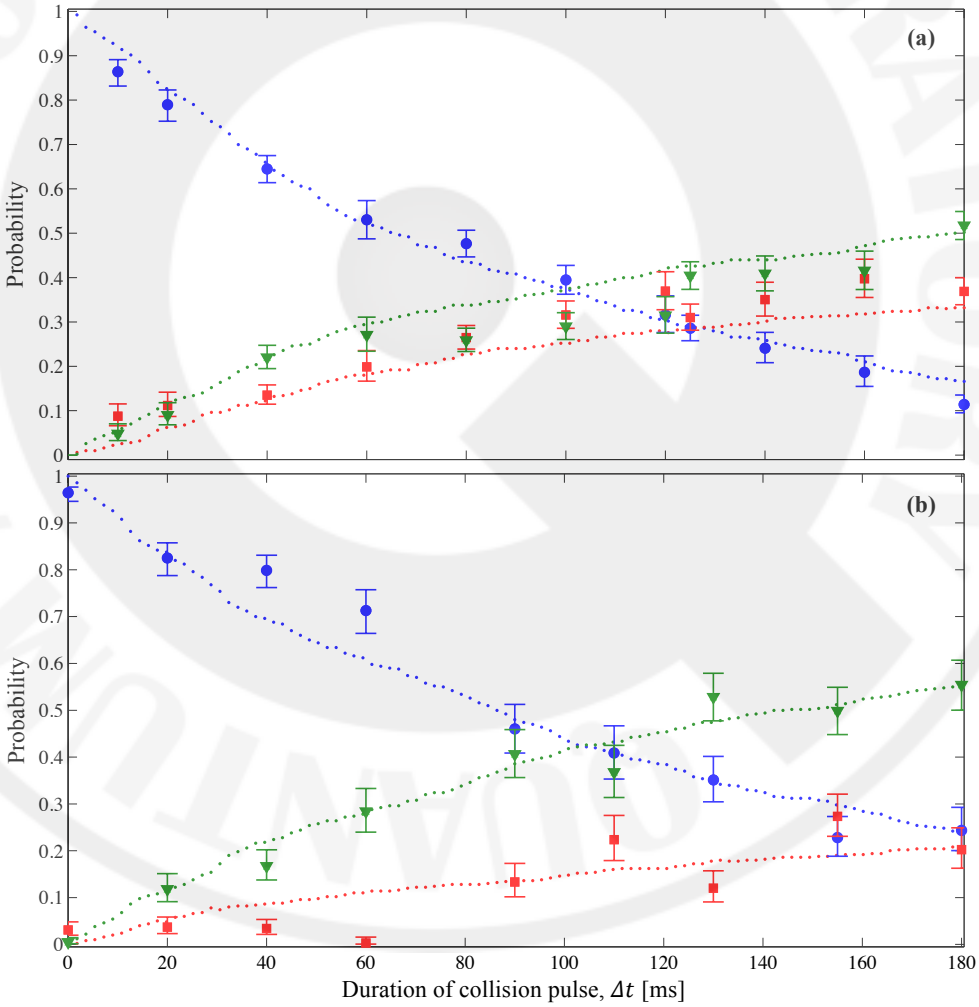

Figure 5.8 show atom pair's evolution for the cooling/repump beam power of 200 μW in (a) and 350 μW in (b). The dotted lines indicate the result of simulation.

The simulation results (dotted lines) are plotted to compare with the experimental data as shown in Figure 5.8. For the simulation results, the probabilities of the remaining two, one and zero atoms in the trap are calculated by averaging over the initial 500 pairs of simulated atoms. The Rabi frequency Ω for the LZ transition is adjusted until the averaged decay time of the pairs is the same as in the experiment for compensating the simplicity of the simulation model. For the experimental result in figure (a), the collision light pulse consisted of the collision beam with $P_{col} = 350$ nW and $\delta_{col} =$ -45 MHz and the cooling/repump beams with $P_{rep} = 200\ \mu$W and $\delta_{rep} = -4.3$ MHz. In figure (b), all beam parameters are the same values as in figure (a) except $P_{rep} = 350\ \mu$W. As seen in the figure, the simulation results agree well with the experiments.

Comparison between the pair evolutions in (a) and (b) shows that the cooling beams play a crucial role in the collision process. The result shows that $P(1|2)$ decreases when the power of the beams is increased. That is because the high power provides more efficient cooling mechanism. Consequently, the colliding pairs could have a lower E_P before collisions and required a higher E_r for the case of single-atom loss and a higher E_r has a less possibility to be released. This leads to the reduction of $P(1|2)$.

The other detuning of collision beam, $\delta_{col} =$ -75 MHz, is simulated as well. As the result shown in Figure 5.9, the simulation agrees well with the experiment. In the experiment, the collision light pulse consisted of the collision beam with $P_{col} =$ 600 nW and the cooling/repump beams with $P_{rep} = 400\ \mu$W and $\delta_{rep} = -4.3$ MHz.

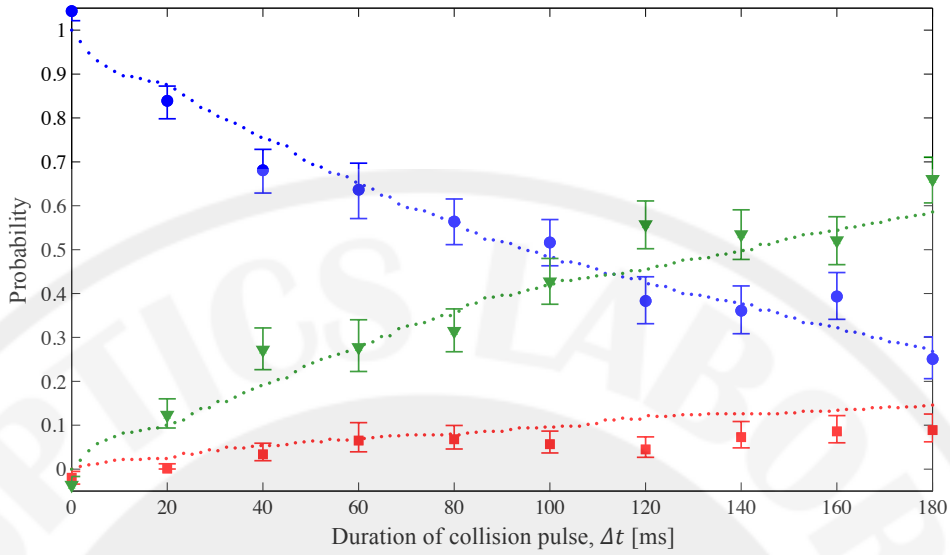

Figure 5.9. Probability to observe two, one and zero atoms in FORT under the influent of the collision light pulse plotted as function of the pulse duration where δ_{col} = -75 MHz.

Effect of the collision beam detuning

As shown in Figure 5.6 (b), the probability distribution of the released energy E_r depends on the detuning of the collision beam δ_{col}. For the case of large detuning, the colliding atoms have more chance to release the large energy compared with the small detuning. The reason is that at the corresponding Condon point R_c for the larger δ_{col}, the excited state potential has a higher gradient; the excited pair can go to the shorter range of its internuclear separation; and then it gains a larger E_r. From this reason, $P(1|2)$ would depend strongly on δ_{col}.

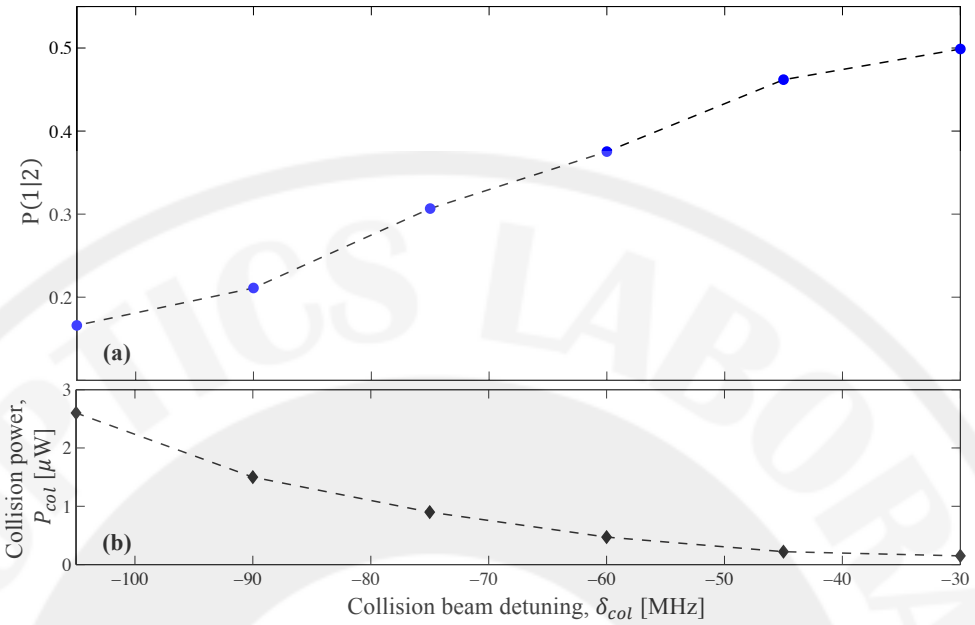

Figure 5.10. (a) P (1|2) extracted from the pairs evolution plotted as a function δ_{col}. (b) Corresponding power of the collision beam P_{col} used in the measurement.

To study an effect of the detuning on the collisions, the pair evolution was observed for several values of δ_c (from –30 to –110 MHz). All parameters of the collision pulse were fix as used in Figure 5.8 (a) except P_{col}. For each δ_c, P_{col} was adjusted such the way that the pair decay time was about 90 ms. The used P_{col} was plotted as a function of δ_c in Figure 5.10 (b). The values of $P(1|2)$ were extracted after the pair evolutions were measured. The result shows that all of the obtained $P(1|2)$ values for these near resonant light are more than zero as display in Figure 5.10 (a). Furthermore, the $P(1|2)$ value rises obviously when the detuning is closely to the resonance. The highest observed value is equal to 0.5 at the detuning of –30 MHz. From this nonzero $P(1|2)$, using the same parameters of the collision light pulse can provide the single atom loading efficiency to be exceeding the 50% limit as reported in next section.

5.1.2 Single atom loading efficiency

To prepare single atom by using the red detuned light assisted collision, the experiment began with loading about 30 atoms into the FORT. The collisions between the atoms were induced by applying of the collision light pulse for 402 ms. This duration was optimized for getting the highest single atom loading efficiency while the probability to obtain two atoms was minimized. After the collision pulse, the imaging stage then exposed the remaining atoms, of which the number was one, zero or two. These processes were repeated for 400 times to determine the single atom loading efficiency. The single atom loading efficiency as a function of the detuning of the collision beam δ_{col} was presented in Figure 5.11.

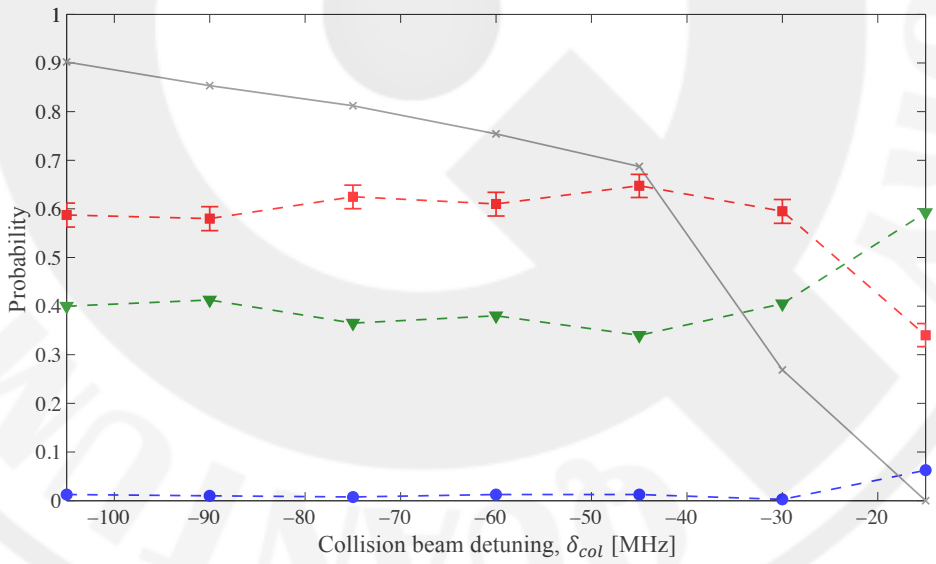

Figure 5.11. Single atom loading probability as a function of δ_{col}. Blue circles, red squares and green triangles indicate the probability of obtaining two, one and zero atoms respectively. The black crosses represent a single atom survival probability after a collision pulse of 1.5 s.

In order to understand the result, a single atom survival probability after applied the collision light pulse for 1.5 s was observed. The probability represented the trapping lifetime of single atoms while the pulse was shining them. If the probability was low, the lifetime was short. To measure the survival probability, single atoms were prepared and then shined by the collision pulse for 1.5 s. At the end, the atom numbers were measured to determine the probability.

As shown in the figure, the trend of the single atom loading efficiency agrees well with the $P(1|2)$ values in the previous figure. However the single atom loading efficiencies for the small detuning (–30 and –15 MHz) are dropped, even though the $P(1|2)$ values are high. This obstruction comes from the short trapping lifetime that is indicated by a low survival probability. As a compromise between $P(1|2)$ and the trapping lifetime, the collision light pulse with the detuning of –45 MHz gives the highest loading efficiency as seen.

The effect of the cooling/repump beam power P_{rep} was investigated as well. The single atoms were prepared by using the collision pulse with the same parameters in Figure 5.8 (a) except P_{rep} varied from 50 to 550 μW. As the result shown in Figure 5.12, the single atom loading efficiency is plotted as a function of P_{rep}. In the low power regime in the figure, the short trapping lifetime indicated by the survival probability obstructs the efficiency. The collision pulse with P_{rep} = 50 μW contributes the efficiency of only 0.39. This represents a lack of the cooling mechanism. When the power is higher, the efficiency increases. This continues until the beam power is more than 200 μW. The loading efficiency started to drop because

of the reason mentioned before in the comparison of the pair evolutions between $P_{rep} = 200$ and 350 μW in Figure 5.8.

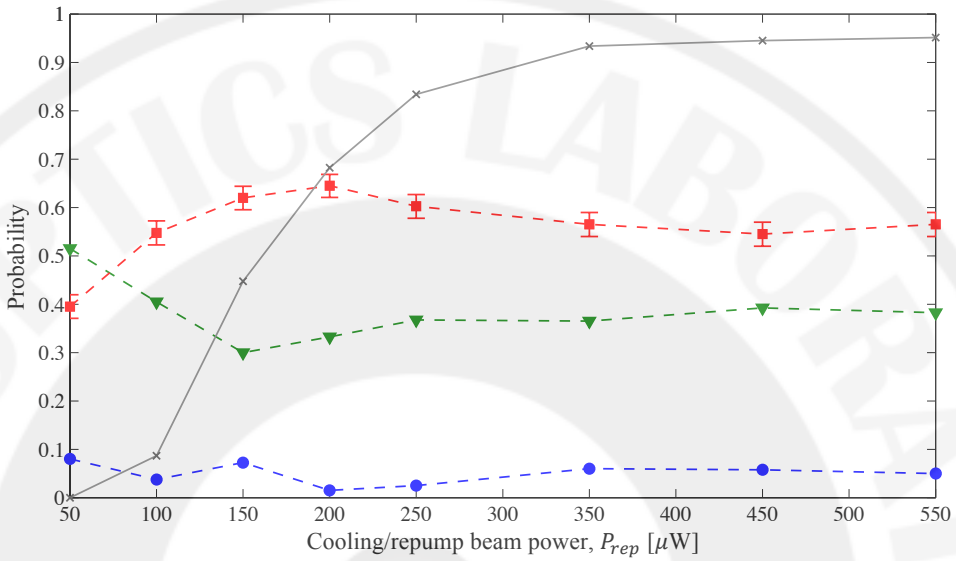

Figure 5.12. Loading probability as a function of P_{rep}. The meanings of the symbols are as in previous figure.

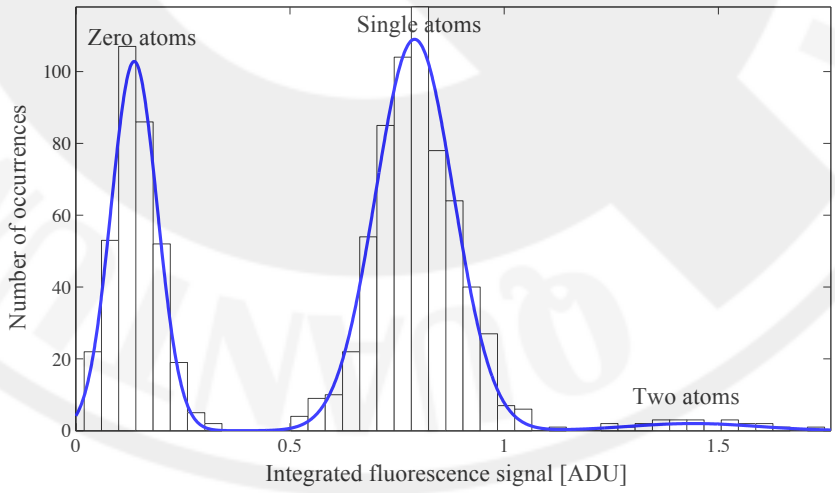

Figure 5.13. Histogram of the integrated fluorescence signal of each image for 1,000 realizations of the experiment. The large peak represents the single atom loading probability of 63.00 ± 1.53%.

A use of the collision light pulse with the parameters used in Figure 5.8 (a) provided the highest single atom loading efficiency of 63%. The efficiency was represented by the largest peak of the histogram of the integrated fluorescence signal for the 1,000 experimental realizations in Figure 5.13. The result shows that a use of the red-detuned light for preparing single atoms can provide the efficiency higher than the limit of 50% obviously.

5.2 Cold collision induced by blue detuned light

In this section, the cold collisions induced by the blue detuned light were studied. The experiment began with observing the time evolution of two atoms as detailed in Sec. 5.2.1. The simulation of two-body collision was used as a tool to obtain the insight of the collisional processes. Finally, the collision light pulse was employed for isolating single atoms in FORT. The effect of the light-pulse parameters on the single atom loading efficiency was presented in Sec. 5.2.2.

5.2.1 Time evolution of two atoms

Let consider the system of two atoms in the ground state $|S+S\rangle$ being exposed by the blue detuned light. The collision between the atoms begins with absorbing the photon at a separation of R_c. The atoms then transition into the repulsive potential of $|S+P\rangle$. When the atoms move away from each other, they decay back to $|S+S\rangle$. Consequently, the atoms gain the energy of $\hbar\delta_{col}$ as detailed before in Chapter 2.

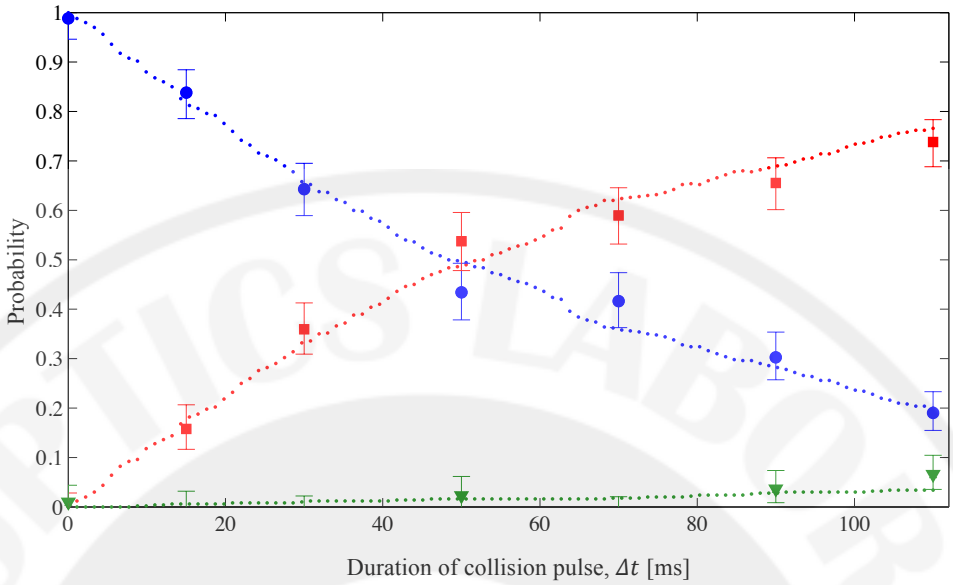

Figure 5.14. The pair evolution as a function of Δt for $\delta_{col} = 85$ MHz.

The collisional processes described above provide the capability to control the energy released from the collision by tuning the detuning of the light. If the energy is set equal to the trap depth, this would contribute a high value of $P(1|2)$. That is because the energy is enough for making only single atoms lost from the trap for the low-energy colliding pair. For this purpose, the pair evolution under the effect of blue detuned light was investigated. The collision light pulse consisted of the collision beam with $P_{col} = 11\ \mu$W and $\delta_{col} = 85$ MHz and the cooling/repump beams with $P_{rep} = 640\ \mu$W and $\delta_{rep} = -4.3$ MHz. As expected, the result in Figure 5.14 shows that the most occurrence of the collisions contributed only the single-atom loss as represented by the $P(1|2)$ value of 0.96.

The reason for obtaining the near deterministic $P(1|2)$ is discussed below. As the released energy was equal to the trap depth ($E_r = U_0$), the pair energy after collision could be written as $U_0 < E_p < 2U_0$ where the reference level is at the

bottom of the trap. If both atoms had the total energy lower than U_0, neither atom escaped from the trap. The atoms with a mount of total energy were cooled down by the light pulse and might collide with each other again. This scenario was then repeated until one of them gained the most of E_r. In this case, the atom with total energy larger than U_0 would escape from the trap while the other still was confined in the trap. From this processes, the collisions induced by this light pulse contributed only a single-atom loss except for the collision between the high-energy atoms, of which the probability to occur was very low. For getting the insight of these collisional processes, the dynamic of the colliding atoms was simulated to reproduce the observed pair evolution. The simulation result agrees well with the experiment as indicated by the dotted line in Figure 5.14. The detail of the simulation was explained below.

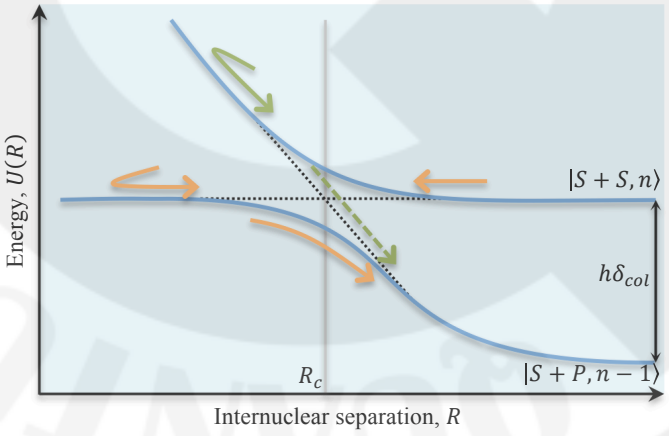

Figure 5.15. Dressed state picture showing an avoided crossing between two quasimolecular states around R_c. The color arrows show the different excitation paths.

For the case of blue detuned light, the processes in the simulation are the same as in the case of red detuned light accept for some details as following. First, an

excitation probability of the simulated atoms is different. To determine the excitation probability, the dressed state picture is considered. In Figure 5.15 the atoms, which are initially in $|S+S,n\rangle$ state may undergo an adiabatic passage followed by a LZ transition as indicated by the green arrows, or vice versa as indicated by the orange arrows. In both case, the atoms end at $|S+P,n-1\rangle$. The excitation probability can be calculated as

$$P_e = 2P_{LZ}(1-P_{LZ}). \tag{5.13}$$

Second, the energy release E_r in this collision process is fix as the constant value of $\hbar\delta_{col}$. The last, the momentum of individual atoms changes in opposite direction compared with the case of the red detuned light due to the repulsive force. So we can rewrite the equation (**5.10**) as

$$\Delta \boldsymbol{v}_1 = -\Delta \boldsymbol{v}_2 = \alpha \boldsymbol{R}\,. \tag{5.14}$$

We get a new value of α by

$$\alpha = \frac{-\boldsymbol{R}\cdot\boldsymbol{v} + \sqrt{\frac{4R^2E_r}{m} + (\boldsymbol{R}\cdot\boldsymbol{v})^2}}{2R^2}. \tag{5.15}$$

The pair evolution under the influence of the light with the detuning of 185 MHz was observed as well. In this measurement, the collision light pulse consisted of the collision beam with $P_{col} = 7\ \mu$W and the cooling/repump beams with $P_{rep} = 640\ \mu$W and $\delta_{rep} = -4.3$ MHz. The experimental and simulation results were plotted in Figure 5.16. The result gave us $P(1|2) = 0.33$, which was much lower than the previous case. The significant reduction of $P(1|2)$ for a high detuning was come

from the high released energy, which was more than twice of the trap depth. This amount of energy was high enough to make both of atoms lost from the trap.

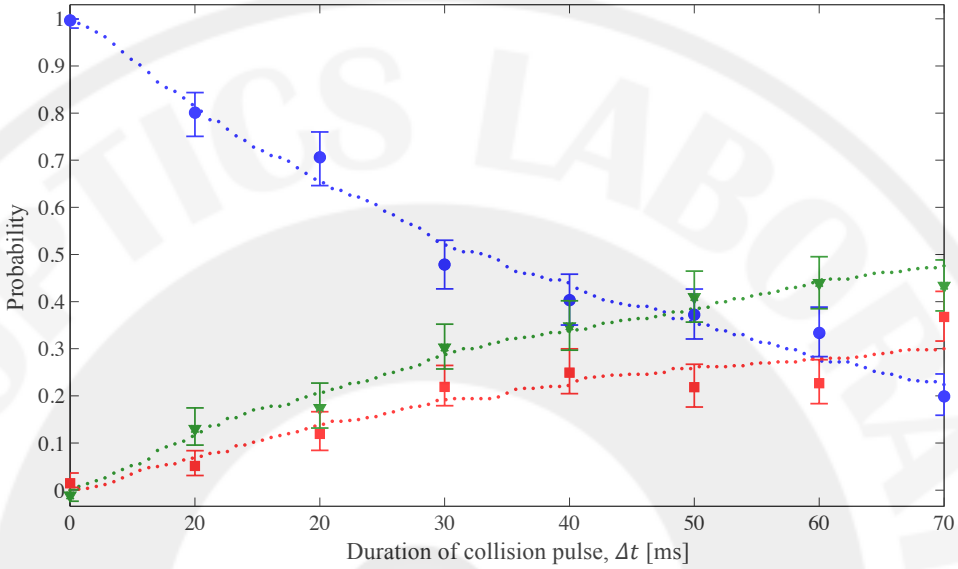

Figure 5.16. The pair evolution as a function of the duration Δt for the case of $\delta_{col} =$ 185 MHz.

5.2.2 Deterministic preparation of single atoms

The effect of the parameters of the collision light pulse on the single atoms loading efficiency is explored in this section. The parameters studied were the collision beam detuning δ_{col}, the collision beam power P_{col} and the cooling/repump power P_{rep}. Let consider first the δ_{col}, which is used for determining the released energy.

In the measurement, the cooling/repump beam parameters and the duration were fixed at the same values used in Figure 5.14. For each detuning of the collision beam, the beam power was adjusted for maximizing the loading efficiency. The single atom loading efficiency is plotted as a function of δ_{col} as represented by the red

squares in Figure 5.17. The black crosses indicate the single atom survival probability after the collision pulse of 3.5 s that is used for estimating the trapping lifetime of single atom.

The highest loading efficiency was achieved when the δ_{col} was equal to 85 MHz corresponding with the trap depth. This agrees well with the $P(1|2)$ observed before. For the other detunings, the efficiency dropped for both smaller and larger detuning. When the detuning was closed to the atomic resonance, the trapping lifetime of single atom decreased. This suppressed the loading efficiency. When the detuning was above 85 MHz, the released energy was higher than the trap depth. Even though the trapping lifetime was longer, but the excess energy leaded to the two-atom loss. This agrees well with the $P(1|2)$ observed before in the case of 185-MHz detuning.

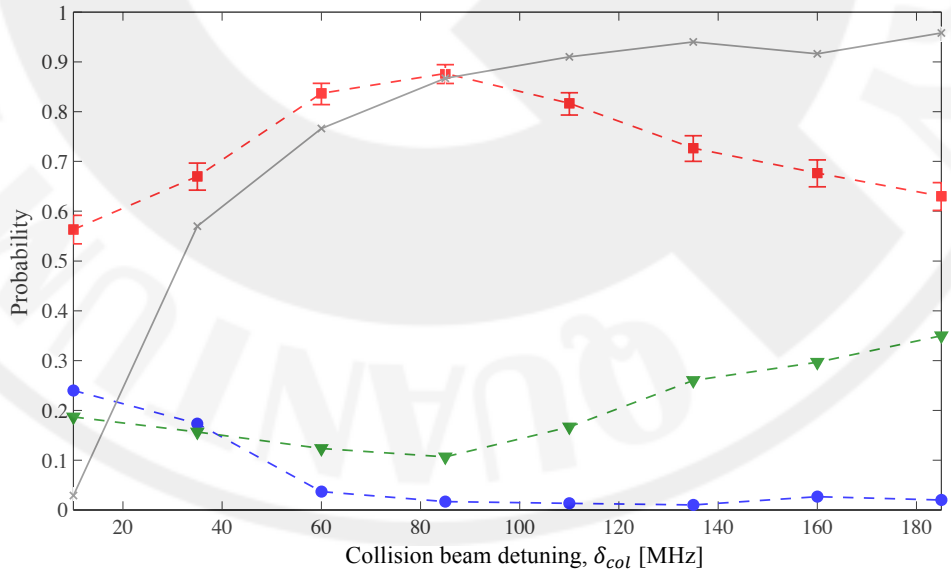

Figure 5.17. Single atom loading efficiency plotted as a function of δ_{col}.

The effect of the collision beam power on the loading efficiency was shown in Figure 5.1 (a). The single atom loading efficiency was plotted as a function of P_{col} along the probabilities of loading zero and two atoms. In the measurement, the cooling/repump-beam parameters and the collision-beam detuning were fixed at the same values used in Figure 5.14. For each value of P_{col}, the duration of the pulse was adjusted to get the maximum loading of one atom at the end of the pulse. The used duration as a function of P_{col} is shown in Figure 5.18 (b). The black crosses in the figure (a) indicate the survival probability after a collision pulse of 3.5 s.

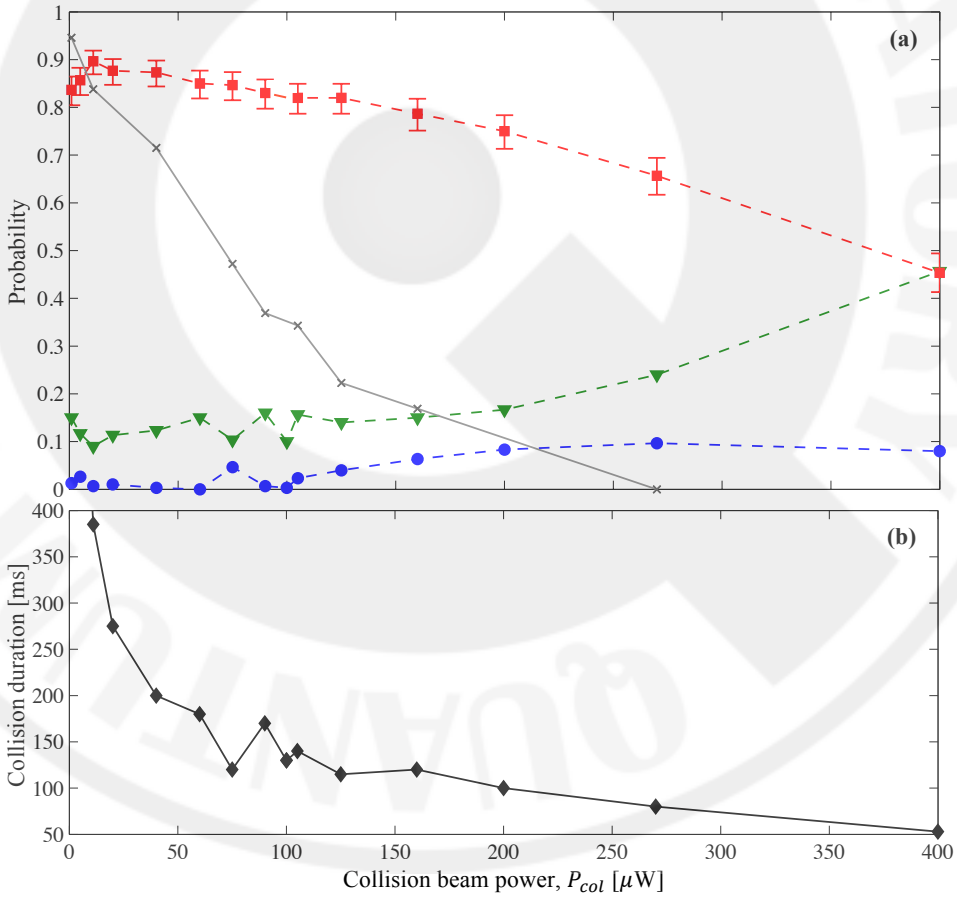

Figure 5.18. (a) Single atom loading probability as a function of P_{col}. (b) The collision duration was adjusted for each P_{col}. The duration used for $P_{col} = 1\ \mu$W which is equal to 2750 ms is not shown.

In the figure (a), the result shows that the loading efficiency is highest at the P_{col} of 11 μW and the collision duration of 385 ms (the same values as used in Figure 5.14). When P_{col} is lower than 11 μW, the trapping lifetime was longer as represented by the survival probability. However, the efficiency drops down because the used collision duration is too long. For example, in the case of P_{col} = 1 μW, the duration is 2.75 s. This duration is comparable with the measured pair-decay time of ~ 4 s due to the cooling/repump beams (in Figure 5.3). During the collision duration, the red-detuned cooling/repump beams induced the pair loss that disturbed the load of single atoms. For the case of high collision power, the efficiency was reduced as a result of the short lifetime.

Finally, the effect of cooling/repump beam power on the single atom loading efficiency was investigated. In the experiment, the collision beam parameters and the cooling/repump beam detuning were fixed at the same values used in Figure 5.14 while the cooling/repump beam power was varied from 0.3 mW to 5.1 mW. For the result, the single atom loading efficiency is plotted as a function of P_{rep} as shown in Figure 5.19. The single atom lifetime substantially depends on P_{rep}. When P_{rep} increased, the single atom survival probability for 3.5 s rises up rapidly. The longer trapping lifetime leads to the higher single atom loading efficiency as shown. However, a growth of the survival probability begins to be saturated at the power of 0.64 mW where the loading efficiency is highest. For the higher power, the loading efficiency is reduced gradually due to an increase of the pair loss induced by the intense beams.

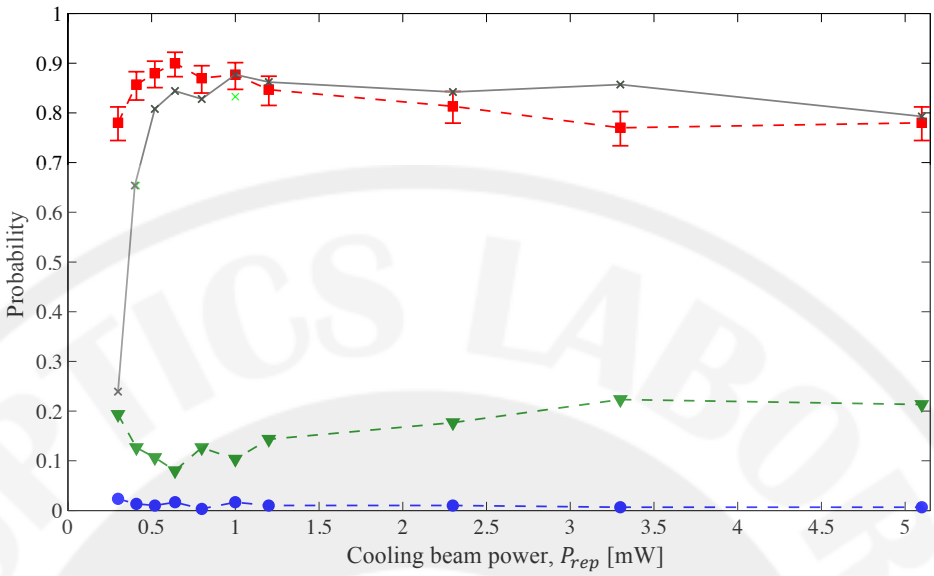

Figure 5.19. Single atom loading efficiency plotted as a function of P_{rep}.

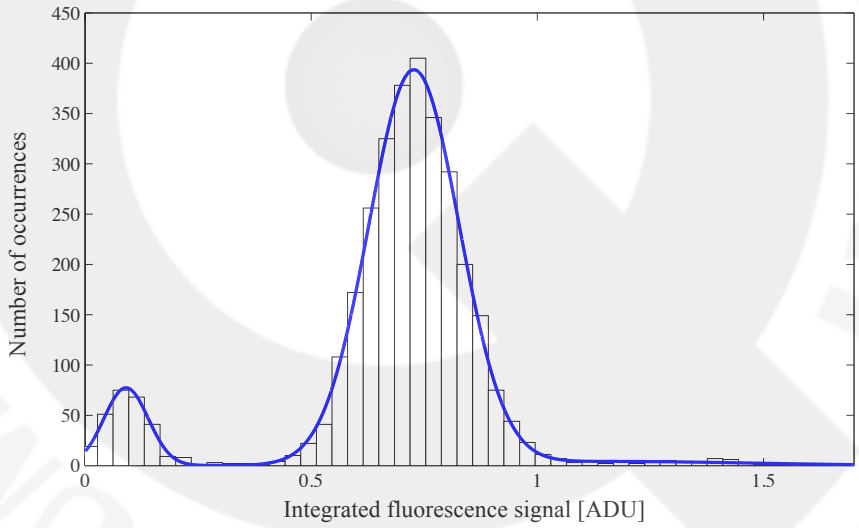

Figure 5.20. Histogram of the integrated fluorescence signal of each image for 3200 realizations of single atom preparation where the parameters of the collision light pulse were the same parameters as used in **Figure 5.14**. The large peak represents the single atom loading probability of 91.000 ± 0.006%.

As reported above, the effect of the parameters, which were δ_{col}, P_{col}, δ_{rep}, P_{rep} and the pulse duration, on the collisions was studied for enhancing the single atom loading efficiency. The highest observed efficiency is represented in Figure 5.20. The occurrence number of integrated fluorescence signals of 3200 experimental realizations is plotted as a histogram. The largest peak of the histogram indicates the single atom loading efficiency of 91%, which is significantly increased from the previous work [21].

The unsuccessful of 9% of loading single atoms would come from the reasons as following. First, the simulation of the time evolution of the pair in Figure 5.14 predicts that the unsuccessful of 3.6% would come from the pair loss events induced by the collision beam (where $P(0|2) = 0.04$). The pair loss events happened because of the collision between two atoms with high total energy. Second, during the collision duration the cooling/repump beams also induced the pair loss with the high $P(0|2)$ of 0.96 where the pair decay time was about 4 s (see Figure 5.3). From simulation, this contributed about 1.7% unsuccessful. Third, the imperfection of the vacuum system contributes about 1.5% because of the measured single atom lifetime is about 22 s. This was estimated by using Monte Carlo simulation [21]. Fourth, the imaging system had a detection efficiency of 99.5% that leaded to about 0.5% of single atom lost during the imaging process. The last, the remaining contribution could come from an inelastic collision that the collision partners were excited in to the undesigned state (the $F' = 2$ state). In this case, the atoms would gain the energy of $h \times 362$ MHz, which is the different energy between the two excited state. This amount of energy is high enough to make both of atoms escaped from the trap.

CHAPTER 6

CONCLUSIONS AND OUTLOOK

In this chapter, we begin by restating briefly the whole picture of the research in the first part of Sec. 6.1. The crucial results in the research are pointed and summarized at the end of the section. Finally, the outlook of the research are elaborated in Sec. 6.2.

6.1 Conclusions

This thesis involves investigation of light-assisted collisions between cold atoms confined optically in a FORT. The research was conducted not only for extending the knowledge of the cold collisions but also for enhancing the efficiency of single atom production, one of a precursor for a neutral-atom based quantum computer. Hence the scheme of this study is to answer the following questions: (1) What are the procedural details of the cold collisions induced by light? (2) What are the best parameters that make only one atom lost from the two-body collisions and improve the single atom loading efficiency?

To respond to these questions, the experiment began with preparing the cold ^{85}Rb atoms in a MOT inside vacuum chamber while monitoring a cold-atom cloud trapped in a MOT with the fluorescence imaging. Upon realizing cMOT followed by

optical molasses, a portion of the molasses cloud was loaded into a FORT (a dipole trap) where the cold collisions were studied.

In the FORT, the occupancy of ether one or two atoms could be prepared and identified. On average eighty-four cold atoms were loaded into the FORT initially. After applying the collision light, the majority of atoms were ejected until only a few atoms were left in the trap. The counting of the remaining atoms was permitted by the assistance of the imaging light pulse. We observed that the histogram of the atomic fluorescence counts was discrete in correspondence with the number of atoms in the trap. This allowed us to determine a small number of the atoms prepared in each experimental run. The number of atoms left in the trap depended on the duration of the collision light pulse; more atoms were lost when the duration was longer. Consequently an attempt was made to optimize the duration for loading either single or two atoms. The measured temperatures of the atoms after loading were 204 ± 5 μK for a single atom and 281 ± 14 μK for two atoms. The capability of preparation and recognition of both single and two atoms provided an ideal pathway to observe and study the individual collision events.

At this point, the questions stated before at the beginning are answerable by investigating the dynamics of two atoms in a FORT under the influence of the collision light pulse. Experimentally, the microscopic view of only two atoms in the trap allowed us to distinguish between the collisional two- and one-atom loss events. As a consequence of the loss, the reduction in the probability of retaining both atoms in the trap was observed while the probabilities of detecting one and zero atoms were increasing (see Figure 5.8). The experimental result was represented in the time

evolution of those probabilities. By simulating the dynamic of two atoms to reproduce the evolution (see Sec. 5.1.1), the insight of the collisional process is revealed and providing the answer to the first question. Furthermore, the probability of a single atom loss event in the two-body collision, $P(1|2)$, was extracted from the observed evolution. The maximization of $P(1|2)$ value was studied to answer the second question.

We found that the collisions induced by the red-detuned light for most parameters investigated gave a nonzero value of $P(1|2)$. The simulation result agrees well with the experiment and also uncovers the reason of the nonzero value. Even thought the red-detuned light assisted collisions can release a high energy (as the atoms undergo the attractive excited-state curve of the semi-molecular energy level illustrated in Figure 2.11 (b)) leading to both collision partner loss but in actuality the collisions have a potential to release a lower energy with a higher probability. For collisions between the atoms with finite speed of the center of mass, it is possible to lose only one of them for a wide range of released energy. As the probability density of the released energy has a strong dependence on the detuning of the collision light, the effect of the detuning on $P(1|2)$ was also investigated. The experimental result shows that the $P(1|2)$ value rise when the magnitude of the detuning decreases (see Figure 5.10). The highest observed $P(1|2)$ value were 0.5 at the detuning of –30 MHz. However, the employment of the light with this detuning contributed to a low efficiency for generating a single atom because of the low trapping lifetime due to the near resonance pressure. The highest single atom loading efficiency of 63% was reached by using the light with the –45 MHz detuning (the other parameters were the

same as used in Figure 5.8 (a)), which were the best parameters compromising between $P(1|2)$ and the trapping lifetime. To the best of our knowledge, this is the first time that the single atom loading efficiency of the red-detuned light-assisted collision exceeds the limit of 50% [9, 18-20]

In the case of collisions induced by the blue-detuned light, we found that the capability to control the released energy from the collision leaded to the observation of near deterministic $P(1|2)$ value. Experimentally, when the detuning of the collision light was set to the value corresponding to the trap depth of FORT, most of the two-atom collisions contributed only to single atom lost. As a result, we observed the highest value of $P(1|2)$ to be 0.96. The simulation was used to reveal the hidden process of this collision as mentioned in the following details. Since two atoms undergo into the repulsive quasi-molecular potential by absorbing the light, the energy released is limit at the trap depth energy. By sharing this amount of energy to both of them, it is not allowed for two-atom loss except for the collision between the high-energy atoms. After the collision, the atoms left in the trap may have a high total energy that leads to the pair loss and the short trapping lifetime. Therefore the cooling mechanism of PGC formed by the cooling/repump beams played a crucial roll for dissipating the excess energy. The cooperation between the collision light and the cooling light leads to a high $P(1|2)$ value. Consequently this provided the world high record of 91% efficiency of loading single atom.

6.2 Outlook

It would be interesting to use the others atomic species such as ^{87}Rb and Cs. Their larger hyperfine splitting would lead to the use of a deeper trap corresponding with the repump and cooling mechanism of the cooling beam. Consequently the collision beam will be set to the larger blue detuned frequency that would reduce the heating due to the radiative pressure of the beam. Furthermore the separation between the atomic ground states is bigger, that would reduce the two-atom loss from the inelastic collision induced by the cooling/repump beams. The two-atom loss from the hyperfine-changing collision may be reduced as a result of larger hyperfine splitting of the excited states. From all above reasons, the use of atomic species with larger hyperfine splitting would provide the big improvement in the efficiency of the single atom preparation by the blue-detuned light.

The other geometry of trap is interesting to be use as well. As in the case of the single atom preparation by employing the red-detuned light, the efficiency would be improved if the high collision rate of the high-energy atoms could be allowed. This may increase $P(1|2)$ with out compromising the PGC cooling rate (the intensity of the cooling/repump beams). As a consequence the left atom after the collision would have a longer trapping lifetime. It has a potential that the efficiency of loading single atom would be improve by using the tight trap under conditions.

However, with the findings in this thesis they could be applied to other applications. The capability to prepare single atoms with efficiency of 91% in the duration of 542 ms could prepare individual qubits occupied in 30-site lattice with the

probability of 0.06. By using the detection light pulse to choose only the successful loading, the single atoms perfectly occupied in all sites of would be achieved in 10 s (and about one minute for the 50 sites). This could provide an infrastructure for quantum computing and information research. In addition, the foundation of nonzero $P(1|2)$ in the collisions induced by the red-detuned light could effect the interpretation of the correlated research such as cold collision study [52, 53] and parity measurements [54].